Understanding the differences in energy levels between $CH_3NH_3PbI_3$ and $(CH_3NH_3)_3Bi_2I_9$ in darkness and under illumination using Kelvin probe measurements

Zubin Farroakh Parekh

Submitted to Swansea University in fulfilment of the requirements for the Degree of Master of Science

Prifysgol Abertawe
Swansea University

Swansea University

2019

KPTechnology

M2A
MATERIALS AND MANUFACTURING ACADEMY

UNDEB EWROPEAIDD
EUROPEAN UNION

Llywodraeth Cymru
Welsh Government

Cronfa Gymdeithasol Ewrop
European Social Fund

Abstract

Deployment of solar energy capacity to rural areas in developing countries requires a cheap and light-weight solar technology. If the solution to this is perovskite solar cells, the use of a lead-free perovskite will avoid toxicity hurdles. In this thesis, two perovskite absorber materials are investigated for their differences in photovoltaic characteristics. Lead-free methylammonium bismuth iodide is analysed alongside methylammonium lead iodide using a range of Kelvin probe techniques. Both perovskite materials are characterised as thin-film photoactive layers deposited on top of fluorine-doped tin oxide glass substrates. Energy level measurement reveals that changing only the metal cation (switching lead with bismuth) completely tunes photo-induced behaviour of the perovskite. Spectroscopic data for surface photovoltage shows the fermi level of $(CH_3NH_3)_3Bi_2I_9$ shifts above and below its dark position at different wavelengths of illumination. Under white light pulses, $CH_3NH_3PbI_3$ performs better with a repeatable surface photovoltage of 250mV. In unique conditions of 500nm light at low intensity, $(CH_3NH_3)_3Bi_2I_9$ generates the higher surface photovoltage with 120mV. These surface photovoltages represent the open-circuit voltage contribution from the absorber material. Both perovskites demonstrate that surface photovoltage remains unchanged after over 5 months of storage in a dark ambient environment. Although this is a very positive result, it is speculated that a poorer retention of surface photovoltage would arise if samples were exposed to light during storage. The measured bandgap of $(CH_3NH_3)_3Bi_2I_9$ was 1.70eV, and the measured bandgap of $CH_3NH_3PbI_3$ was 1.598eV. In general, the work provides useful comparative data between two perovskites and shows $(CH_3NH_3)_3Bi_2I_9$ could have future applications as a photovoltaic device in monochromatic light conditions or with tandem cells.

Conferences and Visits

	Location	Purpose	Dates
Conferences			
SPECIFIC Gregynog	Tregynon, Wales	Oral presentation	17-18/12/18
M2A Annual Conference	Swansea, Wales	Oral and poster presentation	30/04/19
HOPV 19	Rome, Italy	Poster presentation	13-15/05/19
Sêr Solar Symposium	Swansea, Wales	Poster presentation	20/03/19
Visits			
Imperial College	London, England	Training	07/09/18
KP Technology	Wick, Scotland	Use of facilities	12-14/03/19
KP Technology	Wick, Scotland	Use of facilities	03-04/09/19

HOPV 19 Conference

In May I had the privilege of attending a conference on Hybrid and Organic Photovoltaics (HOPV) in Rome with a poster presentation. Although perovskite solar cells were not in the conference title, the topic dominated the conference. I attended the conference with a poster submission. I approached experts and asked their thoughts on complex data I had gathered. I learnt of some interesting avenues for further research like the mechanical stresses that apply to flexible perovskites. I was the only member from my research group who attended. This gave me a wonderful chance to gain experience and confidence networking alone.

Visits to KP Technology

I made two visits to my industrial sponsor KP Technology, where I was welcomed to use their advanced facilities for additional measurements. The first visit was made in March 2019 to carry out a full set of energy level measurements on the materials under investigation. A second trip in September 2019 fulfilled a purpose of running a second phase of testing after analysing results. These visits were instrumental in measuring and understanding the band diagrams.

Declaration and Statements

The following people and institutions contributed to the publication of work undertaken as part of this thesis:

Candidate	Zubin Parekh, Swansea University
Author 1	Sagar Jain, Swansea University
Author 2	Iain Baikie, KP Technology
Author 3	Matt Davies, Swansea University

DECLARATION

This work has not previously been accepted in substance for any degree and is not being concurrently submitted in candidature for any degree.

Signed ..... ████████████████████ .... (candidate)

Date ....27/08/2020...

STATEMENT 1

This thesis is the result of my own investigations, except where otherwise stated.

Other sources are acknowledged by footnotes giving explicit references. A bibliography is appended.

Signed .... (candidate)

Date ....27/08/2020..

STATEMENT 2

I hereby give consent for my thesis, if accepted, to be available for photocopying and for inter-library loan, and for the title and summary to be made available to outside organisations.

Signed .... (candidate)

Date ....27/08/2020...................................

Contents

Acknowledgements

Acronyms and Abbreviations

%wt	Percentage weight
APS	Ambient pressure photoemission spectroscopy
AU	Arbitrary units
BIPV	Building integrated photovoltaics
CBM	Conduction band minima
CNT	Carbon nanotubes
CPD	Contact potential difference
DMac:NMP	Dimethylacetamide: 1-methyl-2-pyrronlidinone
DMF	Dimethylformamide
DMSO	Dimethyl sulfoxide
ETL	Electron transport layer
FF	Fill factor
FTO	Fluorine-doped tin oxide
GBL	Gamma-butyrolactone
HOMO	Highest occupied molecular orbital
HOPV	Hybrid and organic photovoltaics
HTL	Hole transport layer
IPA	Isopropanol
ITO	Indium-doped tin oxide
J_{sc}	Short circuit current
KP	Kelvin probe
LUMO	Lowest Unoccupied molecular orbital
M	Mols/dm^3
M2A	Materials and Manufacturing Academy
MABI	Methylammonium bismuth iodide
MAI	Methylammonium iodide
MAPI	Methylammonium lead iodide
NREL	National Renewable Energy Laboratory
ONHR	Off-null height regulation
PCE	Power conversion efficiency
PV	Photovoltaics
QR	Quantum rods
QTH	Quartz tungsten halogen
R^2	Coefficient of regression
RPM	Revolutions per minute
SKP	Scanning kelvin probe
SPECIFIC	Sustainable Product Engineering Centre for Innovation in Functional Coatings
SPS	Surface photovoltage spectroscopy
SPV	Surface photovoltage
UHV	Ultra-high vacuum
UPS	Ultraviolet photoemission spectroscopy
UV	Ultraviolet
v/v	Volumetric proportion
VBM	Valence band maxima
V_{oc}	Open circuit voltage
WF	Work function
WWF	World Wide Fund for Nature
XRD	X-ray diffraction

Chapter 1. Introduction

1.1 Research route

The climate change problem

Development of renewable energy is at a momentous point in time. Awareness and acceptance of climate change has risen over the last decade, but unfortunately so have average global temperatures. During the 20th century the earth's average temperature had risen by 2 degrees Fahrenheit, but even more worrying is that scientists of the International Panel on Climate Change (IPCC) estimate a temperature rise between 2.5 to 10 degrees Fahrenheit over the next century [1]. A rise by 1.5°C is reported to be the threshold for climate change [2]. Greenhouse gas emissions are the primary cause of climate change because they absorb and radiate 90% of radiation reflected off the earth [3]. The UK has set important targets to minimise greenhouse gas emissions as the consequences globally are devastating.

- In 2008 the UK set the target of reducing its greenhouse gas emissions by 80% relative to 1990 by 2050 [4].
- In 2019 this was amended to achieving net zero greenhouse gases by 2050 [2].

Renewable energy offers emission free energy generation. Demand will continue to grow as the world attempts to minimise climate change. The WWF submitted a report back in 2011 demonstrating that the world could feasibly produce energy 100% from renewable sources by 2050 [5].

Despite the increasing efforts to fight climate change, global carbon dioxide emissions increased by 1.7% in 2018 [6]. Globally in the last four years, more renewable energy capacity has been installed than fossil fuel and nuclear combined. In 2018, 181GW of new renewables were installed [6]. 55% of the renewable energy capacity installed in 2018 was solar energy. Solar energy has been the dominant source of global renewable capacity installed each year since 2016 (Figure 1).
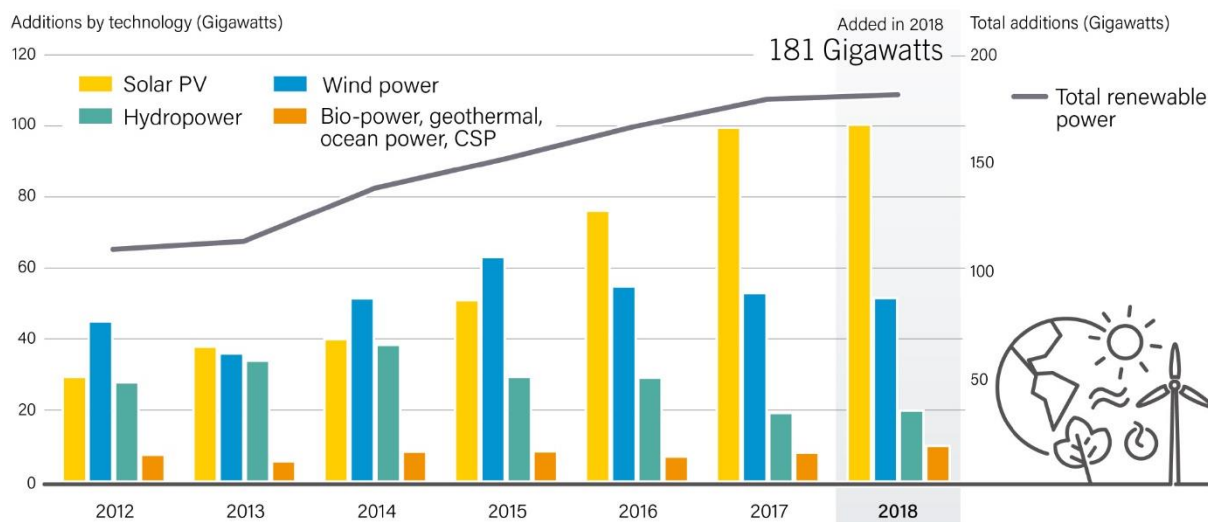
Figure 1 - Annual additions of renewable power capacity, by technology and total, 2012-2018. Figure copied with permission from REN21 2019 Global Status Report [6].

Although solar energy is storming in terms of capacity installed, annual electrical power generation highlights how little it contributes to global energy production. In 2018, 2.4% of the world electricity generation came from solar energy (Figure 2) [6]. However electrical power makes up only 17% of energy consumption (Figure 3).
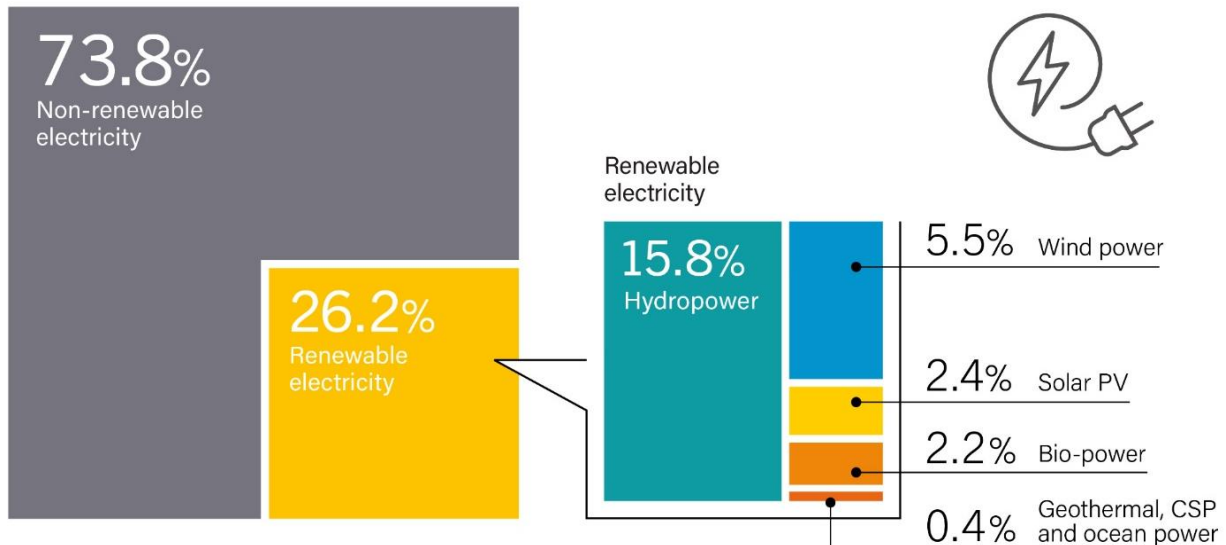
Figure 2 - Estimated renewable energy share of global electricity production, End-2018. Figure copied with permission from REN21 2019 Global Status Report [6].

With heating and cooling at 51%, a rise in solar powered home heating could make all the difference. Although silicon solar panels on rooftops are becoming more and more popular, other building integrated photovoltaics (BIPV) are being explored. Swansea University have demonstrated solar air heating walls, photovoltaic windows and thin-film solar PV integrated in steel roofing with the 'Active Buildings' project run by SPECIFIC [7].
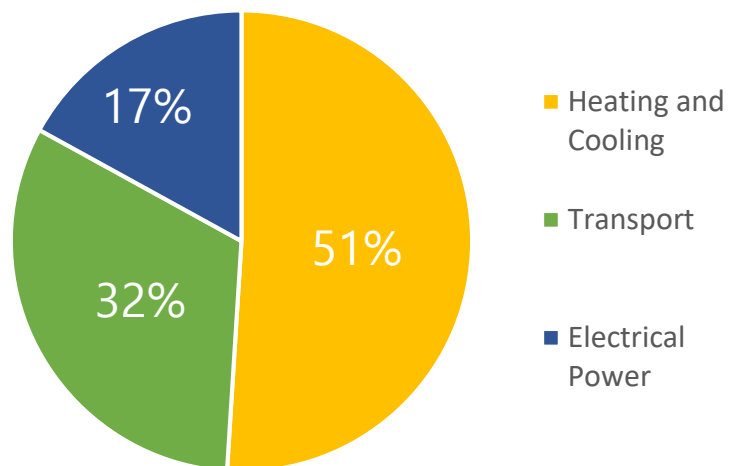
Figure 3 - Total final energy consumption by sector, 2016. Data copied from with permission from REN21 2019 Global Status Report [6].

Solar energy is still far from meeting its full potential. The power of the sun absorbed by the earth's surface for one hour would be enough to provide energy to the entire earth for one year [8]. It is anticipated that by 2020 the cost of onshore wind and solar PV will both become cheaper than the cheapest new coal, oil or gas alternatives [9].

There is a variety of solar cell technologies that can be split into first, second and third generation depending on the materials used.

First generation solar cells are made from highly pure silicon in polycrystalline or monocrystalline form. This is the conventional solar cell technology that is seen in most solar panels today. Monocrystalline cells have higher efficiencies but the polycrystalline cells are cheaper to manufacture so they are both popular [10]. The efficiency also depends on the purity of the silicon but generally is around 25% for monocrystalline cells and 20% for polycrystalline cells [11].

Second generation solar cells are thin-film technologies using a range of different materials. These include amorphous silicon, cadmium telluride and copper indium gallium selenide. Although these may have poorer efficiencies, they are lower in cost and they opened doors to new photovoltaics applications with their light weight and flexibility. The manufacturing process is faster and thin layers mean less material is required [12]. This makes second generation technology well-suited to solar power plants.

Third generation solar cells are a group of emerging technologies that are currently being heavily researched to produce solar cells with higher efficiency and lower cost per watt of electricity [13]. These include tandem cells, dye sensitised solar cells, organic PV, perovskite solar cells and quantum dots. Third generation technologies are mainly manufactured with solution-processed methods which offer fast and low-cost manufacture.

It can be interesting to learn just how rapidly the technology has progressed by taking a brief look at solar cell history and when perovskite solar cells were introduced.

1887: The photoelectric effect was discovered by Heinrich Rudolf Hertz [14].

1932: Audobert and Stora discover the photovoltaic effect [15]**.**

1954: Photovoltaic cell is developed by Daryl Chapin, Calvin Fuller and Gerald Pearson [15].

1957: Hoffman Electronics achieves **9%** efficient photovoltaic cells [15].

1958: Space satellites are successfully powered by silicon solar cells [15].

1985: The University of New South Wales breaks **20%** efficiency under 1-sun conditions [16].

1990: Solar-powered plane flew over the United States in stages using no fuel at all [17].

1994: The Nation Renewable Energy Lab (NREL) developed a solar cell with **30%** efficiency [18].

2006: Several major high street electric retailers stock PV modules in UK [18]**.**

2009: First perovskite solar cell was made with **3.8%** efficiency [19].

2012: Perovskite solar cell efficiency reaches **9%** [20].

2015: The largest photovoltaic power plant in the world had a capacity of 850 MW [21].

2016: Portugal runs on renewable energy alone for 107 hours [22].

2019: Maximum efficiency for a perovskite solar cell is **25.2%** [23].

Solar energy has become a huge contributor to renewable energy capacity as shown on Figure 1. This is largely down to manufacturing plants in China successfully optimising the production of silicon photovoltaics; leading the way for other countries [24]. Cheap mass production has led to prices dropping for silicon-based solar panels.

Figure 4 is the NREL Best Research-Cell Efficiencies graph. It shows improvements in all solar cell technologies with verified PCE (Power Conversion Efficiency). Silicon solar cell technology has improved by less than 2% since year 2000. Although 95% of all solar technology is silicon based [25], there is definitely room for third-generation technology.
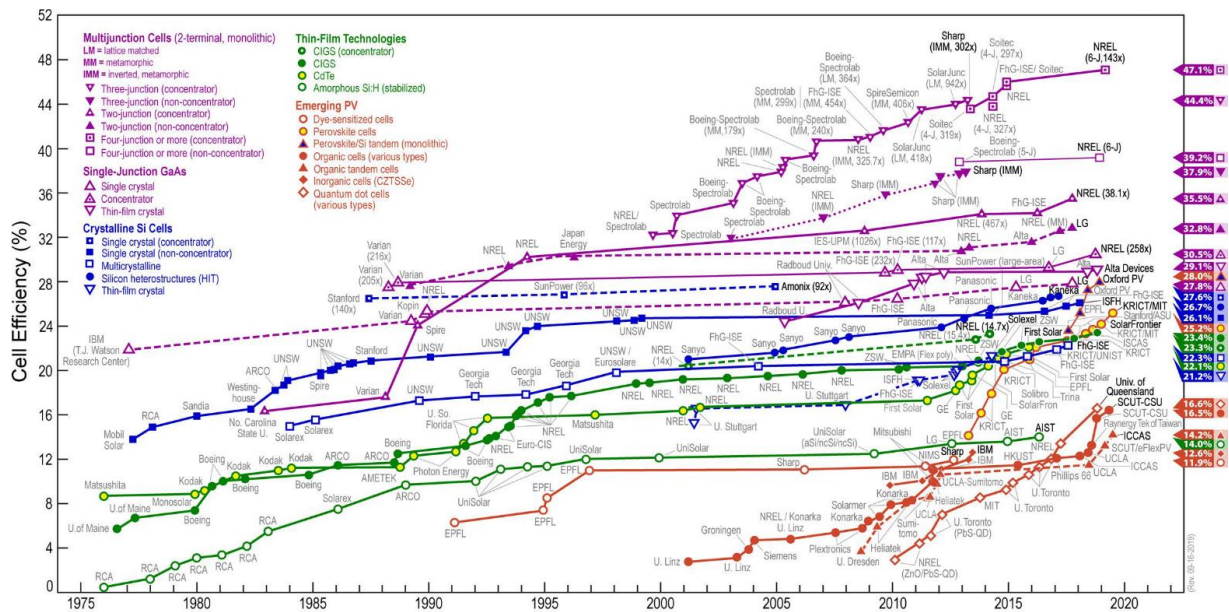
Figure 4 - NREL Best Research-Cell Efficiencies from 16th September 2019 [23].

The most recent generation of solar cells is third-generation. This generation offers printable low-cost options to manufacturing solar cells. The most advancing third-generation technologies are:

- Tandem solar cells
- **Perovskite solar cells**
- Dye sensitised solar cells
- Organic solar cells
- Quantum dot solar cells

Perovskite solar cells are one of the most researched third generation solar cell technologies because of rapidly improving PCE results, and manufacturing methods that are quick and cheap. They also can be engineered to flexible and transparent design criteria. Recently, tandem solar cells are showing most promise, as efficiencies around 40% are achieved by using four or more junctions in a sandwich structure [23] - these can be perovskite layers as well.

Developing countries close to the equator have the most ideal locations to focus solar energy. In India, rural villages have only recently been attached to the national grid [26]. For some remote and inaccessible locations solar panels with energy storage are installed to avoids huge energy loss through mains grid cables over large distances [27]. Perovskite solar cells can be exceptionally

lightweight and thin; an economic alternative to deploying heavier and bulkier solar packs across rural areas.

Perovskite solar cells

Perovskite solar cells (PSCs) are made with an intrinsic semiconductor absorber material that has perovskite crystal structure. The perovskite crystal structure is ABX_3 in terms of stoichiometry and it is named after $CaTiO_3$ – a mineral discovered by L.A. Perovski. The cubic unit cell for this structure is detailed in Figure 5 and Table 1. [28]
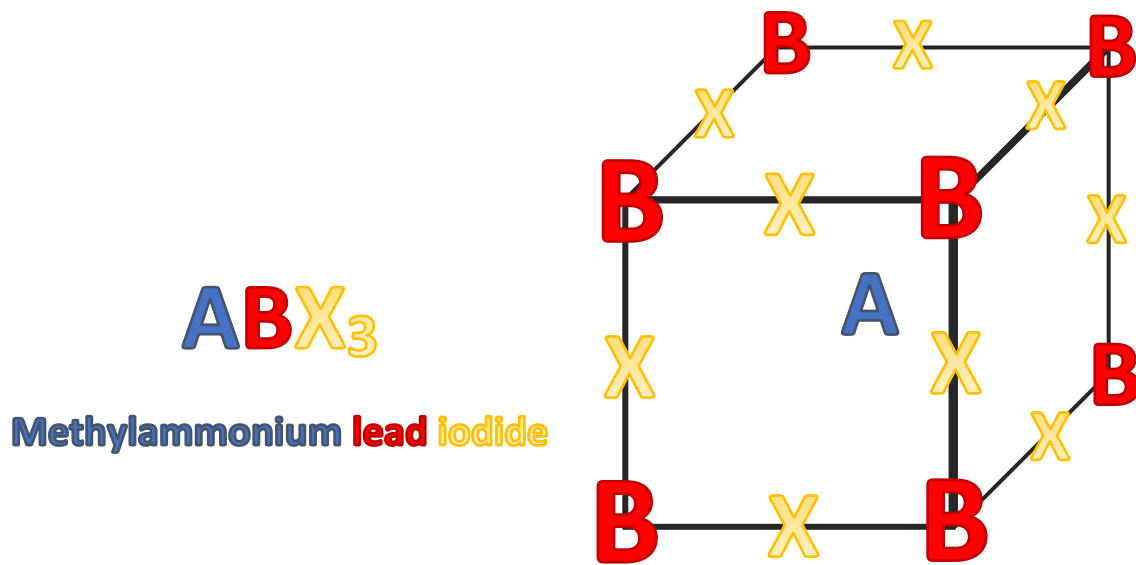
Figure 5 - Perovskite Unit Cell with ABX_3 composition.

Table 1 – Ion coordinates within ABX_3 perovskite crystal.

Constituent	Type of ion	Unit Cell Coordinates
A	Cation	½, ½, ½
B	Cation	0, 0, 0
X	Anion	½, 0, 0

The first attempt to use perovskites as photovoltaic devices was documented in 2009 and an efficiency of 3.8% was recorded [19]. The low-cost manufacturability of the samples meant that research was cheap and fast. Low-cost research meant that many research groups could get involved with PSC research. As the wonderful optoelectronic properties of perovskites were discovered, the PCE rose from 3.8% to 22.7% in just 7 years - the fastest improving solar cell technology ever [29]. The halide perovskite was the catalyst of success in terms of increasing PCE. The ability of perovskites to achieve high efficiencies comes down to a number of strong optoelectronic properties they commonly have. These are: high absorption coefficient, tuneable bandgap, long carrier recombination time, long carrier diffusion lengths and high electron/hole mobility [29]. A high absorption coefficient means a

high number of bandgap photons are absorbed when a perovskite is under illumination. The composition of the perovskite can be altered to give the material a different bandgap. This is how band gap tuning is achieved, and it works particularly well for halide perovskites [30]. Long carrier recombination time is important for solar devices because it means charge carriers are effectively contributing to an electric field for a longer period of time before recombining. The carrier diffusion length is the distance a carrier travels before recombining [31]. Long carrier diffusion lengths in perovskites lead to high electron and hole mobility [32]. Both these characteristics mean that electrons and holes generally have good ability to move within the perovskite bulk material resulting in a higher current.

As a commercial product, PSCs offer other advantages: low-density films, physically flexible films and cost-effective production routes [29]. 'Lightweight' means they are easier to install on rooftops, and 'flexibility' means they can be attached to curved surfaces. Deploying perovskite solar cells to rural areas in developing countries becomes easier because they can be thin and lightweight, with high power-to-weight ratio [33][34]. In comparison to silicon solar cells, the manufacturing cost per Watt is around 15-25% of the cost for traditional silicon-based panels [35]. Perovskite solar cells can also be engineered to be colourful, opaque and transparent – opening the possibility of energy harvesting windows and features.

On the NREL best efficiencies graph (Figure 4), the highest recorded PCE for perovskites is 25.2% [23]. In general, the highest efficiencies of perovskite solar cells have been from lead halide materials. The lead content in these materials means that the resulting commercial product would be a source of toxicity. This has promoted huge interest into lead-free perovskites.
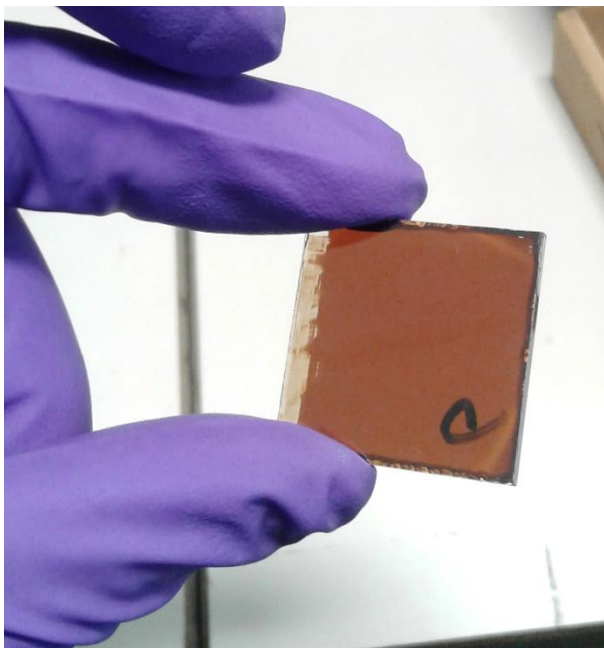
a   b

*Figure 6 - Photos of perovskite thin films manufactured at Swansea University. **a** Methylammonium lead iodide on FTO-glass substrate. **b** Flexible and transparent perovskite solar cell module produced by Sauletech [123].*

*Image **b** from www.sauletech.com*

1.2 Lead-free perovskite solar cells

The lead issue

The most common perovskite material tested for solar cells is methylammonium lead iodide (MAPI). The iodide ion is often interchanged with bromine and chlorine to tune the bandgap as desired. Lead is poisonous to the human organs and can cause damage to the nervous and reproductive systems, as well as the hematopoietic and renal organs, resulting in a range of disabilities and even death [29]. The lead content could easily spread into the environment if it is allowed to dissolve into rain water. Non-hermetic sealing, incorrect afterlife disposal or damaged units are all plausible scenarios that could result in the release of lead into the environment. This toxicity obstacle has led to a demand for research into lead-free perovskites for solar cells.

The lead ion (Pb^{2+}) is divalent, therefore an obvious replacement would have a +2 oxidation state [29]. Elements with 2+ or 4+ valency are suitable for replacing Pb in $CH_3NH_3PbI_3$ [36]. Group 14 and 10 metals are most common alternatives [37]. Of the Group 14 elements tin and germanium are the best candidates because they both have strong and broad optical absorption [36]. Atoms of smaller radius are less suited as they will lead to greater distortion and unstable structures, making bismuth a good candidate [36].

The maximum lead-free efficiencies achieved to date are displayed in Table 2. It is common that the highest efficiencies come from absorbers that are not of exact ABX_3 composition. In some absorbers proposed, the ABX_3 is hard to recognise. In fact, the term 'perovskite' is loosely used for a family of absorbers that includes: perovskite-like, double-perovskite, triple-cation perovskite and hybrid perovskite – each of which do not have ABX_3 composition. For bismuth and antimony perovskites the divalent Pb^{2+} is replaced with trivalent Bi^{3+} and Sb^{3+}, therefore the ABX_3 structure becomes a perovskite-like structure e.g $A_3B_2X_9$ [38]. Although not strictly perovskite, they are referred to as perovskite throughout this work. Figure 7 shows the association between perovskite group and lead content of the absorber.
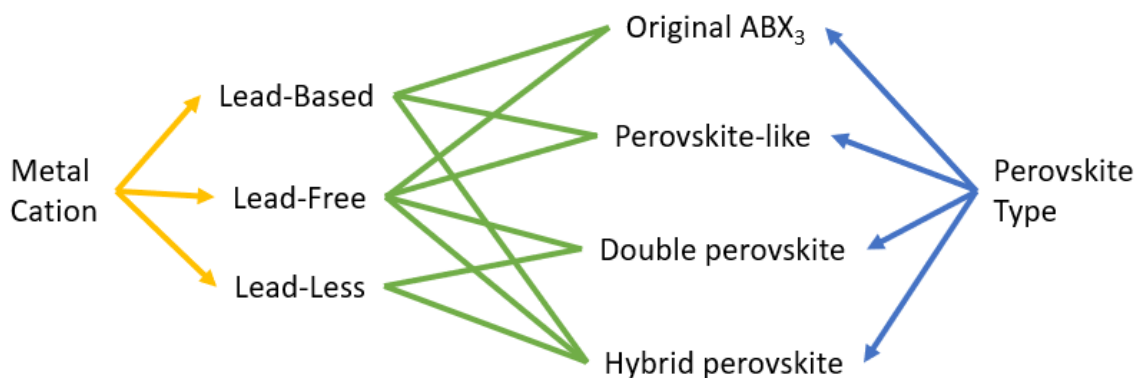
Figure 7. Links and overlapping groups of perovskites depending on the metal cation.

Despite all this interest in lead-free perovskite solar cells, methylammonium lead iodide is likely to become a successful commercial product. The efficiencies achieved are much higher, and the lead issue can be contained. But will it be cost-effective? Exploration into lead-free is a possibility of a safer and more sustainable alternative.

In terms of efficiency, tin-based halides are the most promising. A maximum PCE of 12.96% was achieved by Chienyi Chen in 2016 using Caesium as the monovalent ion (Figure 8, Table 3) [39]. This was an example of lead-free perovskite in the form of quantum rods.

Table 2 - Highest efficiencies for tin-based, antimony-based and bismuth-based lead-free perovskites found in literature.

Absorber	Architecture	PCE %	Date	Ref
$CsSnI_3$	$ITO/TiO_2/CsCnI_3/Spiro\text{-}OMeTAD/Au$	12.96	21/11/16	[39]
$(N\text{-}EtPy)SbBr_6$	$ITO/TiO_2/(N\text{-}EtPy)SbBr_6/P3HT/Au$	3.80	04/10/17	[40]
$(CH_3NH_3)_3Bi_2I_9$	$FTO/c\text{-}TiO_2/mp\text{-}TiO_2/MA_3Bi_2I_9/P3HT/Au$	3.17	01/05/18	[41]
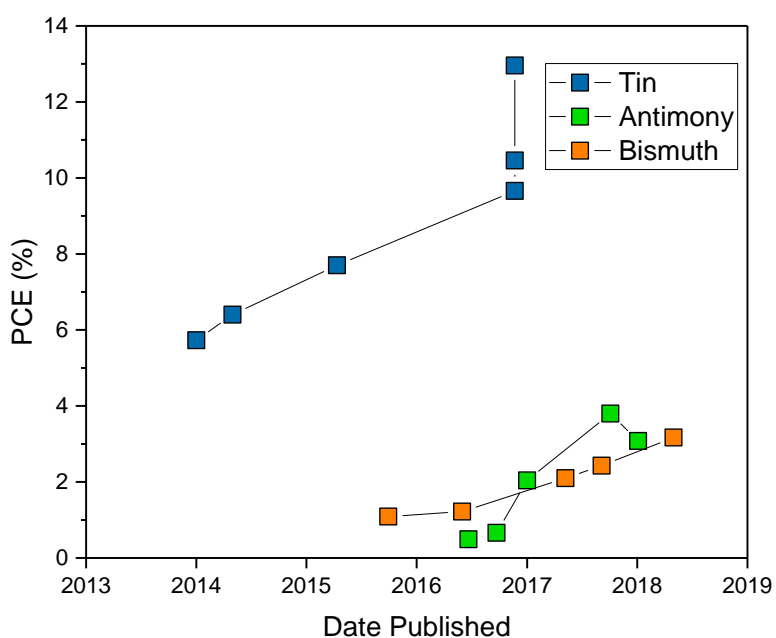
Figure 8 - Timeline of increasing highest efficiencies for lead-free perovskites (including some which are perovskite-like, and double-perovskite), August 2019.

Table 3 - Best PCEs for Tin, Antimony and Bismuth lead-free absorbers.

Absorber	Type	PCE (%)	Date Published	Reference
$MASnIBr_2$	Perovskite	5.73	01/01/2014	[30]
$MASnI_3$	Perovskite	6.4	01/05/2014	[42]
$MASnI_3$	Perovskite	7.7	12/04/2015	[43]
$CsSnCl_3$	Perovskite	9.66	21/11/2016	[39]
$CsSnBr_3$	Perovskite	10.46	21/11/2016	[39]
$CsSnI_3$	Perovskite	12.96	21/11/2016	[39]
$MA_3Sb_2I_9$	Perovskite-like	0.49	21/06/2016	[44]
$Rb_3Sb_2I_9$	Perovskite-like	0.66	22/09/2016	[45]
$MA_3Sb_2I_9$	Perovskite-like	2.04	01/01/2017	[46]
$(N\text{-}EtPy)SbBr_6$	Perovskite-like	3.8	04/10/2017	[40]
$MASbSI_2$	Perovskite	3.08	04/01/2018	[47]
$Cs_3Bi_2I_9$	Perovskite-like	1.09	29/09/2015	[48]
$Cs_2AgBiBr_6$	Double-perovskite	1.22	31/05/2016	[49]
$AgBi_2I_2$	Perovskite-like	2.1	08/05/2017	[50]
Ag_2BiI_5	Perovskite-like	2.43	05/09/2017	[51]
$MA_3Bi_2I_9$	Perovskite-like	3.17	01/05/2018	[41]

Table 4 – Estimated characteristics to assess economic value of different perovskites.

Perovskite	Efficiency	Toxicity	Stability	Cost
Lead-based				
Tin-based				
Antimony-based				
Bismuth-based				
Germanium-based				

Table 4 summaries the characteristics of each perovskite group depending of their metal cation alone. This is based broadly on literature but is only a rough display of the differences. The cost characteristic takes into account the market price of each chemical element as well simplicity of fabrication [52]. It highlights that lead-free perovskites could be more suited to commercialisation than lead-based perovskites. There may be a point where it becomes worth compromising the lower efficiency for higher sustainability in lead-free perovskites.

Sn	Sb
Pb	Bi

Tin-based perovskites are achieving good results and are the closest lead-free perovskite to competing with lead-based MAPI. This is partly due to tin perovskites generally having low energy bandgaps. $MASnI_3$, $CsSnI_3$, and $FASnI_3$ have bandgaps lower than $MAPbI_3$ with 1.3eV, 1.3eV and 1.41eV respectively – maximising the photons absorbed from sunlight [43][53][54]. The first attempt at synthesising and characterising $MASnI_3$ was published in 2014 showing the tin-based perovskite could yield a PCE of 6.4% [55]. Following this, attempts were made with $FASnI_3$ and $CsSnI_3$, but no improvement to PCE was achieved. $CsSnI_3$ has yielded a PCE of 4.81%, using an excess of SnI_2 combined with reduced atmosphere [53]. $FASnI_3$ yielded ≈4.8% PCE with the use of a SnF_2-pyrazine complex [56][54]. In 2016 QR (quantum rods) technology was used to enhance the PCEs of caesium tin perovskites. This showed huge potential with $CsSnI_3$ reaching 12.96% in QR form [39]. In 2018 a high efficiency of 9.6% was achieved without the use of QR on a hybrid tin perovskite with the composition $GA_{0.2}FA_{0.78}SnI_3$ and 1% of an additive $EDAI_2$ (GA=guanidinium, FA=formamidium, $EDAI_2$=ethylenediammonium diiodide) [57].

The significant downfall of tin based perovskites is they often short-circuit even though regarded as semi-conductors. This is because of spontaneous hole carrier doping that occurs from easy oxidation of Sn^{2+} to Sn^{4+} [56]. This undesired oxidation leads to lower V_{oc} and high carrier recombination [57]. It is suggested that SnX_2 [58] or SnX_3 [53] can help reduce the p-conductivity and make the perovskite less likely to short-circuit [53]. In addition, there is an idea that an excess of SnX_2 leads to improved air stability [58]. Another source suggests depositing uniform and dense perovskite layers is essential to reduce Sn^{4+} ions [54]. If tin perovskites are used, the toxicity of Sn^{4+} cations should be studied further, especially considering a source reports tin ions are more toxic than lead [59]. The Sn^{2+} oxidation is also to blame for the tin perovskites having poor atmospheric stability [30].

Sn	Sb
Pb	Bi

Antimony-based halides are other potential absorbers that are experiencing an increase of interest. Although they have not been shown to operate with higher PCE's than 4%, they offer a non-toxic material that does not bring rise to shorting problems that are present in tin absorbers.

Efficiencies for antimony perovskites are mostly low - around 0.5% as reported with $(CH_3NH_3)_3Sb_2I_9$ in a planar cell [44]. The highest PCE for an ABX_3 antimony perovskite is currently 3.08% with $MASbSI_2$ as the absorber [47]. Trials with mixed halides have been explored and a PCE of 2.19% was achieved with $MA_3Sb_2Cl_1I_8$ [60]. A higher efficiency of 3.8% has been achieved with a perovskite-like absorber – bromoantimonate which has the structure ABX_6 [40].

Sn	Sb
Pb	Bi

Bismuth-based perovskites are non-toxic and have PCEs in a similar range to the antimony-based perovskites. One of their other advantages is good stability in photovoltaic behaviour. This is attributed to minimal degradation during ageing and exposure to environmental conditions [61]. They are rarely considered to be the future of solar cells because their PCE remains too low [62]. The highest documented efficiency for bismuth lead-free perovskite has been achieved with $(CH_3NH_3)_3Bi_2I_9$ - a maximum efficiency of 3.17% [41]. This result was merited to the absorbing material having homogeneous surface coverage, improved stoichiometry, reduced metallic content in the bulk and desired

optoelectronic properties [41]. This investigation demonstrated that BiI_3 could be converted into $(CH_3NH_3)_3Bi_2I_9$ perovskite using a vapour-assisted solution process. $AgBi_2I_7$ and Ag_2BiI_5 contain silver instead of the methylammonium cation and the PCEs recorded were lower: 1.22% and 2.1% respectively [49] [50]. There is useful evidence that $Cs_3Bi_2I_9$ perovskite can be synthesized in ambient conditions and show stable performance [48]. This perovskite has also been compared with $(CH_3NH_3)_3Bi_2I_9$ and the measured PCE was higher by a factor of 9 (1.09% compared with 0.12%) [48]. The idea of using double perovskites (materials with the composition $A_2B'B''X_3$) looks promising from a study with bismuth as a lead alternative where $Cs_2AgBiBr_6$ achieves 2.43% PCE [63]. This is the second highest PCE found for a bismuth perovskite.

Summary of germanium perovskites

Ge	
Sn	Sb
Pb	Bi

Germanium is another element that can be substituted with lead perovskites. It is reported to have low acute toxicity [64], and germanium perovskite bandgap values are suitable [65]. However, this material is rare, so immediately it is the least economic option of the lead-free possibilities. The material requires expensive refinement techniques to be suitable to use [66]. Multiple problems have been reported involving chemical instability and oxidising tendencies in a similar way to tin [67][29]. Generally, the PCE is far behind other lead-free absorbers – $MAGeI_3$ has reached 0.2% [65].

Double perovskites and lead-less perovskites

Double perovskites are a branch of materials that are also known as elpasolites [63]. They have a very similar composition to perovskite but contain double the number of atoms so that a monovalent and trivalent cation combination replaces the divalent cation. The resulting composition is $A_2B^{1+}B^{3+}X_6$ – which is ideal for bismuth because the Bi^{3+} cation has the same number of electrons as Pb^{2+}. $Cs_2AgBiBr_6$ is a double perovskite that has stood out in literature with PCEs of 2.43% and 1.41% [63][68]. There is previous work which shows HOMO at -5.915.eV and LUMO at -3.8eV for this material [69]. Sources have demonstrated promising photo-induced behaviour with repeatable bandgaps around 2.0eV.

It is noticeable that higher efficiencies are achieved when, instead of lead-free, lead-less perovskites are synthesised. These contain reduced quantities of lead without completely eliminating it from the material. High efficiencies recorded are: 15.08% with $(FASnI_3)_{0.6}(MAPbI_3)_{0.4}$ [70], 17.78% with $FAPb_{0.95}Bi_{0.05}I_3$ [71] and 18.97% with $MA_3Bi_2I_9/MAPbI_3$ [72]. This suggests bismuth perovskites combine with lead to achieve higher efficiencies than tin combined with lead. Although this approach can achieve good optoelectronic results, the material still contains lead and is not a solution to a non-toxic perovskite solar cell. Reducing the lead content without eliminating it may not be worthwhile if the same sealing and disposal costs will still apply. Double perovskites and lead-less perovskites are considered too complex to manufacture with high repeatability and within short time frames, so are not investigated in this thesis.

In summary, there is a large variety of perovskites to investigate that can reduce toxicity issues posed by lead in MAPI. In this work, we investigate $(CH_3NH_3)_3Bi_2I_9$ (MABI) because it has low toxicity and good stability, as well as a highest efficiency of 3.17% achieved by our research group [61] [41]. Using a Kelvin probe, we can present useful information on the energy levels of MABI and directly compare with MAPI. Both perovskites can be manufactured with a highly reproducible solution processing method (meaning samples could be manufactured in short time frames in Swansea University laboratories).

MABI cells achieve much lower PCE than MAPI cells, therefore it will be interesting to investigate differences in their work function responses to light. We expect to capture a smaller work function response with MABI due to some of its undesirable photovoltaic characteristics such as:

- higher density of trapping states [73]
- larger exciton binding energy [74]
- lower carrier mobility [74]
- non-radiative recombination [74]

Other Kelvin probe measurement techniques can be used to estimate a complete band diagram [75]. This will be useful for research into the band alignment of MABI with transport layers – optimising this alignment would help to minimise carrier recombination [76]. It is suggested in literature that the PCE of MABI could reach as high as 8% with a V_{oc} of 1V [76].

1.3 Manufacturing methods in literature

It is common that from paper-to-paper the fabrication method will vary because a lot of research into perovskite solar cells is based on process optimisation of manufacturing methods. Each method will produce films with differences in layer thicknesses, grain size and surface morphology. For this reason, a summary of the variation found in literature is reported in this section.

MAPI manufacturing

Solution–processed methods involve a spin-coating step. The spin-coating step is either completed as a one-step, or two-step process. The two-step method has been shown to have better photovoltaic performance [77]. The one-step method is used in this work because it is simpler and easier to control [78]. Table 5 takes methodology information from a range of papers to show differences in this technique. Most of these examples are depositing perovskite as one of many layers which adds more complexity in comparison to the more basic FTO/perovskite samples manufactured in this work.

Table 5 - Comparative table to highlight common differences in fabrication methods across literature for MAPI using the one-step solution-processed method.

Ref	Substrate cleaning	Precursor quantities	Anti-solvent	Spin-coating settings	Annealing
[79]	Ultrasonic cleaning in detergent+deionized water. Rinse in deionized water, acetone, IPA, then plasma cleaned for 10mins	MAI 576mg PbI$_2$ 199mg +1ml solution of DMF 4:1 DMSO	200µl of ethyl acetate	30s 4000rpm	60mins at 100°C
[75]	Ultrasonic cleaning in hellmanex detergent, acetone, IPA, then plasma cleaned for 3 minutes	MAI 3:1 Pb(C$_2$H$_3$O$_2$)$_2$ DMF (400mg/ml) Hypo phosphoric acid (3ul/ml)	/	45s 2000 rpm	10mins at 0°C 5mins at 100°C
[80]	Cleaning with detergent, diluted water, acetone. Ultrasonic cleaning with ethanol for 20mins. Ultraviolet ozone treated for 15mins.	MAI :PbI2 :DMSO 1:1:1 DMF (50%wt)	500µl of Diethyl ester	25s 4000 rpm	1mins at 65°C 2mins at 100°C
[78]	Washing with soap, deionized water, acetone and ultrasonic cleaning with ethanol for 30mins, then plasma cleaned for 20mins.	MAI 1:1 PbI$_2$ GBL:DMSO (7:3 v/v)	800µl toluene	12s 1000 rpm then 30s 4000rpm	10mins at 100°C
[81]	Ultrasonic cleaning in deionized water, acetone and IPA for 30mi each, then plasma cleaned for 10 mins.	MAI 1:1 PbI$_2$ 1.2M in DMF 2:3 DMSO	500µl toluene	10s 1000 rpm then 40s 5000 rpm	5mins at 100°C

Regarding the precursor quantities, the concentration of MAPI to solvent will control the thickness of the film [82]. Table 6 shows a concentration to thickness relationship with DMF as the only solvent.

Table 6 - Thickness of MAPI perovskite layer in relation to the quantity of DMF in precursor solution [83]*.*

MAPI wt% in DMF	MAPI thickness (nm)
25	150
35	260
45	350
55	550

Table 5 only includes examples of methods that have used DMF and/or DMSO in the perovskite precursor solution. The effect of DMSO is reported by Jeon et al very clearly [84]. The anti-solvent drip leads to evaporation of DMF (or GBL), and a MAI-PbI$_2$-DMSO phase is formed [84]. This prevents the MAI and PbI$_2$ reacting rapidly. After the spin, a uniform thin film of MAI-PbI$_2$-DMSO is left. When annealed at 100°C, the DMSO evaporates and leaves the perovskite crystal.

Regarding the anti-solvent step, chlorobenzene is one option [83][82]. The other anti-solvents being used are ethyl acetate [79], toluene [84] and diethyl ether [80]. For the purpose of work function measurements, reproducibility is the most desirable film characteristic. A lot of sources acknowledge that the reproducibility is highly sensitive and dependant on drip amount, drip timing and solubility of anti-solvent [80]. Using dimethyl ether as the anti-solvent should be explored in further work because a source claims to have produced highly reproducible films regardless of the spin-coating conditions with diethyl ester [80]. It is explained that this can be achieved if enough dimethyl ether is used to dissolve the DMF [80]. It has been advised that past 7s into a spin, chlorobenzene does not have an effect, possibly due to the precursor beginning to dry [82]. This source suggests an optimal delay time for chlorobenzene is 4-6s which is significantly less than 15s practised here in. It could be due to a different spin speed used (5000 rpm instead of 3000 rpm used in this work).

Regarding annealing, it is broadly recommended to anneal within the range 70-100°C [85] [86]. However there is risk of excessive or inadequate annealing time and temperature that could lead to poor morphology from uncontrolled evaporation of solvents and crystallisation of the perovskite [85] [87].

There may be a strong argument to anneal at 130°C instead of 100°C. This is because a previous study has shown that for a MAPI and DMSO mixture, a MAI-PbI2-DMSO phase and perovskite coexist at 100°C and not 130°C [84]. The idea of the DMSO requiring 130°C (60min) for the DMSO to be removed is questionable, especially in comparison to another source that advises 65°C for 1min is sufficient to remove all the DMSO after spin coating [80].

There has also been experimentation into the possibility of annealing-free methods. This is to explore reducing production costs. The results concluded that an annealing-free method was possible when using ethyl acetate but not toluene as an anti-solvent drip [78]. It has also been shown that the annealing will be required for DMF:DMSO solvent mixtures, but not for DMac:NMP mixtures [81].

MABI manufacturing

The spin-coating method is a solution-processed method. In literature MABI is often fabricated using the vapour-assisted process instead [88] [41]. The current best PCE for MABI was achieved from a film made with the vapour-assisted process [41]. There is also a report of electric field spray-assisted deposition of MABI [89]. Examples of the solution-processed method have been collected in Table 7 to show common variations in methodology.

Table 7 - Comparative table to highlight common differences in fabrication methods across literature for MABI using the one-step solution-processed method.

Ref	Substrate cleaning	Precursor quantities	Spin-coating settings	Annealing
[48]	/	MAI 2.475M : 1.25M BiI$_3$ +DMF 7:3 DMSO	20s 1500 rpm	30mins at 110°C
[72]	Ultrasonic cleaning with detergent, then deionized water, then acetone. UV/O$_3$ cleaner for 15mins	MAI BiI$_3$ 0.3ml DMF 0.7ml DMSO	10s 1000 rpm 3500 rpm +1ml toluene	30mins at 110°C
[90]	Ultrasonic cleaning with detergent, acetone, IPA	MAI:BiI$_3$ 3:2 molar ratio 2wt% + DMF	30s 5000 rpm	/
[91]	Ultrasonic cleaning with acetone, deionized water+hellamenex, IPA at 50°C. then plasma cleaned for 8mins	MAI:BiI$_3$ 3:2 molar ratio 2wt% + DMF	45s 4000	30mins at 100°C
[92]	Plasma cleaned for 40mins	2.475M MAI 1.65M BiI$_3$	20s 1250 rpm	30mins at 100 °C

Two of the above examples use DMF alone in the solvent mixture [90] [91]. When DMSO is also added, an anti-solvent drip may be required [72]. However, no anti-solvent was used in our method, which still produced photoactive MABI perovskite.

Research into the two step solution-processed method for MABI has shown better PCE in comparison to the one-step method [90]. This is similar to what was shown for MAPI [77]. It is also reported that although the thickness of MABI is not that different between one-step and two-step processes, the surface morphology and grain quality is much better for the two-step method [90].

1.4 Essential theory

This section contains the theory that the author believes is most essential for understanding the project.

Types of semiconductors

The semiconductor group of materials is split into two groups:

Intrinsic semiconductors – materials that generate free electrons and become conductors when given enough energy.

Extrinsic semiconductors – are intrinsic semiconductors that are doped with an impurity to enhance its electrical properties.

Extrinsic semiconductors can be doped in a way to make them either have an excess of electrons (n-type), or a lack of electrons (p-type). In the case of p-type, the term 'hole' is used to represent an electron vacancy.

A perovskite solar cell architecture is made up of electrical contacts either end of a sandwich of semiconductors. There is an intrinsic semiconductor between an n-type and a p-type extrinsic semiconductor. The intrinsic semiconductor absorbs the photons of light and converts the energy to electric energy – this is called the photovoltaic effect. The extrinsic semiconductors are doped to either attract or repel the free electrons. They are referred to as transport layers because they accommodate and enhance the transport of charge across the cell. Solar panels most commonly seen on building rooftops are typically made with a single p-n junction of two doped silicon wafers for the semiconductors.

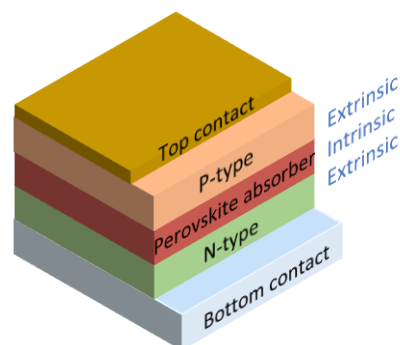*Figure 9 - A diagram of the common semiconductor layers inside a perovskite solar cell. The extrinsic semiconductor layers are often referred to as transport layers.*

Figure 9 shows how semiconductors are commonly arranged for perovskite solar cells. The p-type semiconductor is also referred to as the hole transport layer (HTL), and the n-type semiconductor is often referred to as the electron transport layer (ETL).

Band diagram terminology

Figure 10 is a typical diagram of the energy bands for a semiconductor. It is important to understand how the terminology is used throughout the thesis to describe certain energy levels.
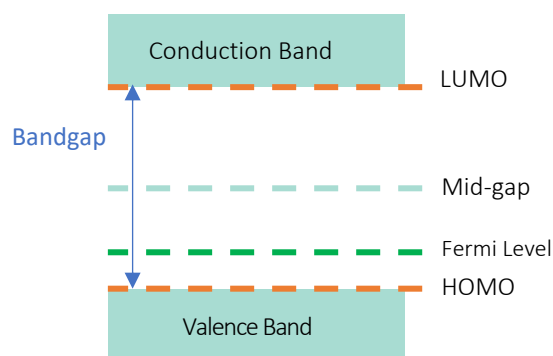

Figure 10 – Example band diagram with labels of energy levels referred to in the text.

Valence Band: A band of the electron orbitals from where the electrons of an atom can move to the conduction band when excited with enough energy.

Conduction Band: A band of electron orbitals that electrons occupy if they have been excited from the valence band with enough energy.

Bandgap: An energy difference between the highest orbital of the valence band and the lowest orbital of the conduction band. Electron energy levels do not exist within the gap, but an electron may jump the gap if it gains energy equal to or greater than bandgap.

Mid-gap: The half-way level of the bandgap.

Fermi Level: The highest energy level that any electron inside an atom occupies at absolute zero.

Lowest Unoccupied Molecular Orbital: The energy level that marks the bottom edge of the conduction band.

Highest Occupied Molecular Orbital: The energy level that marks the top edge of the valence band.

Use of HOMO and LUMO to denote the bandgap edge maybe contentious depending on whether a material is an organic semiconductor or an inorganic semiconductor [93]. Differences between these two semiconductor types in terms of energy levels is beyond the scope of the project, so for simplicity bandgap edges are denoted as HOMO and LUMO for all materials. The valence band maxima (VBM) and conduction band minima (CBM) are terms that are analogous with HOMO and LUMO in the context of labelling the bandgap edges [94].

In literature, it is common to come across the fermi level measured at ambient temperature [75][95]. This is still a detection of the maximum energy level electrons exist in, and it is measured relative to the surface potential. Where this work refers to the fermi level, it is measured at ambient temperature and relative to the surface potential.

Work Function

The **work function** is a material property that applies to atoms on the surface. It is the minimum energy required to remove an electron from a material to a point in a vacuum immediately outside the material surface. In this work it is calculated by the energy difference between the fermi level and the surface potential of a material (Figure 11).
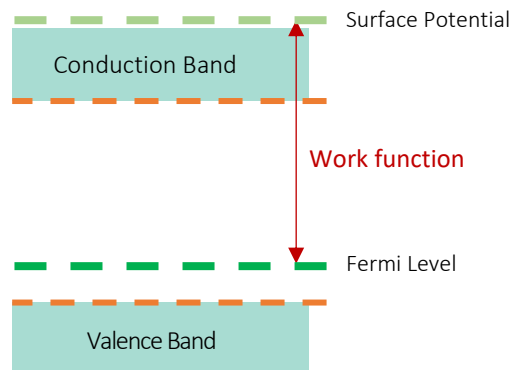
Figure 11 - Example band diagram with work function detailed as the difference in energy between the surface potential and fermi level.

The fermi level position within bandgap shows the type of doping for an extrinsic semiconductor. For intrinsic semiconductors, it shows whether the conductive behaviour is n-type or p-type.
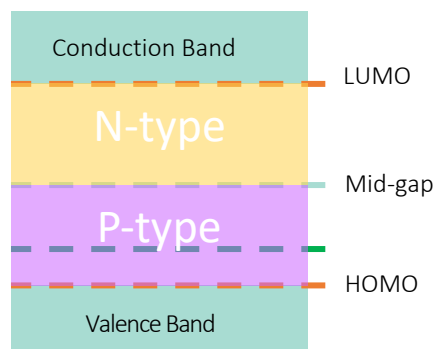
Figure 12 - Example band diagram highlighting regions that the fermi level would be located for p-type and n-type doped semiconductors.

Kelvin probe theory

The Kelvin probe measurement technique offers highly sensitive analytical surface measurements. Kelvin probes can measure the work function of a material faster than the Ultraviolet Photoelectron Spectroscopy (UPS) technique because the system operates in ambient conditions [96].

Figure 13 - Kelvin probe simplified drawing showing that the Kelvin probe tip and sample are in electrical contact. This contact equalises the differences in fermi level, creating a corresponding difference in surface potentials between the tip and sample surface.

The signal the Kelvin probe generates is called Contact Potential Difference (CPD). The CPD is a difference in surface potential that exists between the Kelvin probe tip and the sample below (Figure 13). CPD is used for a direct conversion to measure work function.
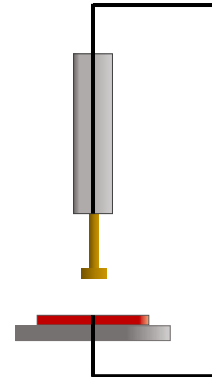
$$WF_{sample} = WF_{tip} + CPD$$
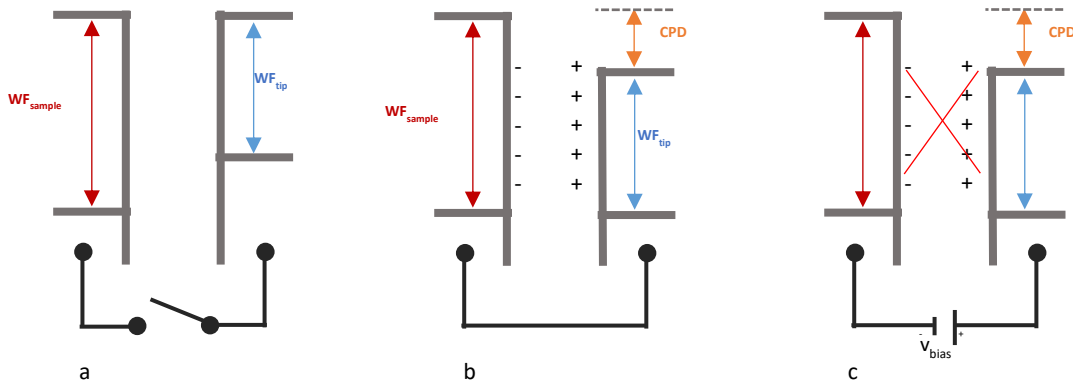
*Figure 14 - Three diagrams to explain how CPD is obtained from the Kelvin probe system. The electrical circuit shows Kelvin probe and sample **a** disconnected electrically, **b** connected electrically, **c** connected electrically with a voltage bias applied. [124].*

Figure 14a shows a representation of the energy levels when the two materials are not electrically connected. When connected, the electrons flow from the material with low WF to the material with high WF and create a potential difference between the surfaces (Figure 14b) - this is what Lord Kelvin discovered. Figure 14c shows the same situation with a voltage applied in the opposite direction. This would cancel out the field when the bias voltage equalled CPD. This is the concept used to obtain the CPD. A Kelvin probe must be vibrating continuously to measure CPD (Figure 15). Otherwise the current due to difference in work function would dissipate very quickly.
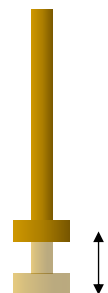
Figure 15 - Graphic of the Kelvin probe in vibrating motion.

The Off-Null Height Regulation (ONHR) method, engineered by Professor Baikie at KP Technology, is used to achieve highly accurate signals. By alternating the backing voltage and interpolating the Y intersect from two peak voltage signals, the CPD is measured (Figure 16).
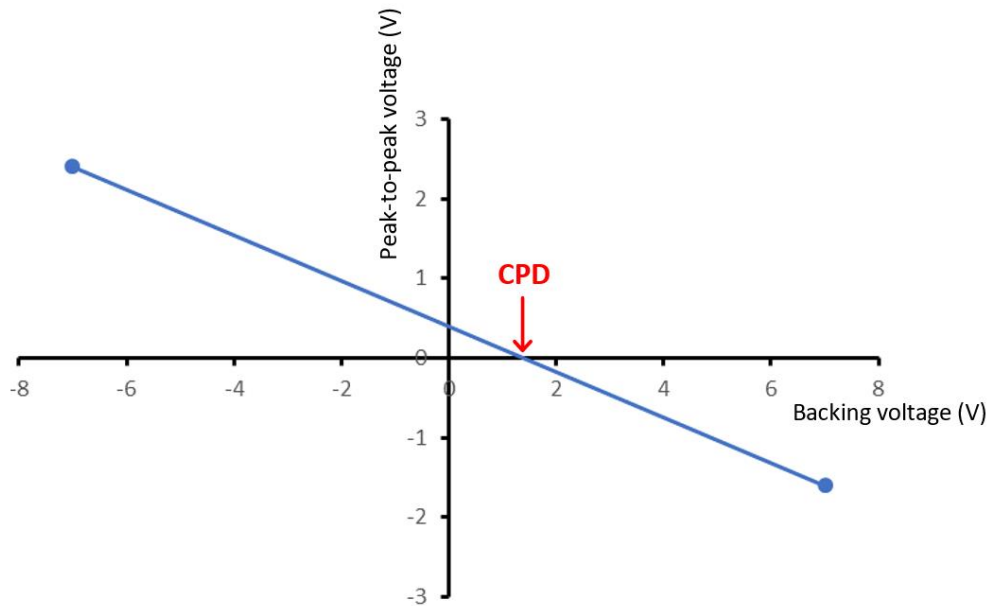
Figure 16 - Peak-to-peak voltage at +7V and -7V backing voltages to reveal the backing voltage required for the null condition (zero peak-to-peak voltage). The CPD is labelled as the backing voltage at the null condition.

Where the CPD is not obtained in vacuum conditions, measurements of work function might vary slightly from material data sheets or other measurements completed in vacuum conditions. The absolute work function of a sample is completely dependent on the accuracy of the tip work function measurement, so a reference sample of known work function is extremely important. The CPD is sensitive to many other variables during a Kelvin probe measurement, not just changes in the work function. Example of these are: temperature, pressure, resistance at electrode, wear and sample cleanliness. Awareness of these variables will help improve experimental control.

Kelvin probe measurement techniques

A Kelvin probe measures **work function** very easily. The work function is of interest because it instantly quantifies the fermi level relative to the surface. Some example tests often completed on perovskites are:

- Work function degradation with sample age
- Work function variation over sample area

Surface photovoltage is the difference in potential energy that is generated on a material surface when under illumination.

KP Technology manufactures Kelvin probes specialised for testing optoelectronic properties. Therefore, they are equipped with a light source inside a Faraday enclosure, blocking out all external radiation. With the ability to illuminate the sample during a Kelvin probe measurement, a range of surface photovoltage measurements are possible.

- Work function responses to light pulses
- Light soaking effects on work function
- Surface photovoltage (SPV) - with changing light intensity
- Surface photovoltage spectroscopy (SPS) – with changing wavelength of light
- Ambient pressure photoemission spectroscopy (APS)

The work function response to a light pulse shows the **open circuit voltage (V_{oc})** that would be generated by the absorber layer in a solar cell [75]. The SPS measurement is a method used to estimate **bandgap** by monitoring the work function change over a spectrum of light. The APS technique is sensitive to the photoemitting ability of a material. This derives the ionisation energy (or photoemission threshold) of a material which corresponds to the **HOMO level** for semiconductors, as labelled in Figure 10.

It is highly important to ensure the work function in dark conditions is being measured constantly throughout any experiment [75]. This should be used as a baseline measurement and a reference of any changes that might be time dependant due to ambient degradation [75].

Kelvin probes can measure work function and fermi level very fast. This sets them apart from the alternative UPS method often used to measure work function [96].

The **V$_{oc}$** (open circuit voltage) determines the strength of the photo-induced electric field across a solar cell. Although the transport layers generate most the V$_{oc}$, the absorber material also contributes with the electric field it generates. A material with larger V$_{oc}$ would improve the Power Conversion Efficiency (PCE):

$$PCE\ (\%) = \frac{Voc \times Jsc \times FF}{Power_{Incident}} \times 100$$

J_{sc}: $short\ circuit\ current$ FF: $fill\ factor$

The **bandgap** is important for identifying the absorber's capability to harness energy from the sun. Electrons in the valence band can only absorb energy equivalent to the bandgap because they can only excite to orbitals in the conduction band. Photons of higher energy than bandgap are still absorbed, but any energy excess to bandgap is wasted as heat through vibrational states. A smaller bandgap means a lower minimum energy is required for generation of charge. MAPI's bandgap is around 1.6eV [75], making it a very good absorber of all visible light. Other perovskites generally have a larger bandgap than MAPI. The optimum bandgap for photovoltaics is 1.3eV as per the Shockley Queissar theory [36].

HOMO level marks the bottom of the bandgap and allows LUMO to be estimated if the bandgap is known. Knowledge of HOMO and LUMO of each layer in a solar cell helps to optimise the materials by minimising energy loss. An offset in band alignment causes energy loses at the interfaces. If the transport layers have bandgaps with similar HOMO and LUMO level to the absorber material, the efficiency will improve [75] [97].

Where the **fermi level** lies within bandgap depends on how the semiconductor's doping properties (Figure 12). Extrinsic semiconductors will have a fermi level below mid-gap if they are p-type, or above mid-gap if they are n-type doped [75] [98]. Intrinsic semiconductors in dark conditions are assumed to have a fermi level at mid-gap [99]. It will change from mid-gap under illumination. The location above or below mid-gap identifies whether the intrinsic behaviour is p-type or n-type.

Minority carrier diffusion length (L$_n$) can be estimated from SPV measurements [100]. The diffusion length will only be accurate if the thickness of the material is greater than 3L$_n$ [100]. The property quantifies how far minority carriers will travel as they diffuse within the material. The following characteristics must be known or estimated to calculate L$_n$: absorption coefficient, wavelength of incident light, surface charge region width, film thickness, minority charge density and recombination velocities [100].

Chapter 2. Experimental methods

2.1 Manufacturing procedure

Easy manufacturability has made perovskite solar cells an especially hot topic for university research, as full cells can be made within one day from scratch with laboratory equipment.

a   b
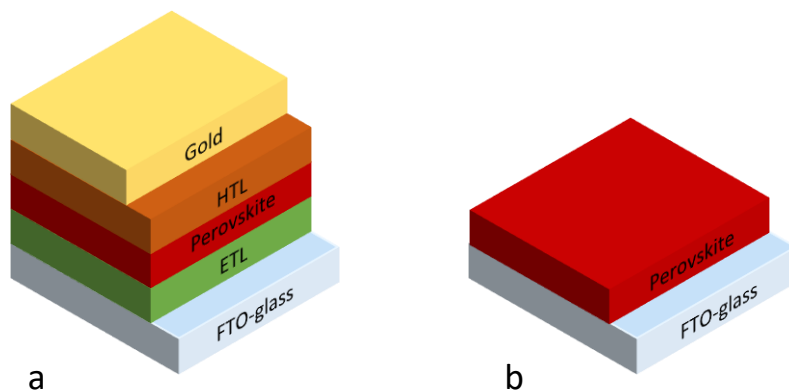
*Figure 17 - Three- dimensional model of **a** full cell architecture, **b** sample architecture. Layers deposited on top of FTO-glass substrates are defined.*

Testing in this project did not require a full cell to be manufactured as the focus was maintained on the perovskite material itself. In this work the sample architecture consists of the perovskite layer deposited on top of an FTO-glass substrate. FTO-glass is a cheaper conductive substrate than ITO-glass. The main stages of the process were:

1. FTO-glass cutting
2. FTO-glass cleaning
3. Preparation of perovskite precursor solution
4. Spin-coating perovskite solution on FTO-glass substrates
5. Annealing samples

The procedures for MAPI and MABI are kept very similar to each other to maximise control variables and ensure that differences in results are due to the materials themselves and not differences in fabrication. However, some details are different to obtain a good quality of film for each material.

1. FTO-glass cutting

FTO-glass substrates were cut to size by marking with a cutting edge (Figure 18a), followed by breaking with handheld glass cutters (Figure 18b). Marking was done on the non-FTO face to minimise damage to the FTO. Substrates varied in dimensions between 30x30x5mm and 15x15x5mm.
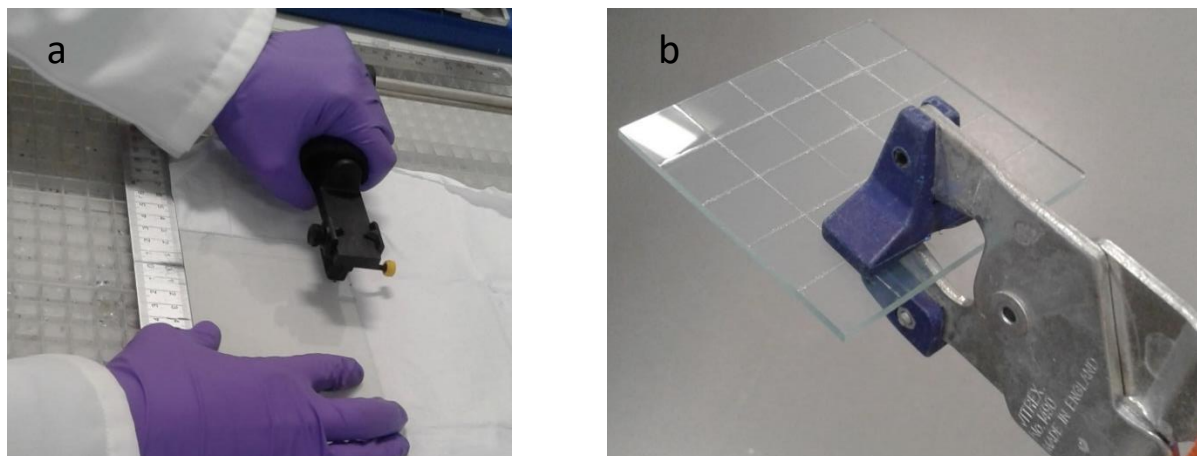
*Figure 18 – **a** Glass marking technique using linear scribing tool. **b** Using glass cutters to break FTO-glass substrate as scribed*

2. FTO-glass cleaning

Substrates were scrubbed with a mixture of Hellmanex detergent and deionized water using a toothbrush (Figure 19a). The Hellmanex detergent was used because it has good wetting action and does not leave a residue when rinsed off with more deionized water. Next, samples were mounted onto a substrate holder submerged in a beaker of deionized water and Hellmanex detergent (Figure 19b). This was placed in an ultrasonic bath and sonicated for 10 minutes at 60˚C. Then substrates were rinsed again in deionized water followed by acetone and iso-propanol (Figure 19c). They were dried individually with a nitrogen air gun.

*Figure 19 - **a** Brush cleaning individual substrates with deionized water + Hellmanex mixture **b** Ultrasonic cleaning of multiple substrates positioned on a rack that is placed in a beaker of deionized water **c** Solvent rinsing of substrates **d** Oxygen plasma cleaning of substrates.*

The final step of the glass cleaning is to remove any remaining surface contaminants with O_2 plasma cleaning. The O_2 plasma cleaning is used because it can remove organic contam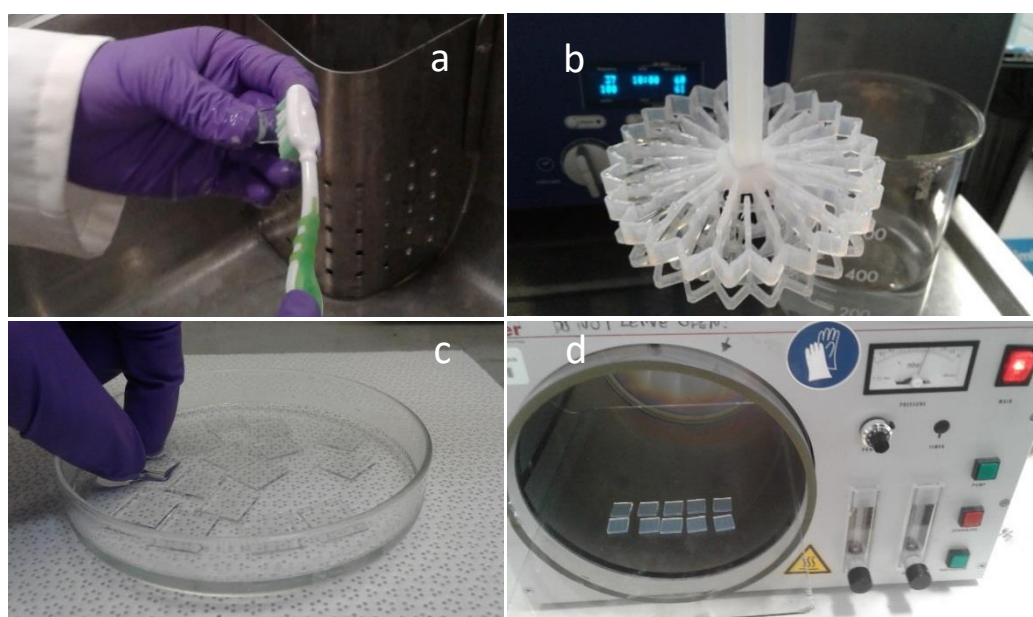inants very effectively by reaction with oxygen [101]. The samples are placed, FTO side faced up inside the vacuum chamber (Figure 19d). The pump is switched on to reduce pressure to 300mBar. At 300mBar the O_2 valve is opened to allow oxygen to leak the vacuum. The rate of oxygen flowing in should be fine-tuned to balance the pumping at 300mBar. When the pressure is stable at 300mBar with the O_2 valve open, the radio-frequency plasma generator is switched on. The samples are only exposed to the plasma for 3 minutes, being cautious of damaging the FTO surface with excessive plasma cleaning. It is known that the plasma cleaning does have an effect on the work function of FTO [102]. Cleaning the glass is a very crucial step in achieving high quality samples because the perovskite film morphology is completely dependent on what it is deposited on [103].

3. Preparation of perovskite precursor solution

To deposit the perovskite in a spin-coating process it must be in liquid form. Therefore, a precursor solution of the perovskite materials and solvents is prepared (Figure 20). Dimethylformamide (DMF) and dimethyl sulfoxide (DMSO) are the solvents used to dissolve the powders.

Methylammonium bismuth iodide:

Bismuth iodide	540mg
Methylammonium iodide	200mg
Dimethyl formamide	0.4ml
Dimethyl sulfoxide	0.6ml

40 minutes on 140˚C hotplate to dissolve

Methylammonium lead iodide:

Lead iodide	605mg
Methylammonium iodide	200mg
Dimethyl formamide	0.4ml
Dimethyl sulfoxide	0.6ml

60 minutes on 60˚C hotplate to dissolve

Figure 20 - Quantities of constituents required for MABI and MAPI perovskite precursor solutions and the dissolving time and temperature.

The mixtures are filtered through 0.2µm syringe filter tips to remove any solid excess left in the solution. The solution is now ready for spin coating.

4. Spin-coating perovskite solution on FTO-glass substrates

The spin-coating step was completed in a glove box under a nitrogen-purged atmosphere. The nitrogen purging is very important because it keeps O_2 and H_2O levels down, which minimises oxidisation of the metal cation during spin-coating and annealing. The spin coater settings were the same for both perovskites:

Duration: 30s

Speed: 3000 rpm

Acceleration: 3000 rpm/s

The substrate is held down during spinning by a vacuum seal on the base of the substrate. The O-ring on the chuck was switched depending on the substrate size: for 15x15mm substrates, the small O-ring was required; for 30x30mm substrates, the larger O-ring was used (Table 8, Figure 21a).

The volume of perovskite solution deposited on the glass substrate before spin coating was 50µl and 100µl for 15x15mm and 30x30mm substrates respectively. The procedure for MAPI involved releasing chlorobenzene as an anti-solvent over the perovskite after 15s of spinning. The chlorobenzene volume used was 150µl and 300µl for the $15mm^2$ and $30mm^2$ substrates respectively (Table 8).

Table 8 - Differences in the spin-coating method that were dependant on the substrate size.

	Substrate size	
	15x15mm	**30x30mm**
O-ring size	small	Large
Perovskite solution (ml)	50	100
Anti-solvent drip (MAPI only)	150	300

*Figure 21 - **a** Spin-coater chuck with detail on O-ring size. **b** Nitrogen atmosphere glove box used for spin-coating.*

5. Hotplate annealing

After spin-coating, the samples were transferred onto a hotplate within 1 minute of the spin ending. The annealing times and temperatures were different for the two perovskites (Figure 22). The MAPI perovskite annealing involved two hot-plates (for two different temperatures) whereas the MABI annealing was carried out with one hot-plate. This was done to achieve controlled evaporation of solvents and better crystallisation for each material, which, in this case, meant different methods were required.
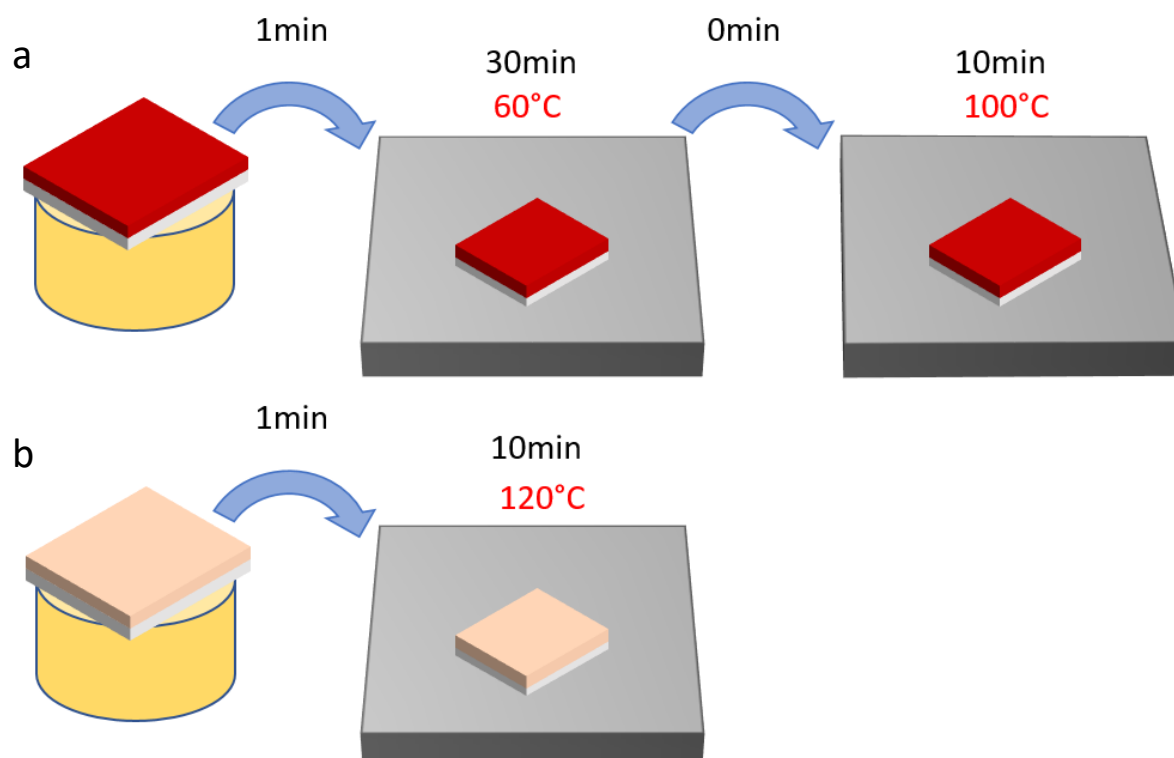

*Figure 22 - Hot-plate annealing methods for **a** MAPI and **b** MABI*

2.2 Instruments and equipment

Kelvin probes

KP Technology design and manufacture Kelvin probes for the world's leading institutions. Data in this report comes from three KP Technology Kelvin probe systems (Figure 23): the KP020 system at Swansea University; APS04 system at KP Technology; and UHV system at KP Technology.
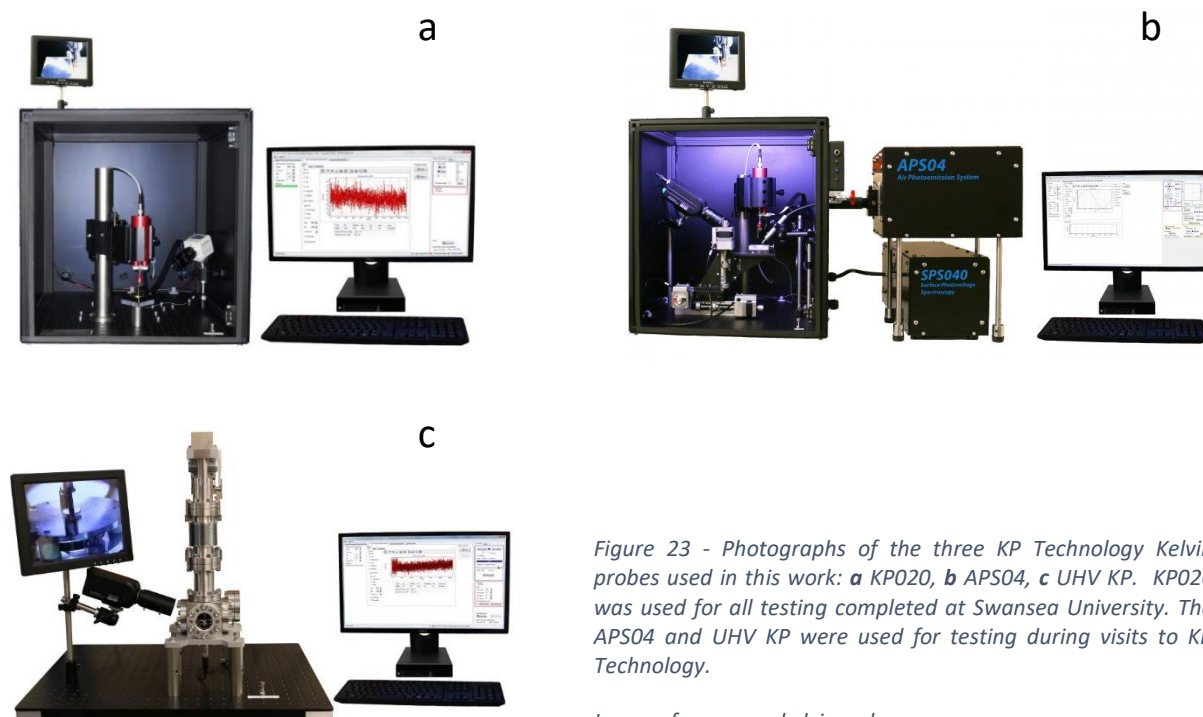

Figure 23 - Photographs of the three KP Technology Kelvin probes used in this work: **a** KP020, **b** APS04, **c** UHV KP. KP020 was used for all testing completed at Swansea University. The APS04 and UHV KP were used for testing during visits to KP Technology.

Images from www.kelvinprobe.com

The main setup steps for all three systems are:

1. Calibration of the tip. This involved calculating the WF_{tip} using a reference material of known work function e.g gold wafer or highly ordered pyrolytic graphite (HOPG).
2. After the tip has been calibrated, a sample is mounted below probe tip.
3. The probe vibration is switched on and it is lowered closer to the sample by manual adjustment until it can pick up a strong signal of surface potential.
4. A voltage signal is generated using the off-null height regulation (ONHR) method. The voltage signal is the Contact Potential Difference (CPD), which is equivalent to the difference in work function between the tip and the sample. For a known tip work function the following equation derives the sample work function:

$$WF_{sample} = WF_{tip} + CPD$$

5. The CPD is measured under desired conditions.

All the hardware and capabilities of the KP020 are also present with the APS04. The APS04 system is capable of three additional measurement techniques:

- Scanning CPD measurement – the Kelvin probe maps work function over a horizontal area by translating on two axis with stepper motors.
- Ambient photoemission spectroscopy (APS) – photoemission is detected at the Kelvin probe whilst the sample is illuminated with spectroscopic ultraviolet light.
- Surface photovoltage spectroscopy (SPS) – CPD measurement with spectroscopic visible light.

Each of these techniques can be carried out simultaneously without disturbing the ambient environment within the Faraday enclosure. For ambient photoemission spectroscopy, the APS04 system provides deep ultraviolet light from a deuterium source which requires a volume of nitrogen gas to supress ozone production in the external APS unit [104]. This was achieved by purging the volume inside the external APS unit with nitrogen from a gas cylinder. Spectroscopic light enters the Faraday enclosure through optical fibres attached to separate external units for APS and SPS (Figure 23b).

The UHV Kelvin probe is a system designed to offer work function measurement of samples in a high-quality vacuum. The system design includes an enclosure of much smaller volume to lower the pressure faster. The probe is lowered before lowering the pressure. Substrate size was reduced from 30x30mm to 15x15mm in order for it to fit through the opening of the enclosure. The enclosure itself allows light in through small glass windows, but therefore it does not have shielding from electromagnetic waves, so achieving a high-quality dark environment is very challenging. Our dark measurements were completed in a room with no windows and the lights switched off. To illuminate the sample, a quartz tungsten halogen lamp (same as installed in KP020) was positioned by an enclosure window.

Note: all three systems were setup with a 2mm diameter gold tip.

Detailed guide of KP020 Kelvin probe operation

The following is a detailed guide to how a typical Kelvin probe measurement was completed for the KP020 Kelvin probe at Swansea University. Refer to Figure 24 for labelling of parts.
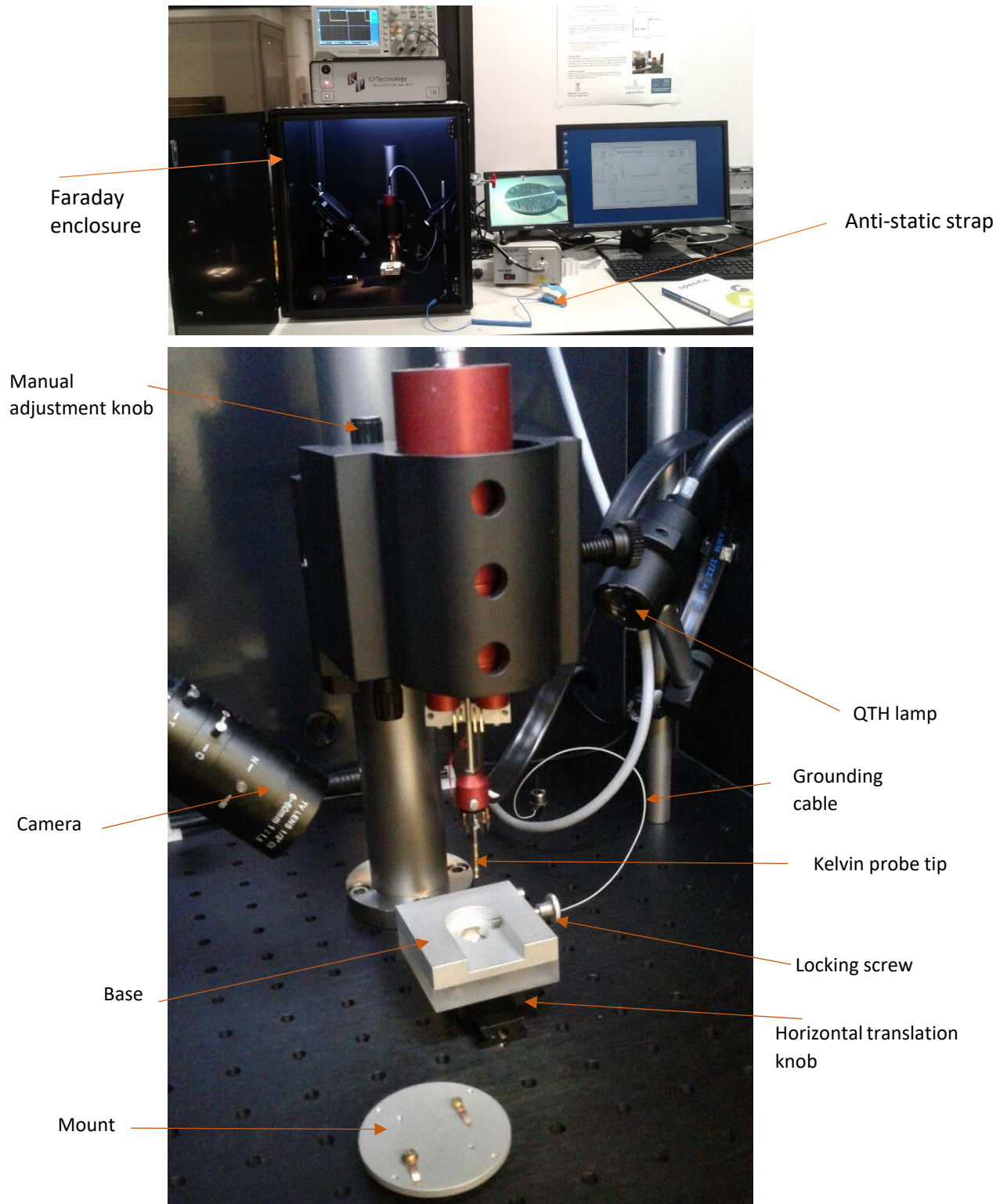

Figure 24 - Photo of inside the KP020 Kelvin probe with labelling of components

Step 1. Mounting the sample

The Faraday enclosure is opened, and the antistatic-cable is connected to the operator's wrist. The sample is fixed onto the mount by a grounding method which holds the sample in place whilst also electrically grounding the surface to the base below. This method improved with time, evolving from basic conducting aluminium tape to fastened copper flexure clips (Figure 26, Appendix C Figure 82). For a perovskite sample, it is essential to scratch away an area to expose the conductive FTO layer below for electrical grounding (Figure 25). The probe tip is raised manually to at least 30mm above the base to allow room for slotting the mount and sample into place without knocking against the probe tip. The sample is always placed with the perovskite layer facing up towards the probe. To lock the mount and sample in place under the probe, the locking screw is tightened. If a non-conductive oxide layer has formed on the mount, the locking screw will pierce through it.
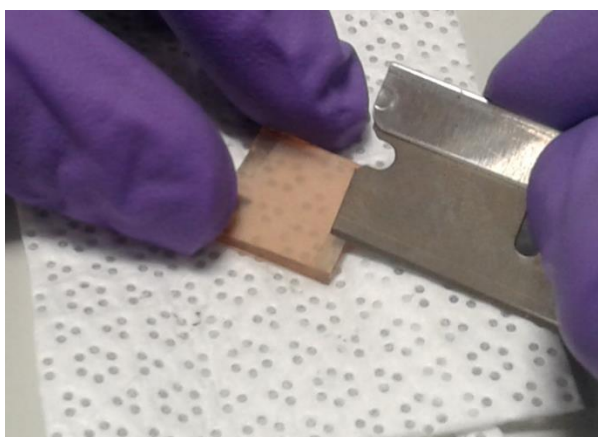

Figure 25 - Scraping off strips of the perovskite layer at the edges of a sample to expose fully conductive FTO for grounding the sample.
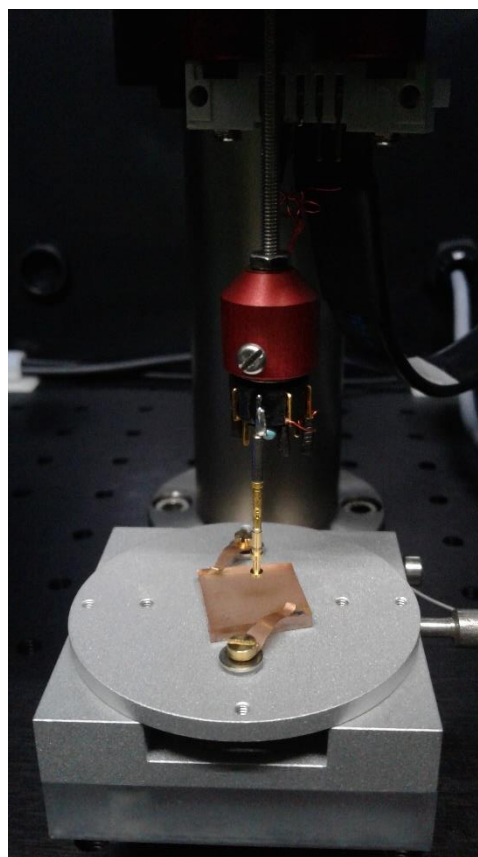

Figure 26 - The Kelvin probe set-up with the improved sample mount and copper flexure clips to over-come grounding issues.

Step 2. Lowering the Kelvin probe

The Kelvin probe is enabled and begins vibrating. A voltage signal is displayed on the logging interface. The manual adjustment knob is twisted clockwise to lower the probe towards the sample surface. As the tip approaches past 5mm above the sample the CPD signal to noise ratio should be low (Figure 27a). If a waveform like Figure 27a is not distinguishable, then there is likely an error with the mounting setup (Appendix C Table 27). After the peak-to-peak voltage of the signal reaches over 600mV, the waveform should appear sinusoidal, like Figure 27b. The optimal distance between the probe and sample is around 1mm mean distance, with a peak-to-peak vibration amplitude of 0.46mm [104]. This corresponds to a reading of 300 arbitrary units of the "Gradient" variable within the software. To achieve this without making accidental contact with the sample, gradual manual lowering is required before fine tuning can be done with automated controls. Next, the antistatic strap is detached, and the enclosure door is shut.

For a light sensitive sample like perovskite, the room lights were switched off for Step 1 and Step 2 to avoid long decay time for the fermi level of the material to reach dark equilibrium.
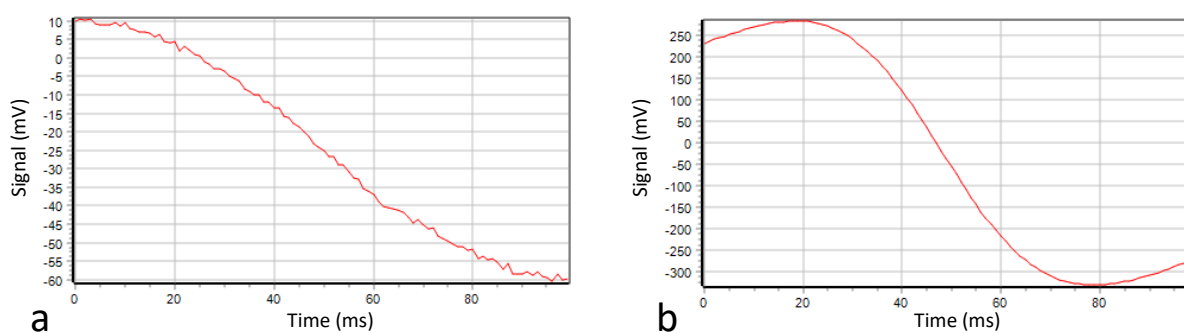

*Figure 27 - The raw voltage signal monitored during lowering of the Kelvin probe **a** when the tip is around 5mm above the sample, **b** when the peak-to-peak voltage surpasses 600mV.*

Step 3. Completing a measurement

The signal averaging is set to 30 to minimise the noise and random errors captured. There are two measurement functions with the KP020 software. These can be opened with the "Work function" tab, or the "Surface photovoltage" tab on the software. The work function measurement logs a CPD measurement and the surface photovoltage measurement logs the CPD whilst illuminating the sample with white light of increasing intensity. The light can be switched on manually during a work function measurement to capture the CPD response to illumination at chosen times. For any measurement involving illumination, the QTH light source must be switched on first. The manual intensity adjustment knobs on the QTH light source were always left in the default position (1 o'clock). To change the intensity, the automated controls on the software interface were used. If intensity is not specified for a light measurement in the results chapters, the default intensity of 5000 AU should be assumed. To convert to a lux scale, luxmeter measurements were taken for the intensity scale 0-5000 AU in steps of 500 AU (Table 14).

The CPD of any sample will always be changing by some amount due to natural changes in the environment and material. For photoactive samples there will be a period of decay once the Faraday enclosure is closed due to light pollution affecting the material before entering the enclosure. This decay period is completely material dependant. For the MAPI and MABI samples tested it was roughly 20 minutes as shown in Figure 28. As a rough convergence criterion, the CPD was rounded to nearest mV once the change in running average was smaller than 1mV/minute.

Other equipment

Most of the measurements in the results chapters were completed with the Kelvin probes. However, other instruments were used to characterise the samples further and provide more information. Information on the other equipment used can be found here.

UV-visible Spectrometer:
A UV-visible spectrometer is used to characterise the samples' light absorption and estimate bandgap. The instrument used was a Perkin Elmer Lambda 9 UV/VIS/NIR spectrometer. The instrument provided another method of estimating bandgap to check against the Kelvin probe SPS method as reported in Section 4.6.

Photoluminescence:
Photoluminescence measurements show the wavelength and intensity of light that samples emit when they fluoresce or phosphoresce. The instrument used is a Horiba FluoroMax. Data from the photoluminescence measurements were used in preliminary testing for degradation with heat exposure (Appendix B Figure 79).

X-Ray Diffraction:
The XRD is used to characterise the composition of the samples and show diffraction peaks that suggest the samples have perovskite structure. The XRD also detects materials underneath the top layer, especially in the case of perovskite thin films that are less than 1 μm thick. The instrument used was a Bruker D8 Discovery. The XRD plots are shown in Appendix A. This is an area that could have been looked into in more detail with repeat measurements and further analysis of peaks.

Profilometer:
Film thickness is a very important variable to measure for the manufactured perovskite samples. The procedure is slightly different for the two perovskites, so a difference in thickness is expected. Thickness of the photoactive layer plays an important part in charge transport as it determines the distance between the FTO-perovskite interface and the sample surface. It is important to note that the two perovskites manufactured in this work has different thickness. This was not intended and in future work the spin-coating settings for MABI will need to be optimised to achieve 500nm thickness. The instrument used to measure the film thickness was a Bruker Dektak 6M. The profilometer plots are shown in Appendix A.

2.3 Experiment plan

Experiment aim

The aim for the thesis experimentation was to characterise the two perovskite materials, MAPI and MABI, with a Kelvin probe to learn more about their differences and why MAPI performs much better in a solar cell.

Measurement targets

1. Obtain a baseline work function measurement to address a variation due to ageing and manufacturing inconsistency of the samples.

With our sample architecture, the perovskite layer is exposed and therefore likely to react with O_2 and H_2O during storage so a work function aging trend is expected. The manufacturing procedure is simple but involved lots of steps that will inevitably introduce variation between samples which also needs to be quantified. This data is presented in Chapter 3.

2. Carryout measurements required to obtain fermi level, bandgap and HOMO level for the samples.

These are the measurements required to construct a band diagram for the two types of sample with measured energy values. The band diagram will tell us the where the fermi level lies within the bandgap. A comparison of the energy levels to those on band diagrams in literature will provide useful information on how our samples may be different. This data is presented in Chapter 4. Understanding the FTO-perovskite interface requires plain FTO measurements for the band diagrams. The FTO fermi level is important because it will have a strong influence on the perovskite fermi level.

3. Change in work function and band bending under illumination.

Work function light response measurements will show where the fermi level shifts to on the band diagram once under illumination. Using the band diagrams, a model of a band bending mechanism through the perovskite thickness can be shown. This data is presented in Chapter 4.

4. Investigate differences in the light response between the samples with light pulse cycling and varying light intensity.

These measurements will characterise the perovskites' ability to generate voltage under different light conditions. It is expected that MAPI will out-perform MABI and demonstrate a much larger open circuit voltage with larger surface photovoltage measurements.

5. Investigate differences in photoactive behaviour in different environmental conditions e.g. under vacuum, nitrogen atmosphere, heat exposure, humidity levels.

All previous testing will have been completed in ambient conditions. Carrying out measurements in other types of environments will reveal more advantages and disadvantages of the two perovskites, in particular, with stability. Due to time constraint, not all of these conditions could be investigated under the scope of the thesis. A first iteration of testing under vacuum and nitrogen atmosphere was completed.

These targets also became an order of hierarchy so that Target 1 had to be met before Target 2. Completing the measurements in this way minimised gaps in understanding of the samples.

Reporting the results

The results and discussion for this thesis are reported across Chapters 3, 4 and 5.

Chapter 3 covered the results for the baseline measurement. (Target 1)

Chapter 4 is the main results chapter. This includes description of all the measurements carried out to obtain energy band diagrams and detailed analysis on the differences between MAPI and MABI. The chapter goes into detailed analysis of behaviour of MAPI and MABI under illumination and discussion of models proposed to explain photoactive behaviour. (Target 2, Target 3 and Target 4)

Chapter 5 reports results from measurements under vacuum and nitrogen atmosphere. The hypothesis is that in ambient conditions oxygen dopes the perovskite, therefore when the oxygen is removed from the atmosphere, a corresponding shift in the fermi level can be measured. The results are a first iteration of measurements so the findings reported required further testing. (Target 5)

Chapter 3. Baseline measurement

3.1 Summary

Perovskites are intrinsic semiconductors, which means the work function changes when the material absorbs light. A baseline measurement of dark work function provides a reference of dark equilibrium to compare to. Variation in a dark baseline measurement will likely be due to:

- samples being slightly different from one to another giving rise to batch uncertainty
- samples degrading with time
- samples that are especially slow to adjust from room light to dark conditions

Dark work function measurements were carried out on MAPI and MABI to address each of the points above. Work function measurements found in literature are listed below in Table 9.

Table 9 - Work function values from literature to be used for reference of reasonable dark work function values.

Sample	Work Function (eV)	Instrument	Reference
Lead based			
FTO/MAPbI$_3$	5.1	Kelvin probe	[95]
FTO/MAPbI$_3$	5.1	Kelvin probe	[75]
Bismuth based			
MA$_3$Bi$_2$I$_3$	5.52±0.054	Kelvin Probe	[105]
MABi$_3$I$_{10}$	5.11	UPS	[106]

3.2 Dark equilibrium

The work function measurement of a photo-sensitive sample will always have a decay function to the dark equilibrium because the sample is mounted with the Faraday enclosure open (Figure 28). Even if the lights in the room are switched off the sample will absorb enough light to shift the fermi level.
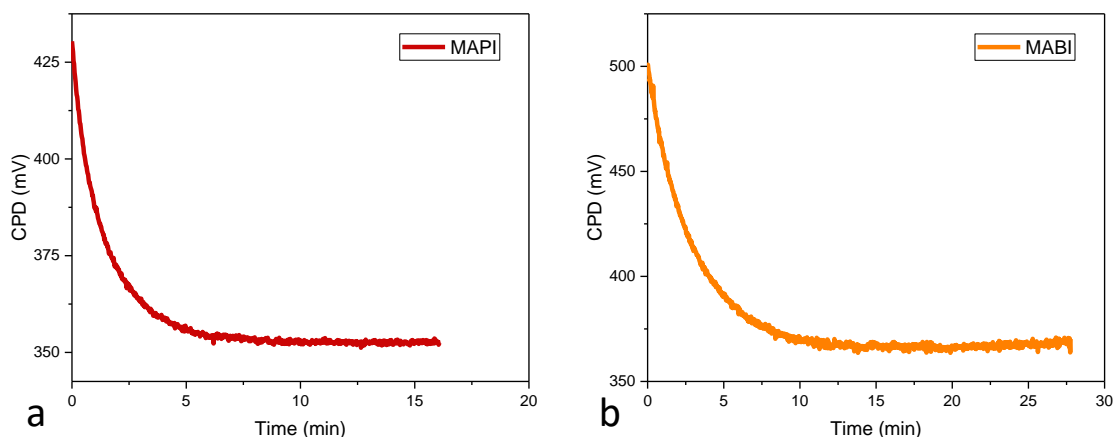
Examples of dark equilibrium decays:

*Figure 28 - Kelvin probe measurement of CPD reaching an equilibrium in dark conditions for **a** MAPI, **b** MABI. The samples were mounted in conditions of minimal light.*

3.3 Manufacturing repeatability

Before carrying out any comparative experiments, it was important to measure how much the dark work function varied across samples that were manufactured the same way to quantify manufacturing reproducibility.

For each batch, any film that had large visual defects across the surface was not measured. The age of the samples was monitored with each sample being measured multiple times over 7 days to show time-dependant degradation.
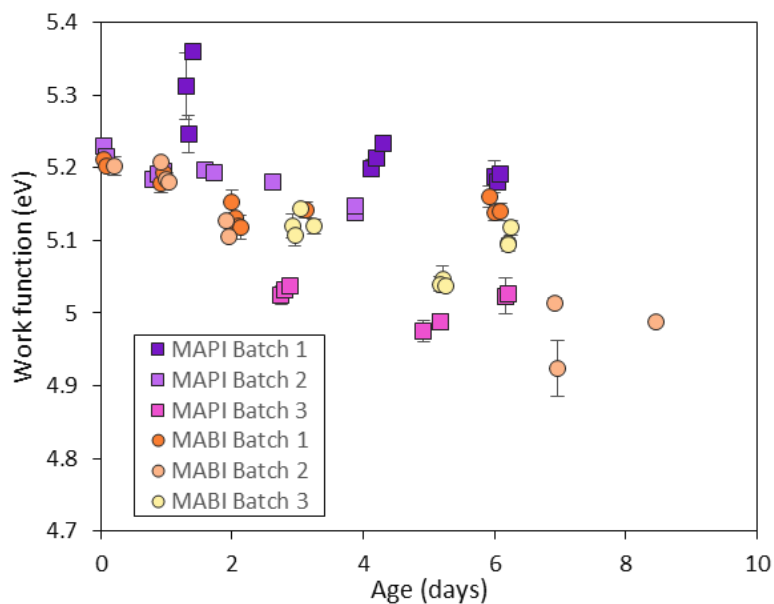

Figure 29 – Dark work functions of MAPI and MABI samples from different batches showing change with age as well as manufacturing-induced variation.

The data includes multiple samples from different batches to prove a robust manufacturing method is being practised. Batches are shown in different colours to highlight that it is the main cause of variation in MAPI. The MABI batches overlap better showing the manufacturing process is more repeatable. It is likely the source of this is the anti-solvent dripping step where chlorobenzene is deposited on MAPI during spin-coating. This step is not a part of the MABI procedure.

With the exception of the early points of MAPI Batch 1, the variation across samples within a batch at the same age is very small. Both perovskites have negative gradients with increasing age. The rate is approximately -0.2eV in 7 days. This shows that there is an ageing relationship with work function. The good news is that the gradient is very similar between all batches of both perovskites, showing the ageing is reliable. Although MABI is expected to have better stability, it is not obvious in the 7 days of work function lifetime. The error bar values were calculated by the sum of ±0.003eV for instrument resolution; ±0.001eV for rounding from convergence and the standard deviation from two locations measured for each data point. The long-term stability of the work function is explored next.

3.4 Long-term work function ageing

Here the work function ageing of the two perovskites has been measured over almost 60 days (Figure 30). Previous examples of the stability of MABI have only been found for PCE, not work function [76][41][61][74][106]. The samples were stored in a black ESD container. The average values show that MAPI is more effected by ageing in terms of work function (Table 10). The MAPI work function decreases by over 0.2eV, whilst the MABI decreases by less than 0.125eV.

Table 10 - Summary table for work function ageing over 60 days for MAPI and MABI.

	Start	Finish	Change in WF (eV)
MABI	5.375	5.25	0.125
MAPI	5.29	5.075	0.215

These numbers are in line with the expectation that MAPI is a less stable film when exposed to atmospheric conditions. MAPI work function values decrease more with age, backing up the claim that MABI has better stability characteristics.

The vulnerability of MAPI to degradation due to oxygen and light is well documented [107] [108] [109][95]. Oxygen diffusion is reported to saturate a 500nm film in 10 minutes and lead to structural degradation of the perovskite in a timescale of days [107]. Photo-induced degradation has been heavily linked with work function degradation and causing different charge carrier dynamics [95]. With this considered, the work function change over almost 60 days in atmospheric conditions is actually smaller than expected. Take notice of how the degradation of work function over 60 days (Figure 30) does not match well with the data for 7 days (Figure 29). This is likely due to poorer storage conditions for samples during the 7 days measurements (a better container was used for the 60 days measurements). Hence, Figure 29 has a faster rate of work function degradation.
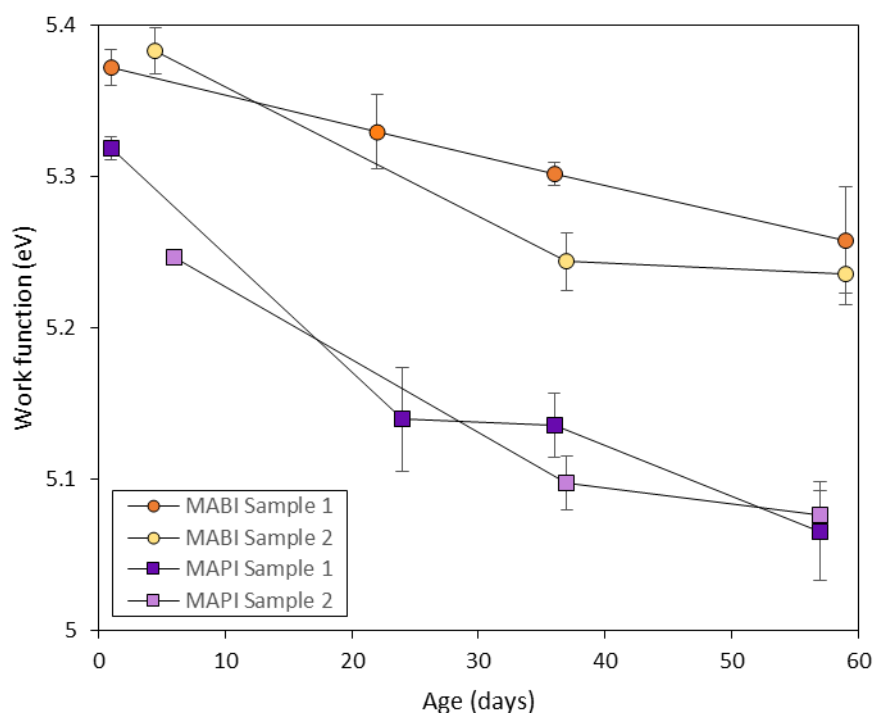

Figure 30 - Long-term dark work function ageing of MAPI and MABI measured from two samples of each perovskite. Samples were stored in an ESD container shielded from visible light.

In terms of work function, it is possible that photo-induced degradation has a greater impact on work function ageing than oxygen diffusion and humidity levels in the environment. This hypothesis comes from observations of our MAPI samples turning yellow when left outside of a light-shielding container. The samples stored for 60 days in a light-shielding container had no signs of yellowing. Humidity levels are considered to be strongly linked with degradation, however the degradation of MAPI due to moisture has been shown to be minimal where oxygen is not present [109]. A publication shows the photo-induced degradation of MAPI work function is rapid (0.4eV/20mins) and linked with modulation doping by the PbI_2 phase [95]. We report a work function degradation trend in the opposite direction (Figure 30). This should be investigated in further work.

Chapter 4. Understanding the differences in energy levels between MAPI and MABI in darkness and under illumination

4.1 Summary

This chapter is the analysis of the measurements completed to obtain band diagrams and light responses for the two perovskites. MAPI and MABI are compared as thin-film photoactive layers deposited on top of an FTO-glass substrate. In collaboration with KP Technology, measurements of fermi level (Section 4.4), highest occupied molecular orbital (HOMO) (Section 4.5) and bandgap (Section 4.6) are obtained with an APS04 Kelvin probe system. A detailed analysis of MABI in this way has not been done before.

The chapter gathers energy level data that is summarised as a band diagram for each perovskite with FTO as a conductive layer underneath (Section 4.3). The derivation and analysis of each energy level is reported through Sections 4.4 to 4.6. Following this, the chapter explores the intrinsic properties of MAPI and MABI by measuring the change in work function under illumination (Sections 4.7 to 4.9). It is demonstrated that MAPI and MABI have very different responses to light. Under white light illumination, MAPI experiences an increase in work function of 250meV and MABI experiences a decrease of 40meV. The response of MAPI is sharp and consistent, delivering a highly repeatable CPD rise in less than 20 seconds. The response of MABI is more complex than MAPI and the decay that follows is much slower. Explanations for these differences are explored and discussed throughout.

4.2 Measurement techniques used

All the measurement techniques in Table 11 are obtainable simultaneously without requiring any manual instrument adjustment. However, a dark work function equilibrium is always required between each measurement.

Table 11 - Summary of the measurement techniques completed in this chapter and the associated data extracted.

Measurement technique	Data extracted
Dark work function scan (SKP)	Fermi level variation across the sample face
Ambient Pressure photoemission spectroscopy (APS)	HOMO level
Surface photovoltage spectroscopy (SPS)	Bandgap measurement
Surface photovoltage (SPV)	Fermi level response variation with light intensity
Light pulse cycling	Fermi level response variation with time

For measurements involving illumination, the sample is radiated from the perovskite side as shown in Figure 31.
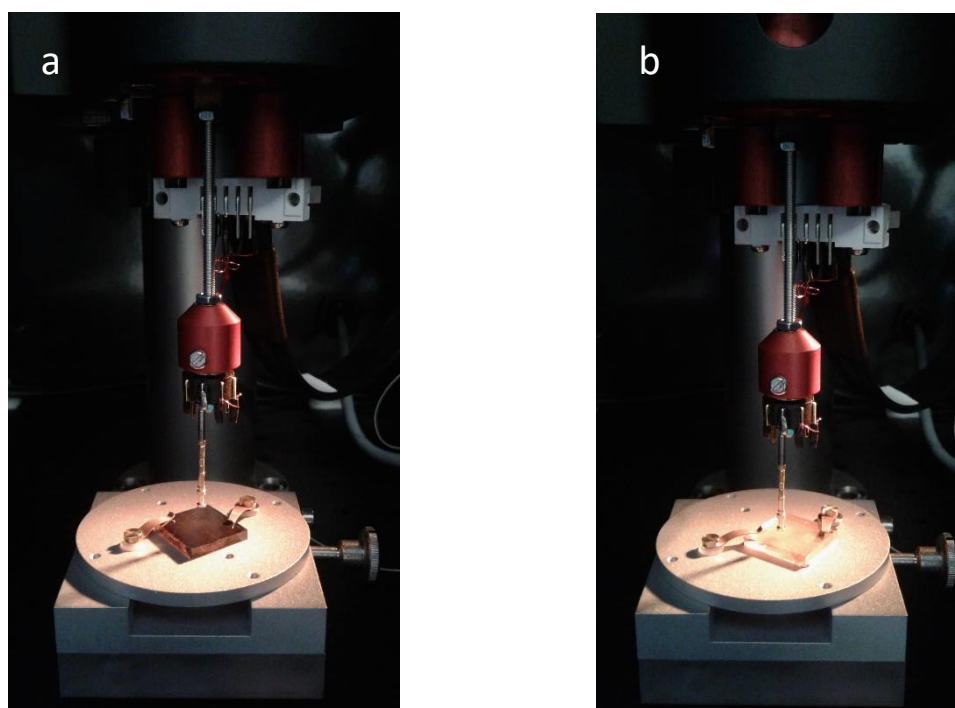

*Figure 31 - Photographs of samples mounted inside Kelvin probe with illumination directed on the top face of the sample. **a** MAPI, **b** MABI*

4.3 Band diagrams

A band diagram provides an effective way to visually compare the different energy levels of the two perovskites (Figure 32). It is important to assess the influence of FTO on the energy levels because the junction between the two materials causes complex behaviour.
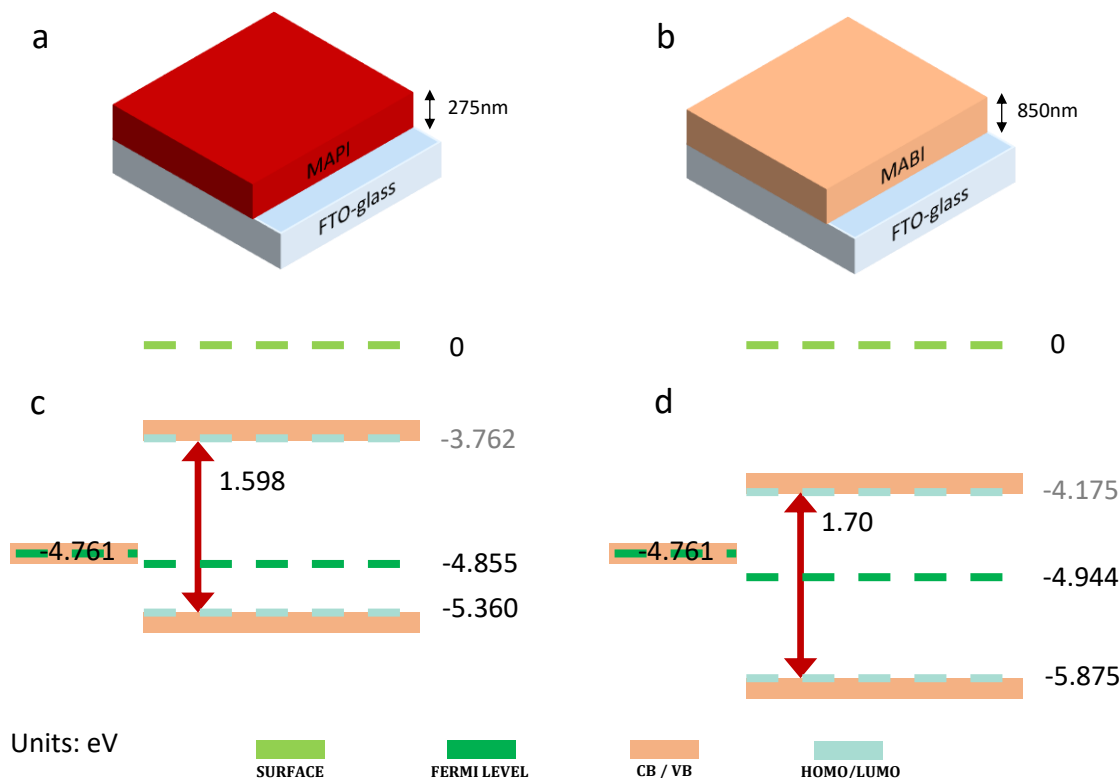

*Figure 32 – **a** MAPI, **b** MABI are architectures of the samples with perovskite thickness measured by the profilometer. **c** MAPI, **d** MABI are band diagrams for each sample with energy level values obtained from different Kelvin probe measurements techniques.*

The fermi level is obtained from a simple CPD measurement in the dark. The fermi levels measured are only 0.1eV different, but where they lie relative to the band edges is more different. The fermi level of MAPI is located below mid-gap (weak p-type doping), whilst for MABI it is above and much closer to mid-gap (very weak n-type doping). The band diagram for MAPI compares well with most values from previous work [75][95][103].

On the left side of each band diagram is the measurement of plain FTO. This is important because contact between the materials means that the fermi levels will equalise at the interface [104]. Since FTO is the grounded layer, it cannot change potential and the fermi level of the perovskite becomes locked to it. Differences in the work function only make sense when the bands are drawn with different surface potentials like in Figure 33.
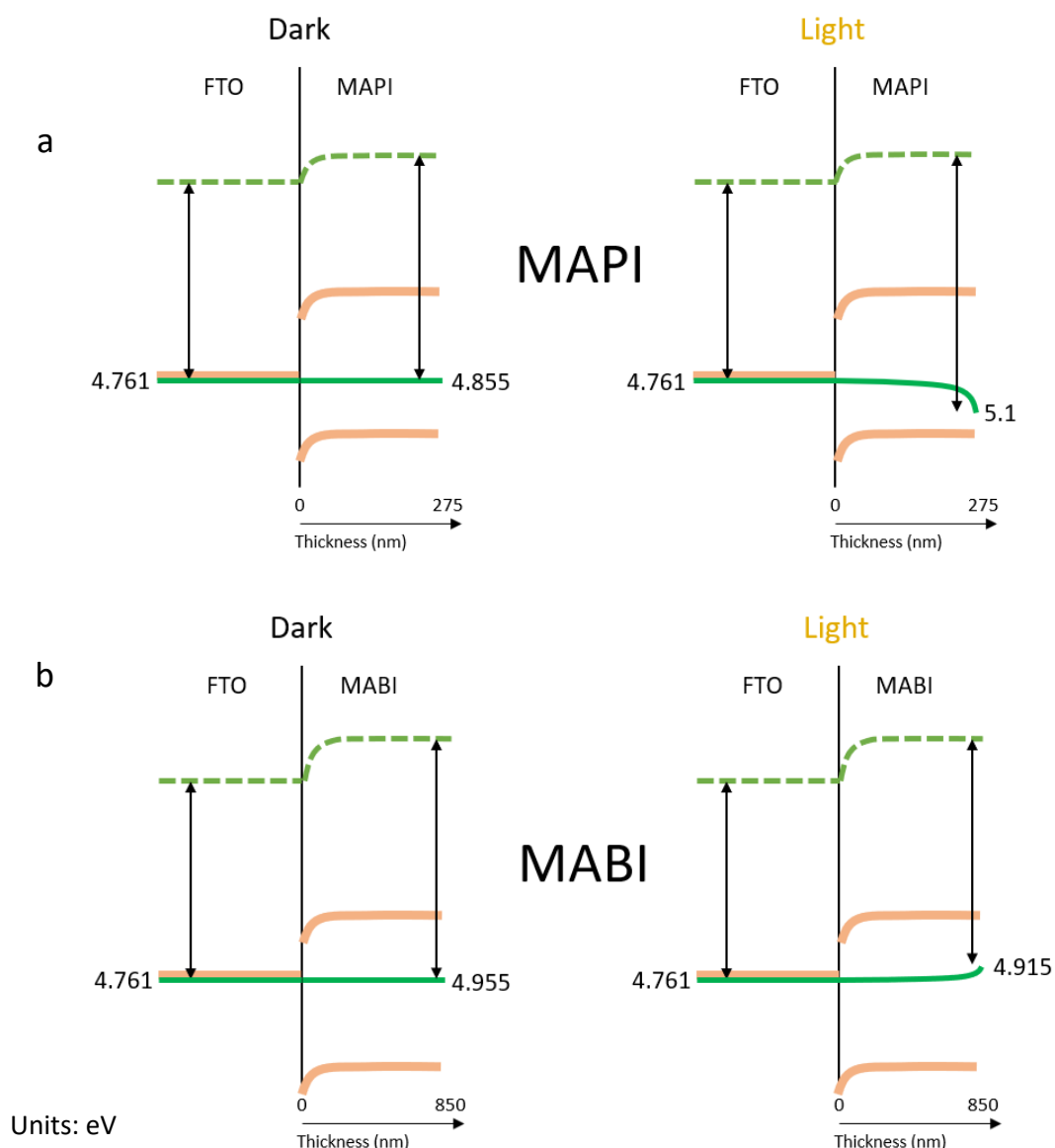
*Figure 33 – **a** MAPI, **b** MABI band diagrams with detail on band bending as a function of thickness. The diagram in light models the band bending to explain the measured response. Values for perovskite WF in light are extracted from Section 4.8 Table 15.*

Figure 33 includes band diagrams which show how band bending might be occurring across the thickness of the sample and the photo-induced changes that occur under white light illumination. Fermi level shifting due to illumination happens because of charges at any of three locations within the sample: the surface of the perovskite; the perovskite bulk; or the FTO-perovskite interface. Our model proposes that the photovoltage detected for MAPI is a surface effect, showing the fermi level of the atoms on the surface changing due to the net movement of charge carriers generated. It is proposed that absorption of band gap photons takes place mostly in the top layers of atoms. For this reason, the fermi level bends more at maximum thickness (Figure 33). In the model, illumination results in the fermi level showing no change at the interface, small change through the bulk and large change at the surface. For MABI, it is proposed that there is a combination of a similar surface effect and an additional interface effect, resulting in a slight decrease in work function. The interface effect could explain the complex and sporadic behaviour of the MABI light response as explored further from Section 4.6 onwards in this chapter.

It is important to note that our manufacturing procedure led to different thickness for the two perovskites. This was not intended and in future work the procedure for MABI will need to be optimised to achieve 500nm thickness.

It is understood that the surface can adopt any charge (being uncapped) due to surface dipoles, or movement of ions and free charge. Since the light induced change in work function for MABI is relatively small, it is reasonable that these other effects could interfere with what we interpret as the light response. Other work in literature has explored modulation doping as a model for the band changes under illumination [95].

The LUMO energy level has been included on Figure 32 for reference. However, it is important to note that this is simply a value calculated by subtracting the bandgap from the HOMO level – it is not measured directly.

4.4 Dark CPD scan – to estimate fermi level

A dark CPD scan was completed to determine an average fermi level value for two samples of each perovskite (Table 12). This also highlighted any locations to avoid when using the Kelvin probe in static mode. Regions where the work function shifts significantly down are indicative of surface defects at the edge of the sample where the film coverage may be poorer, or greater roughness at the edge of the glass substrate. Before each scan, the CPD was checked to ensure the sample had reached equilibrium in the dark conditions.

The results for the two MAPI cells and two MABI cells are summarised in Figure 34 showing the average work function for each scan.

MAPI

Average WF (eV)= 4.894 ±0.007
Average Gradient (AU) = 301 ±6
Age (days) = 4

Average WF (eV)= 4.815 ±0.011
Average Gradient (AU) = 300 ±7
Age (days) = 6

MABI

Average WF (eV)= 4.942 ±0.017
Average Gradient (AU) = 300 ±8
Age (days) = 5

Average WF (eV)= 4.946 ±0.018
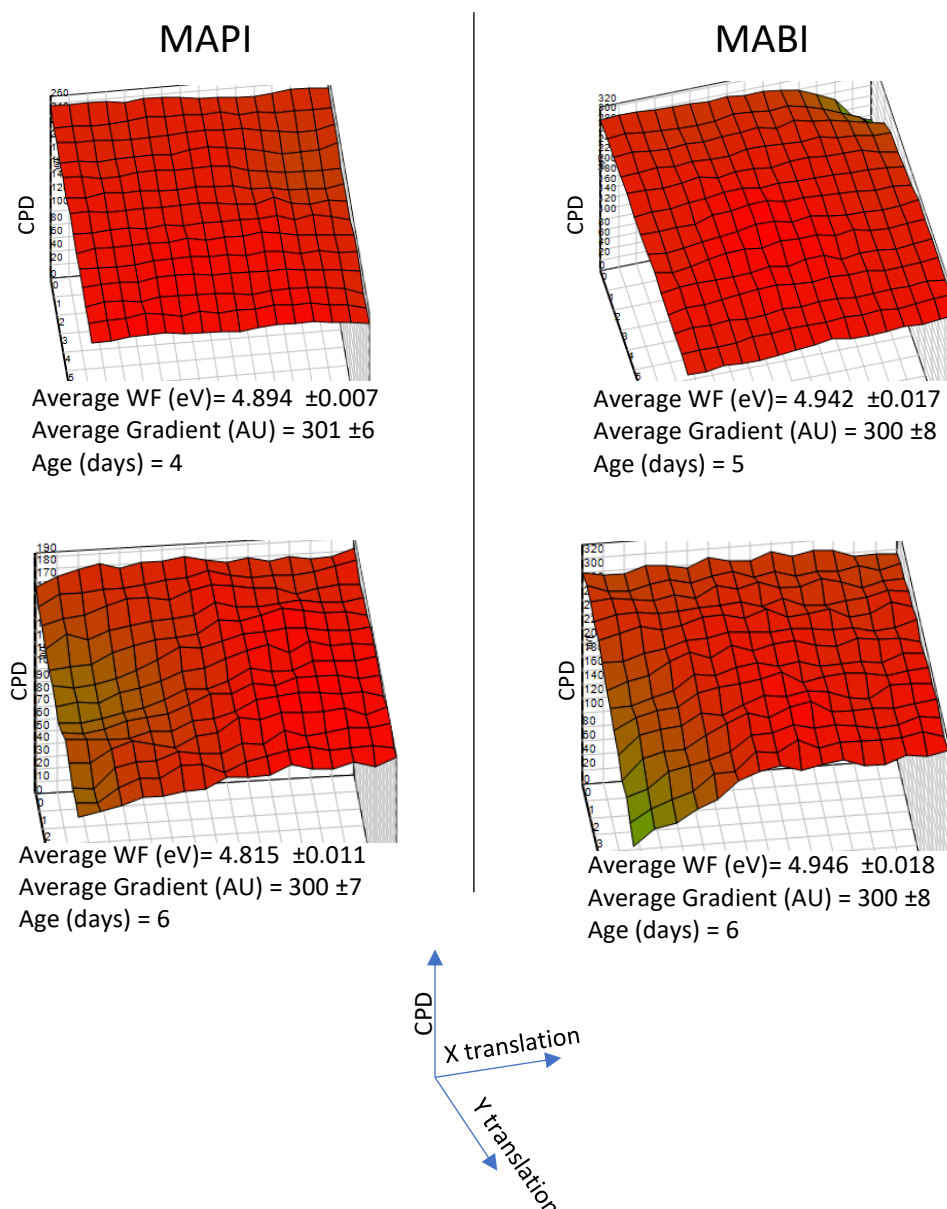Average Gradient (AU) = 300 ±8
Age (days) = 6

*Figure 34 – Scanning Kelvin probe measurement of 15x15mm samples producing 3D plots for CPD measured in dark conditions. Each node on the square mesh represents a data point separated by 1mm increments in X and Y directions. **a** MAPI **b** MABI.*

For conversions of CPD to work function, the tip work function was **4.637 eV**. A silver reference sample had its work function calculated with the APS technique in order to calibrate the tip. Therefore:

$$WF_{tip} = WF_{silver} - CPD = 4.477 - (+0.160) = 4.637 \ eV$$

$$WF_{sample} = WF_{tip} + CPD = 4.637 + CPD$$

The largest range of work function for any of the four samples is 0.018eV over the 15x15mm area – this confirms all samples have a uniform spread of work function. The difference of average work function between the MAPI samples is 0.08eV, whilst for the MABI samples it is 0.004eV. MAPI samples may have more variation from one sample to another because of the anti-solvent release step in the manufacturing procedure. The regions on MABI, where the plot dips, are areas where the glass or FTO might have sustained defects from the cutting process.

The Gradient signal is extremely sensitive to the spacing between probe tip and sample. The maximum variation of ±8 AU in Gradient is very small, and it shows the samples being tested have uniform morphology. During a single-point measurement it is common to record a Gradient variation of up to ±5 AU.

The dark work function degrades with a negative gradient as the sample ages (Chapter 3). Testing has shown the rate of degradation is less than -0.2eV/week (Figure 29).

Table 12 - Average work function values from dark CPD scans on MAPI and MABI.

	Dark work function (eV)	
	MAPI	MABI
Sample A	4.894	4.942
Sample B	4.815	4.946
Average	**4.855**	**4.944**

4.5 Ambient Pressure Photoemission Spectroscopy (APS) – to estimate HOMO level

The APS technique is used to estimate the HOMO level for the band diagrams. The APS04 can extract the photoemission threshold to a resolution of 30-50 meV [104]. It is understood that the photoemission threshold for MAPI and MABI corresponds to HOMO level because they are semiconductors. The tip potential was given +10V bias so that photoemitted electrons from the sample would be attracted to the tip. The sample illumination comes from a deuterium source generating ultraviolet light which is filtered through a grating monochromator to produce incident photons of energy approximately between 4.4eV and 7.0eV.
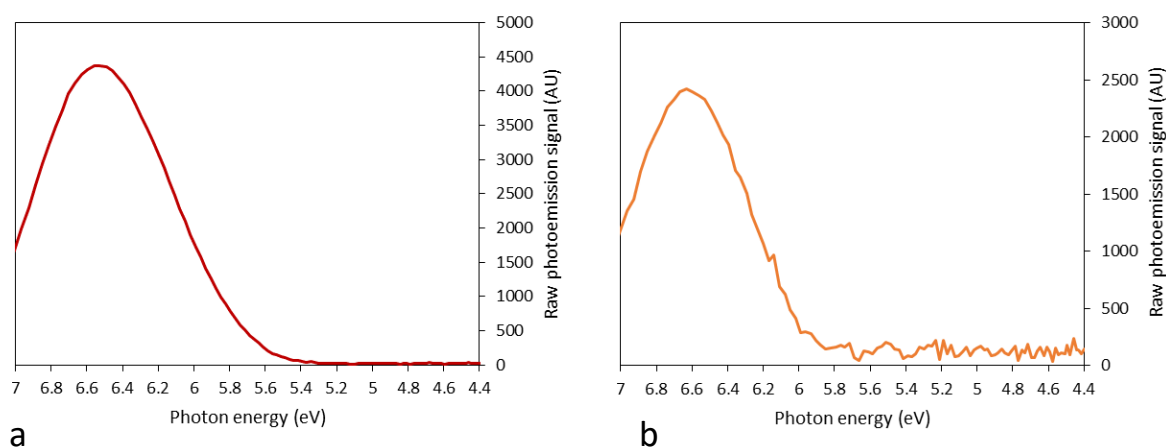

*Figure 35 - APS raw photoemission data against photon energy. **a** MAPI photoemission obtained with a gain of 5 (AU), **b** MABI photoemission obtained with a gain of 8 (AU).*

The photoemission signal (Figure 35) is generated when electrons are emitted under spectroscopic UV radiation from the sample surface and collide with molecules in air. This creates ions which are attracted to a positively charged tip. The current from the photoemission signal increases in proportion with *(photon energy - work function)^n,* where *n=2* for conductors and *n=3* for semiconductors after the photoemission threshold is surpassed [104]. Therefore, a linear relationship is visible on a graph when the photoemission current is cube-rooted (Figure 36).

Both perovskites have performed well as photoemitters showing minimal tail states on Figure 36. Thus, the HOMO estimates made are not influenced by any rogue energy states existing within bandgap. The linear regions for both perovskites on Figure 36 show a great fit with R^2 values close to 1. The linearity demonstrates that both perovskites obey Fowler theory. The HOMO level estimate is obtained by extrapolating the linear section of the photoemission current cubic root plot to the normalized photoemission baseline (Figure 36) [104]. The repeat measurements for each perovskite returned a good match (see Appendix A Figure 66 for these additional plots).
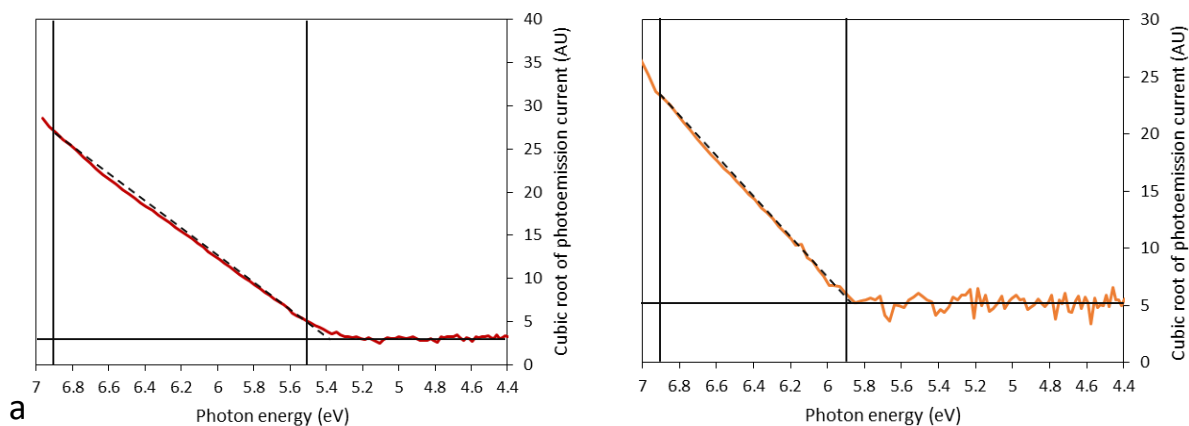
Figure 36 - APS cubic root plot to highlight linear region which extrapolates to a normalised zero photoemission baseline for estimate of HOMO level. **a** *MAPI plot has an R^2 value of 0.9991 and the measurement used a gain of 5 (AU) and resulted in a photoelectric yield of 15.6 (AU),* **b** *MABI plot has an R^2 value of 0.9985 and the measurement used a gain of 8 (AU) and resulted in a photoelectric yield of 17.5 (AU).*

The gain was considerably lower for MAPI, demonstrating that MAPI is a much stronger photoemitter (Figure 36). The HOMO level estimates listed in Table 13 show that the data is highly repeatable for both perovskites using this measurement technique.

Table 13 - HOMO level estimates obtained from APS measurements for each sample. These are averaged for the HOMO levels shown on the band diagrams in Section 4.3.

Sample	HOMO Level (eV)
MAPI Sample A	5.38
MAPI Sample B	5.34
MABI Sample A	5.88
MABI Sample B	5.87

4.6 Surface photovoltage spectroscopy (SPS) – to estimate bandgap

The SPS measurements consisted of illuminating the samples with light through a monochromator for wavelengths 1000nm to 400nm in 5nm steps at maximum light intensity (5000 AU). The main output of the surface photovoltage spectroscopy is a bandgap estimation. The measurement captures an onset of photovoltage as the bandgap is reached. The bandgap is derived by interpolating the wavelength axis at the mid-point of the linear transition. The plots and the associated bandgaps are shown in Figure 37.
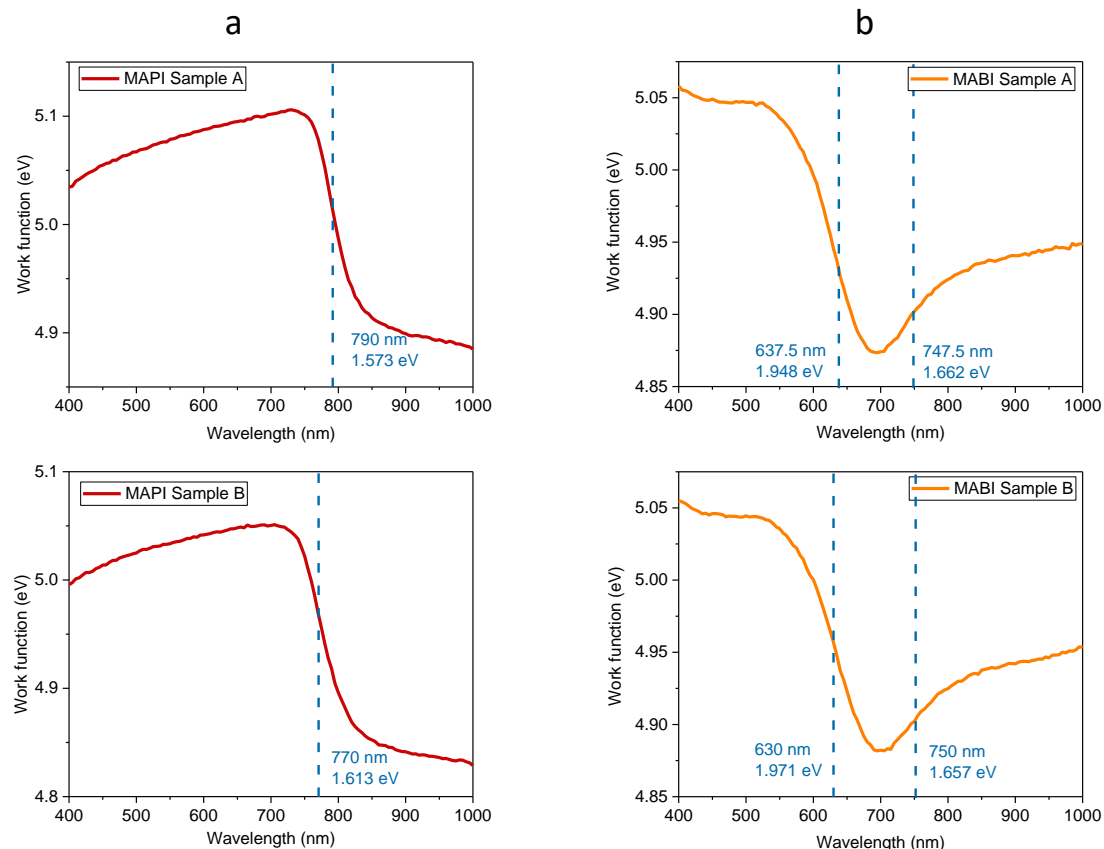

*Figure 37 - SPS plots with bandgap interpolation detailing the bandgap wavelength. MABI measurement shows two possible locations that could indicate bandgap, **a** MAPI, **b** MABI.*

An average bandgap of 1.598eV was measured for MAPI - this is in agreement with literature (1.51 [110], 1.55 [36], [111], 1.59 [85]). The plot for MABI was complex and did not show a clear bandgap transition. The bandgap of 1.70eV (shown in the band diagram) was ultimately estimated from UV-visible spectroscopy as an alternative method. Bandgap values for MABI found in literature are 1.78eV [106], 2.04eV [88], 2.24eV [89] and 2.9eV [91]. The work function at 1000nm matches the dark work function values reported in Section 4.4 for all the plots in Figure 37. This shows the dark equilibrium was reached before the measurement.

The MAPI plots show a linear increase in work function around 800nm, associated with bandgap photons. The only unexpected feature of the MAPI plot is the decline in surface photovoltage from 700nm to 400nm. This is most likely due to there being less photons in the light source at higher energies. The MABI bandgap is harder to estimate from the SPS plot because there are two visible

transitions in the surface photovoltage. This is abnormal behaviour compared to the MAPI SPS plot where there is a single surface photovoltage transition initiated by the bandgap wavelength being reached.

The mid-points of each transition on the MABI plot suggest two different bandgaps of 1.66eV and 1.96eV. Without being able to distinguish the bandgap with certainty, UV-visible absorption spectroscopy was used as an alternative way of estimating the bandgap. The UV-visible absorption spectrum measured on a similar MABI film leads to a bandgap estimate of 1.70eV (Figure 38b). This is a lower energy bandgap than the range of 1.78 [106] to 2.04 [88] found in literature, but is in rough agreement with the lower energy transition on the SPS plots. The MAPI UV-visible absorption spectrum yields a bandgap that is very close to the SPS value of 1.598eV. The difference between the bandgaps of the two perovskites is only around 0.1eV.

The MABI bandgaps in literature have a wide range because the value is particularly sensitive to how the samples are prepared, and fabrication methods are not always consistent between literature sources [41]. Furthermore, the MABI perovskites reported exist in different stoichiometric ratios (e.g. $MA_3Bi_3I_{10}$, $MA_3Bi_2I_9$).

The UV-visible spectrum for MABI shows two onsets (Figure 38b), not just one as in the case of MAPI. This UV-visible absorption profile is consistent for MABI within literature [88][112][61][89]. The first increase in absorbance relates to the bandgap and the second increase around 590nm corresponds to a higher energy split density of states within the conduction band [88]. See Appendix A Figure 67 for repeat measurements of UV-visible data.
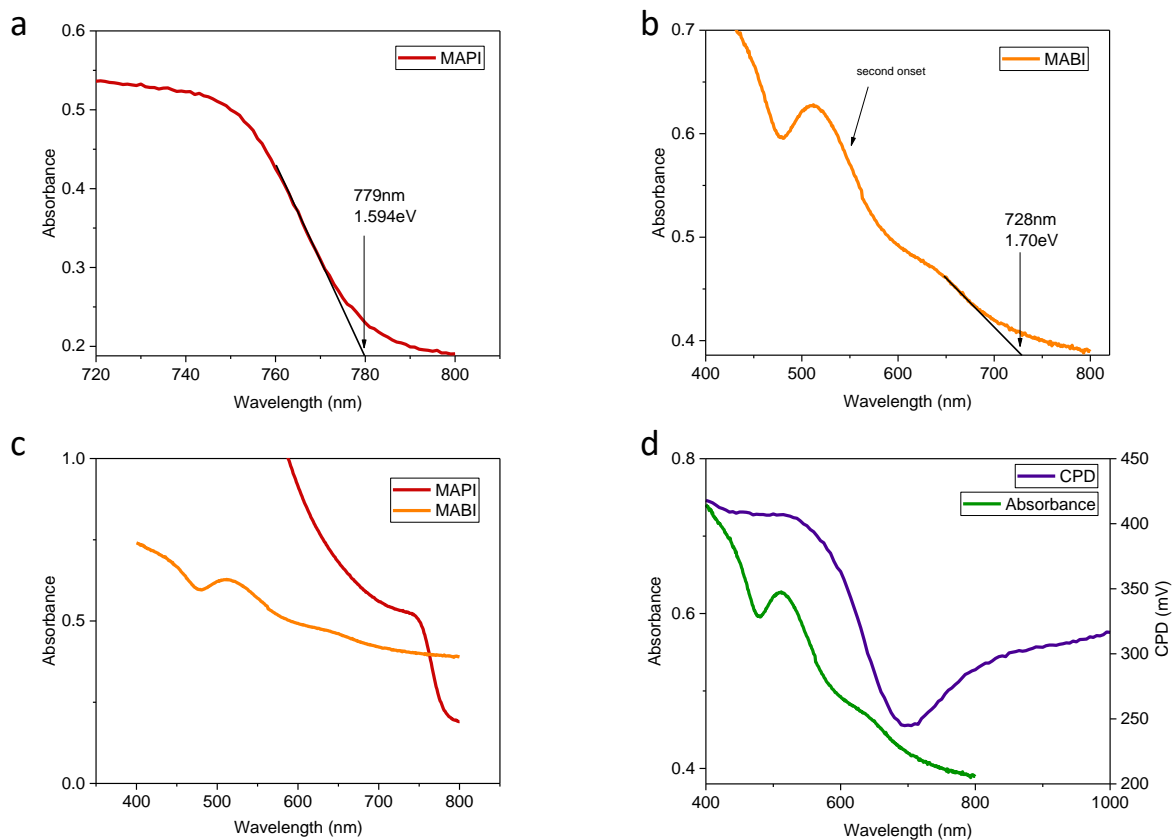

*Figure 38 - UV-visible spectroscopy measurement with bandgap linear extrapolation of **a** MAPI, **b** MABI. Each plot is an average from three samples. **c** UV-visible absorbance for MAPI and MABI on the same axis, **d** MABI SPS and UV-visible data on same wavelength axis. This highlights circa 700nm and 500nm absorption effects.*

Layering the dark work function on the MABI plot highlights how the fermi level shifts in different directions across the spectrum (Figure 39).
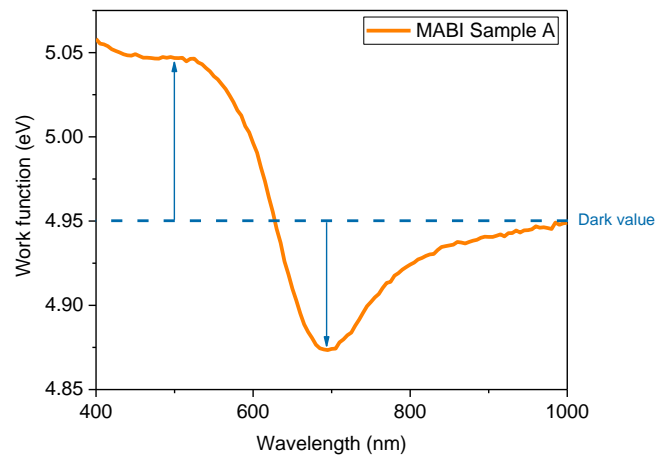

Figure 39 - MABI SPS showing work function shifting up and down relative to dark value.

It is proposed that an ionic effect is responsible for the region where work function increases relative to the dark value. Ions absorbed from the atmosphere, or left surplus in the perovskite composition, could drift within the material due to the electric field generated under illumination.

Ions of atmospheric gases like oxygen can be absorbed at the surface because the perovskite can have a porous surface. The vacuum testing in Chapter 5 suggests oxygen is sucked from the perovskite surface under vacuum. A fermi level response to an ionic effect would likely be a slow effect. This is challenged in Section 4.8 by the result shown for a single pulse of 500nm light (Figure 44a) – the response is fast and occurs within 5 seconds.

Another source of ions is surplus bismuth and iodide left unreacted from the perovskite composition. Bismuth may be present within the perovskite layer in two oxidation states: Bi^0 and Bi^{3+} [41]. Traces of BiI_3 are shown unreacted in the XRD plot (Appendix A Figure 64). The bandgap values for BiI_3 in literature are 1.67 [113], 1.96 [113] and 1.8 [41] [114].

This idea of ionic charge drifting in the electric field across the perovskite thickness does not explain where the 500nm light is being absorbed. The UV-visible data provides strong evidence suggesting that absorption occurs at lower wavelengths because of a split density of states within the conduction band [88]. In other literature, the 500nm peak on UV-visible data is referred to as an excitonic peak, and trivalent Bi^{3+} within $(Bi_2I_9)^{3-}$ bi-octahedrons is suspected to be the composition that absorbs the 500nm light and excites an electron [89]. More research is required to make a concrete conclusion on what effects are causing the result in Figure 39. The model proposed here is an ionic charge diffusion to/from the FTO-MABI interface, initiated by a second absorption from higher energy density states.

4.7 Surface photovoltage (SPV)

The surface photovoltage measurement provides a plot of work function against intensity of light. This is useful for highlighting the intensity required for maximum charge generation.
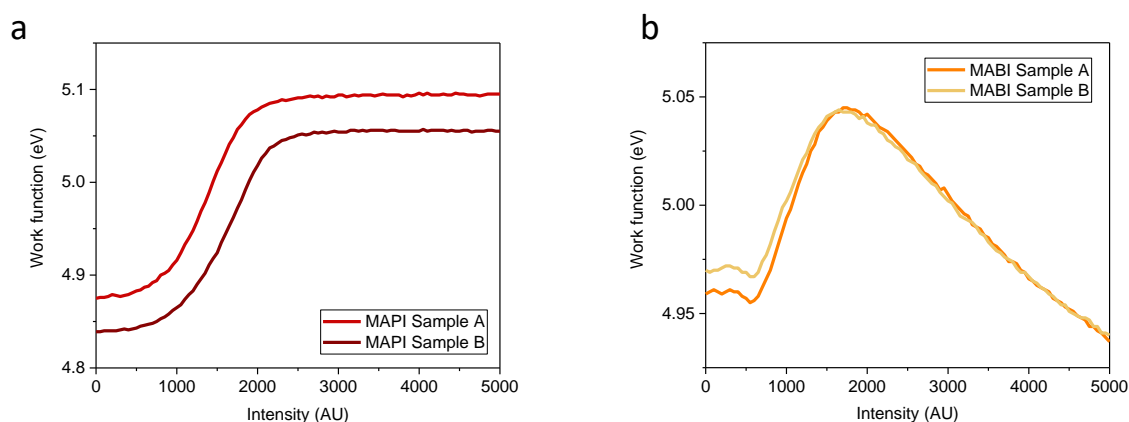

*Figure 40 - SPV plots showing work function change with increasing intensity of white light, **a** MAPI, **b** MABI. CPD converted to work function using tip work function of 4.637 eV.*

The Kelvin probe software displays intensity in arbitrary units (AU). A rough conversion to lux units can be made using Table 14. Both perovskites reach their maximum surface photovoltage well before 5000 AU intensity – highlighting good ability to harness energy at lower intensity levels (Figure 40). The result for MAPI shows an ideal characteristic where the work function plateaus at a maximum. This means the fermi level has an energy limit which it reaches at low intensity.

The MAPI SPV increases steeply until 3000 AU and the MABI increases steeply until 1500 AU. Surprisingly, the MABI photovoltage decreases after reaching the maximum around 1800 AU. This result may help explain why the MABI light response in Figure 43b pulses up at the start and end; the intensity of light for the response is 5000 AU and the light source increases from 0 to 5000 AU in a short space of time. Within this time the response could understandably have a sharp pulse as seen in Figure 43b.

The straight-line increase of work function with intensity shows the material has ideal photovoltaic behaviour. For MABI there is also a straight line decrease which is representative of a second effect. To see the SPV plotted on a logarithmic scale see Appendix A Figure 68 - the linear regions are more distinct.

Conversion of arbitrary units (for white light conditions only):

Table 14 - Measured intensities of white light with a luxmeter for the arbitrary units scale.

Intensity										
AU	0	500	1000	1500	2000	2500	3000	3500	4000	4500	5000
Lux	0.3	2	95	600	1920	4400	8100	13400	20500	29400	40400

When carrying out SPV measurements, there is a risk that a trend captured in the data is unintentionally related to time instead of intensity. This is because the measurement takes considerable time to step through the intensity scale. Diffusion of ions is time-dependant, therefore, SPV measurements were carried out at different speeds to see if the peaks shifted. Figure 13 shows that both perovskites show a slight trend of slower scans resulting in the peak work function reached at lower intensity. The results in Figure 41 show there is a correlation with time, but it is not substantial enough to mask the relationship with intensity.
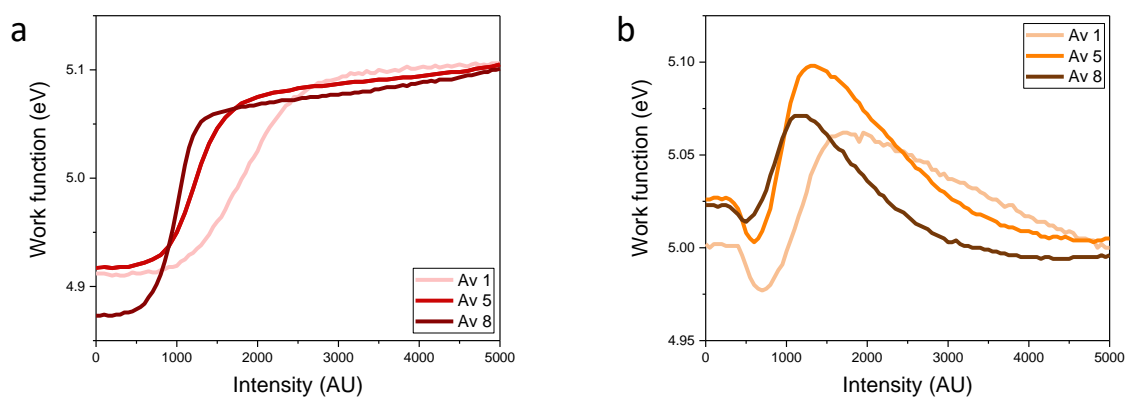
*Figure 41 – White light SPV measurements completed at different scan speeds show that the SPV relationship with intensity is true and not a disguised relationship with time. Av1 =150 seconds, Av5=675 seconds, and Av8=1110 seconds for both perovskites. **a** MAPI **b** MABI*

Above measurements are all with white light illumination – therefore, it includes all the wavelengths in the SPS plots combined. This is important to consider when interpreting the MABI SPV plot because the MABI experiences positive and negative responses depending on wavelength as was concluded in Section 4.6. It is strange that the white light SPV decreases at higher intensities, but perhaps the wavelength that induces a negative response becomes more absorbed. To explore this further, two additional SPV measurements were completed with monochromatic light at 500nm and 700nm (Figure 42). These are the wavelengths MABI responds to the most, as highlighted by SPS (Figure 39).
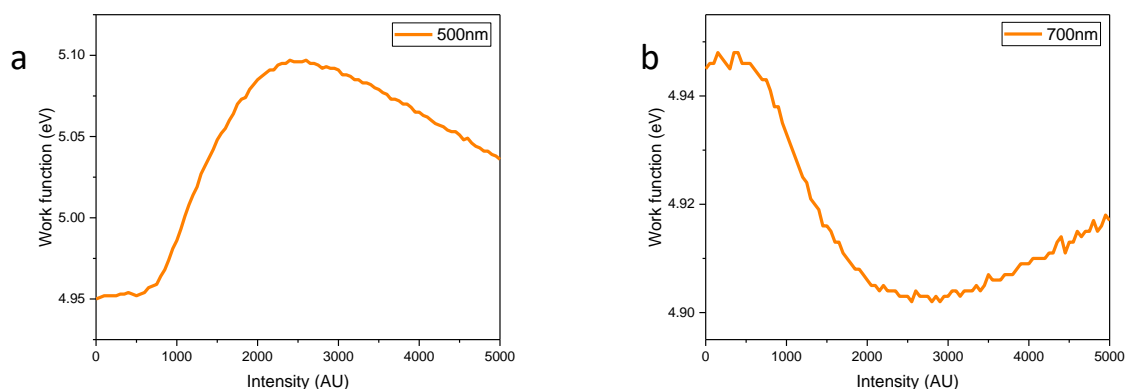

*Figure 42 - MABI monochromatic SPV for **a** 500nm light and **b** 700nm light. There is completely opposite direction of response due to different processes occurring at each wavelength.*

Both 500nm and 700nm measurements begin around 4.95eV. This shows that both measurements were in dark equilibrium at zero intensity. The response measured for 500nm is larger than for 700nm; around +150meV and -40meV respectively. Therefore, the 500nm SPV matches better in terms of shape with the white light plot (Figure 40b), as it has a larger voltage contribution. It makes sense to regard the 700nm effect as bandgap absorption because the UV-visible data suggests a bandgap at around 700nm wavelength. Therefore, the -40meV decrease is the bandgap response and it is good that there is visible absorption from low intensity.

The MABI 700nm plot does not flatten after the peak SPV is reached, instead it increases by 10meV. The band diagram in Section 4.3 shows that MABI is very weakly n-doped (Figure 32) - the fermi level is 30meV above mid gap. It is plausible that the increase mentioned is indicative of the fermi level drifting to mid-gap – an effect that can occur when the light intensity exceeds the natural doping level in the material.

The 500nm data is under further investigation as there is uncertainty over what process is causing the fermi level to respond, as explored in Section 4.6. The model proposed is an ionic charge diffusion to/from the FTO-MABI interface that is initiated by a second absorption from higher energy density states.

4.8 Light response pulses

This section of measurements focuses on the immediate change in CPD of the two perovskites under illumination.

Table 15 - Summary table displaying responses measured, compared to those found in literature for FTO-perovskite and full cell architectures.

Perovskite	CPD response to light (mV)			
	Measured	Literature		
	FTO/Perovskite		Full cell Architecture	
MAPI	250	200 [75][95]	1000	[75]
MABI	40	None found	500 [105]	[112]

A typical full cell (Figure 17a) with MAPI sandwiched between transport layers yields a light response of around 1000mV [75]. When analysing the light response of uncapped perovskite layers, it is important not to look in detail at insignificant photovoltage changes. This work shows a CPD change of around 250mV for MAPI (Table 15, Figure 43a), which would be a significant fraction of the full cell response. The response for MABI has poorer repeatability and is mainly <40mV (Table 15, Figure 43b). In the context of a typical 500mV V_{oc} of a full MABI cell [41], the CPD change might be considered as insignificant towards the performance of a device because it is small in context. Being a smaller response, it suggests that the charge mobility is poorer in MABI.
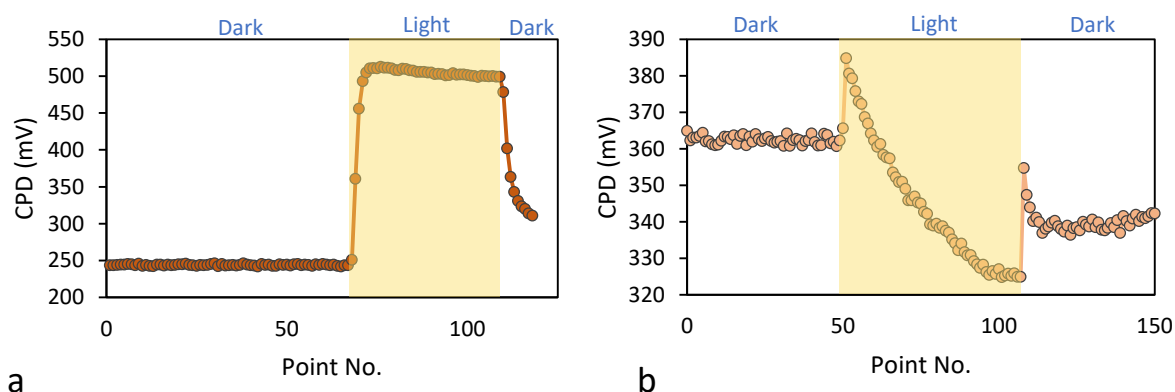

*Figure 43 – MAPI CPD measurement during single light pulse. **a** MAPI shows an efficient charge generation and decay in response to light, **b** MABI shows unclear charge generation and both positive and negative fermi level changes under illumination.*

A semiconductor's work function light response normally involves two functions:

(1) A fast response caused by excited electrons reaching the conduction band.

(2) A slower response caused by slow ionic effects.

After the light is switched off, the work function slowly returns to its original value with an exponential decay. This idea is easy to see in a MAPI response (Figure 43a) but slightly more complicated for the MABI response (Figure 43b). The MAPI response closely matches the result from Amalathas et al [95], but is opposite in direction to the responses reported by Harwell et al [75]. Harwell et al used an architecture of FTO/TiO$_2$/MAPI which explains why the responses switches direction. The TiO$_2$ is an

electron transport layer so it attracts electrons away from the Kelvin probe, whereas FTO is an electron-rich n-type semiconductor so repels the electrons towards the Kelvin probe.

The shape of the MABI response is completely different to MAPI. The sharp jumps at either end of the light region for MABI are likely excitonic effects because they occur in an extremely short space of time. Ignoring these excitonic effects leaves a response of around -40mV.

It is understood that the perovskite surface (being uncapped – not sandwiched between transport layers) can adopt any charge due to surface dipoles, or movement of ions and free charge. Since the light response for MABI is small, it is possible that these other effects could interfere with what we interpret as the light response. Alternatively, the small response may be due to the product of the 500nm effect opposing the 700nm effect. The SPS measurement established that MABI responds positively and negatively at different wavelengths within white light bandwidth. Therefore, the response captured in Figure 43b would be a combination of the responses because it is under white light illumination.
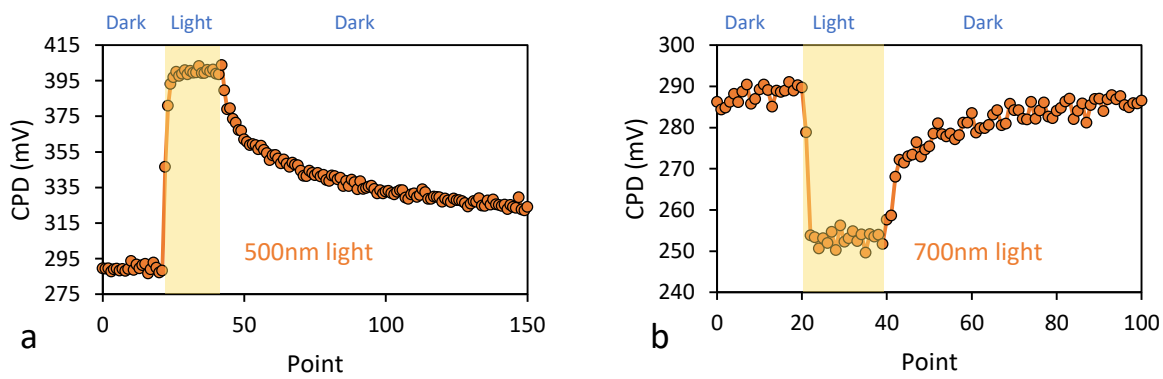

*Figure 44 – CPD responses of MABI to monochromatic light: **a** 500nm light showing large rise in CPD of over 100mV, **b** 700nm light showing decrease of less than 40mV.*

Individual responses to monochromatic light of 500nm and 700nm are shown in Figure 44. The initial response is followed by a relatively stable plateau and then a decay when the light is switched off – similar characteristics to MAPI. The white light response is 40mV, whereas under 500nm light the response soars to over 100mV. Ideas of why the fermi level shifts in different directions have been explored in Section 4.6. It is suggested that the 700nm effect is bandgap absorption, and the 500nm effect is likely an ionic charge diffusion to/from the FTO-MABI interface initiated by photon absorption from higher energy density states.

The 500nm light pulse is incredibly fast. This shows MABI could be used outside of solar PV, for applications involving detection of light around 500nm. Next, a measurement was carried out in 500nm light at an intensity of 2500 AU to test whether MABI could perform better under certain light conditions (Figure 45). The intensity was set at 2500 AU because Figure 42a highlighted 2500 AU was the optimal intensity. The test was successful. MABI shows much faster generation of charge under illumination and a higher surface photovoltage suggesting the V_{oc} would be higher for a MABI cell in these light conditions than for a MAPI cell. The decay is slower for MABI. Improvements to the MABI perovskite quality could reduce the decay time in future measurements.
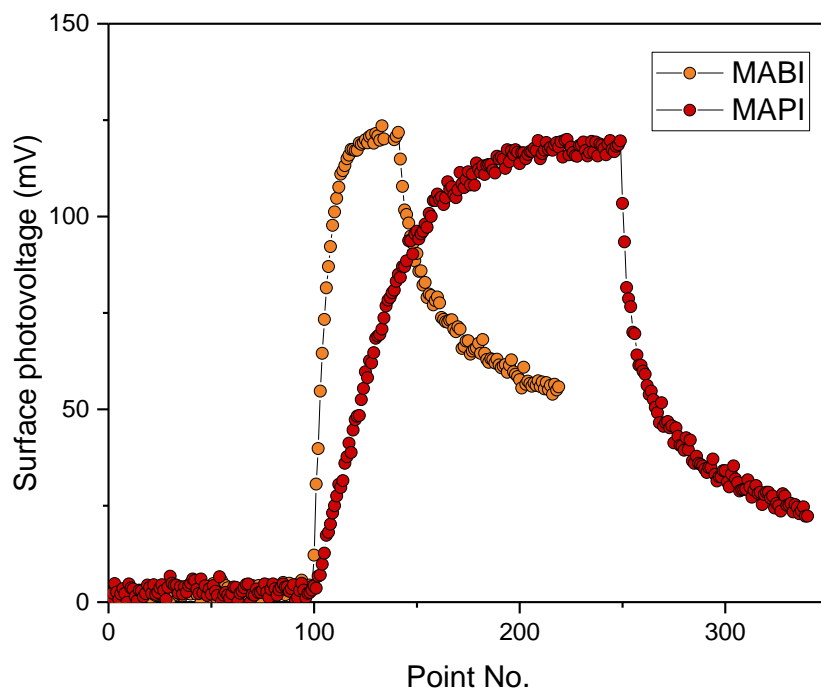
Figure 45 – Responses of MAPI and MABI to 500nm monochromatic light at intensity 2500 AU showing that MABI has a larger light response in these conditions.

4.9 Light pulse cycling

To learn more about the sample performance over its lifetime, 100 cycles of white light pulses are measured over around 2 hours. This is done to capture the fast response alone, with a visual indication of how it changes with the extending number of light pulses. Work function plots are displayed in Figure 46. Each pulse contains 20 points under illumination and 40 points in the dark. 20 points is considered enough time for the response to reach above 90% of its magnitude. Differences between the two perovskites are easy to spot from Figure 46. The comparative observations are listed in Table 16.
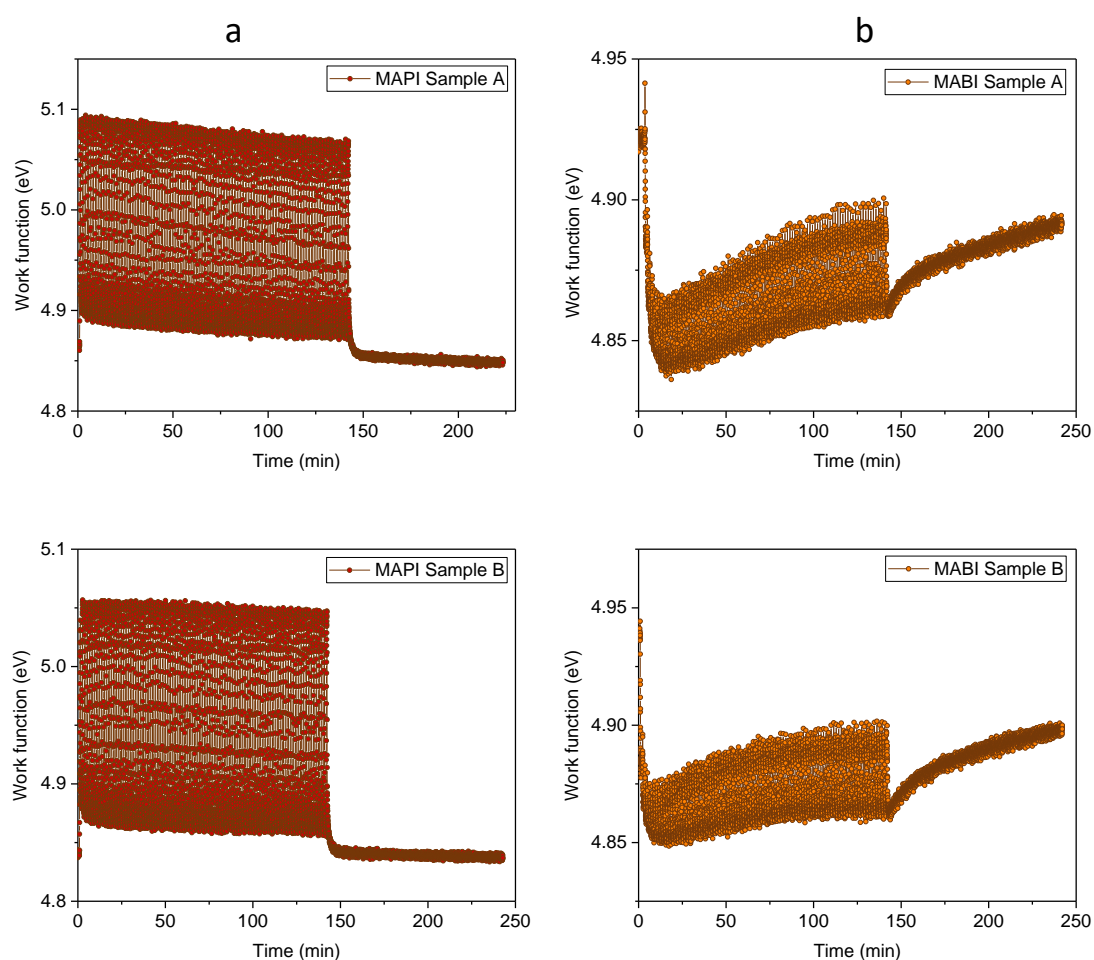
*Figure 46 - Light pulse cycling of **a** MAPI, **b** MABI. Work function plotted against time for 100 pulses of 20 points under white light illumination and 40 points in dark.*

Table 16 – Differences between MAPI and MABI as observed from light pulse cycling.

Detail	MAPbI$_3$	MABI$_3$
Direction of response	Increase in CPD	Decrease in CPD
Magnitude of response (meV)	≈190	≈37
Time dependant response	No	Yes
Decay	Rapid	Slow

Overall the characteristics for MAPI make it highly favourable over MABI: the magnitude of response is always greater so the V_{oc} of the full cell is greatly improved, the response is reliable because there is negligible change with time and the signal decays fast showing minimal trapping states as the charge carriers recombine. The MABI decay does not reach the original value after about 1 hour of decay. This means either the material could have experienced a phase change from light soaking, or more likely is that the decay requires a much longer time to reach the dark equilibrium. The longer decay of MABI is likely linked to there being far more charge traps present in the MABI as it is known that the quantum efficiency is very low [41]. Figure 47 shows the pulses for each perovskite at higher resolution so that details can be easily analysed.
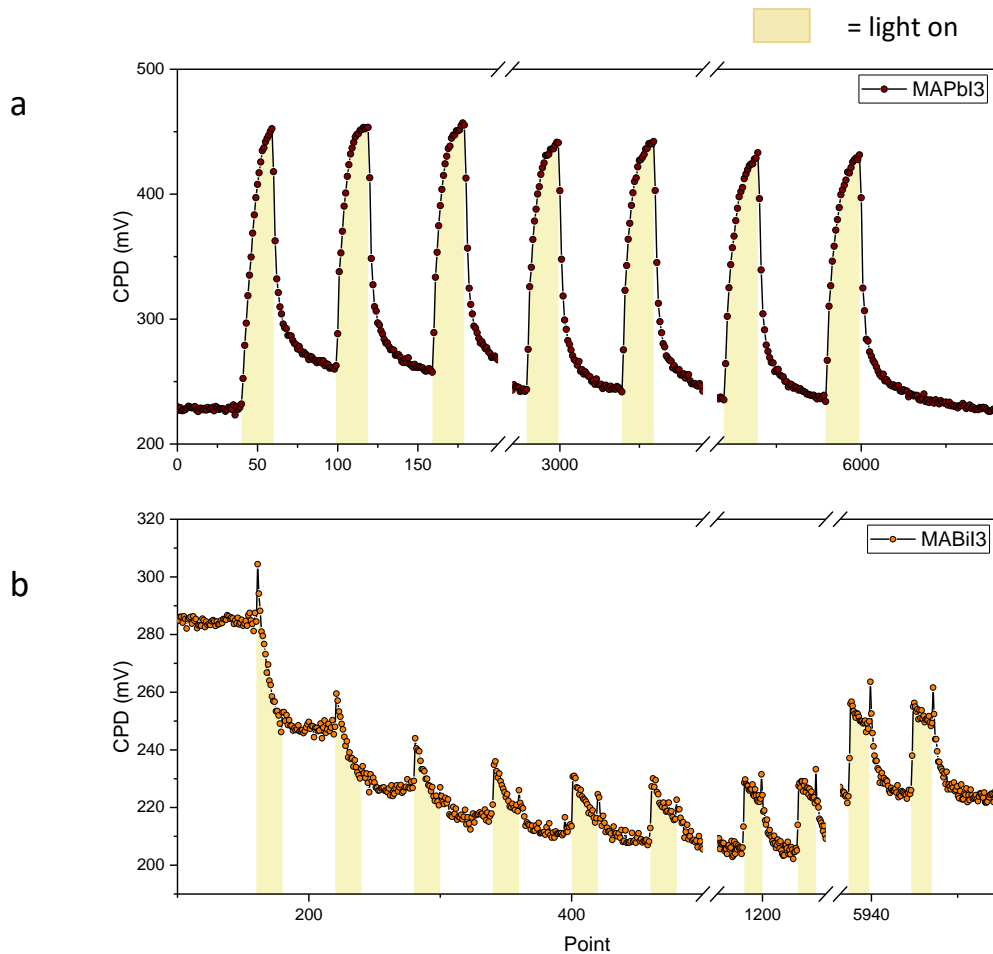

*Figure 47 – Magnified plot of white light responses to show the change across the 100 cycles in detail for **a** MAPI **b** MABI.*

In each pulse the MABI response starts with a sharp excitonic effect in one direction (this is the same as in Figure 43b), followed by the true fermi level change in the other direction. This fermi level change diminishes with number of pulses suggesting MABI has a strong light soaking relationship, and the excitonic effect gradually dominates the response.

Analysing the final decays in more detail on a log scale tells us whether the decay is made up of one or two functions. This is demonstrated with Figure 71 and Figure 72 in Appendix A.

4.10 Surface photovoltage (SPV) after 5months

Samples manufactured for the testing mentioned in the previous sections of this chapter were stored in dark atmospheric conditions and 5 months later the white light SPV was tested again.
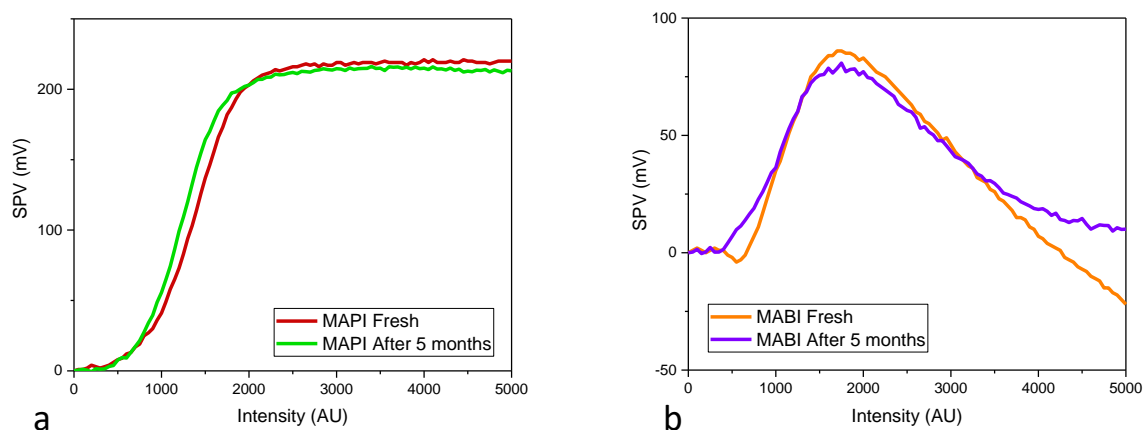

*Figure 48 - White light SPV of after 5 months storage in darkness at atmospheric conditions for **a** MAPI **b** MABI. Work function is converted to SPV for the Y axis by taking the dark work function value as zero.*

Many reports suggest that the stability of MAPI is poor [115][116][117][118]. Figure 48 shows a significant result, because it shows MAPI surface photovoltage is not the source of a decaying efficiency seen in previous stability testing. Both perovskites show here that their SPV is barely affected by ageing over 5 months. The MAPI shows slightly better repeatability in the SPV, and the dark work function value shows less change over the 5 months (Table 17). These samples were separate to those used to test stability in darkness over 7 days (Figure 29) and 60 days (Figure 30).

Table 17 - Dark work function values before and after 5 months atmospheric storage in darkness.

	MAPI	MABI
Before	4.855	4.944
After 5 months	4.805	4.867

Chapter 5. Investigating the effects of vacuuming on the fermi level of MAPI and MABI in darkness and illumination

5.1 Summary

Recently, MAPI degradation has been linked with oxygen doping combined with light [109][108][107]. A mechanism for the oxygen and light-induced degradation is described by Aristidou et al [107]. It is highlighted that an encapsulated oxygen-free environment is desirable for a MAPI solar cell.

This study explores the relationship between work function and oxygen in the environment. Testing is completed on MAPI and MABI perovskite thin films with a Kelvin probe in a vacuum system pumping down from ambient air followed by a nitrogen atmosphere. In the case of both perovskites, a drop in dark work function of over 200mV was seen when pressure was decreased from ambient air, and when the environment was filled with nitrogen the work function did not recover completed to the same value as ambient air. Pumping down the pressure from a nitrogen atmosphere resulted in a smaller drop in work function.

The MAPI and MABI perovskites have work function responses to incident white light as shown in Chapter 4. Here, the light response was measured at atmospheric pressure and low pressure to investigate pressure-induced changes in response. The MAPI white light response became less clear and of smaller magnitude when under vacuum and the MABI did the opposite. The testing was competed at the KP Technology facility in Wick. A summary of the experiment measurements is displayed in Table 18. Note that these results are only preliminary, and no repeat measurements were carried out. These results serve as an indication towards any potential for improved photovoltaic performance under vacuum conditions. In summary, under vacuum conditions the photovoltaic performance of MAPI is not improved, but the photovoltaic performance of MABI is improved.

Table 18 - Summary of UHV KP measurements for MAPI and MABI.

Measurement	*Key Points*
*MAPI **dark** vacuum cycle (from ambient)*	• *CPD drops by 225mV*
*MAPI **dark** vacuum cycle (from N2)*	• *CPD drops by 140mV*
*MABI **dark** vacuum cycle (from ambient)*	• *CPD drops by 220mV*
*MABI **dark** vacuum cycle (from N2)*	• *CPD drops by 180mV*
*MAPI **ambient** light response*	• *At ambient, response was +250mV*
*MAPI **low pressure** light response (from ambient)*	• *At 9.3×10^{-3}mBar, response was -40mV* • *At 6.7×10^{-3}mBar, some clear response of -80mV* • *At 6.4×10^{-3}mBar, some noisy +100mV responses*
*MABI **ambient** light response*	• *At ambient response was -60mV then slightly positive +15mV; it is a complex response to begin with*
*MABI **low pressure** light response (from ambient)*	• *At 1.2×10^{-2}mBar, response was +20mV* • *At 8×10^{-3}mBar, response was same as at ambient* • *At 7.3×10^{-3}mBar, response became +50mV*

For conversions of CPD to work function use a tip work function of **4.412 eV**. This was the work function of the gold UHV Kelvin probe measured in ambient conditions. There is confidence that the work function of the gold tip will be unchanged under vacuum because oxygen in ambient conditions has negligible effect [119].

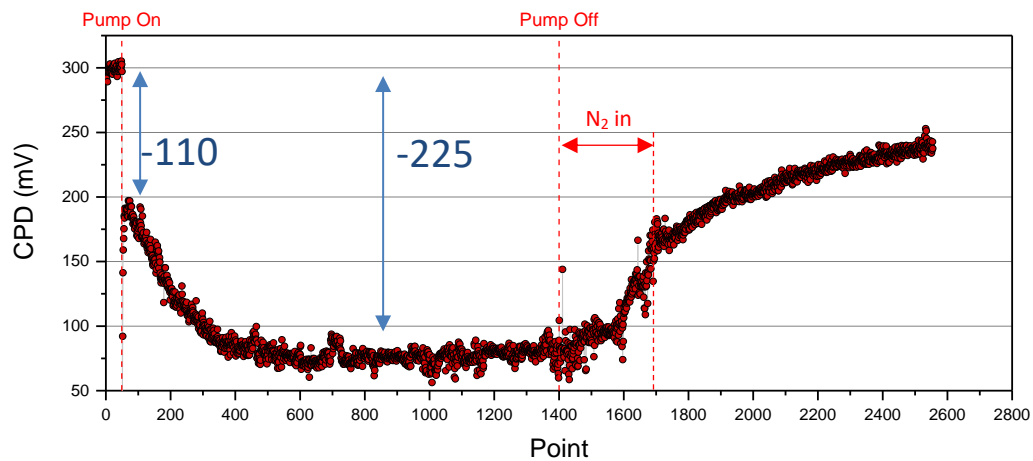## 5.2 Effect of pumping on dark work function

Sample: MAPI

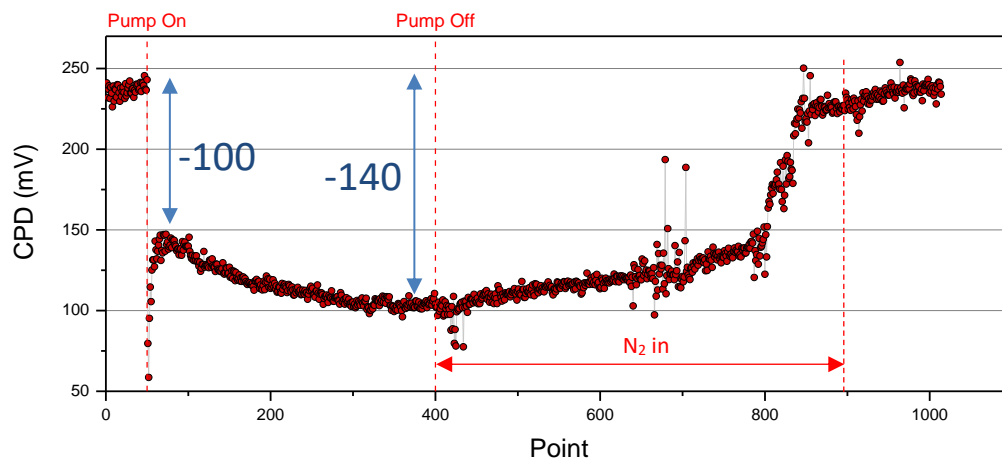*Figure 49 - MAPI dark vacuum cycle from ambient air.*

Figure 50 - MAPI dark vacuum cycle from atmospheric pressure nitrogen.

Pumping down results in an instant drop in CPD for MAPI in ambient and nitrogen conditions. The initial drop in CPD is very similar for both plots, suggesting the initial effect is not dependant on oxygen in the atmosphere. Instead it is most likely due to the initial drop in pressure that occurs instantly when the pump begins to draw. Pumping from an N_2 atmosphere results in a smaller overall change in CPD. The difference between the first and last points on Figure 49 might be an indication of the oxygen having left the surface of MAPI, because the first and last points on Figure 50 for pumping from a nitrogen atmosphere match up. This observation shows there is a difference when lowering the pressure in ambient conditions and lowering the pressure in nitrogen conditions and that it is likely due to the oxygen doping present in ambient conditions, but not present in nitrogen conditions.

Within the data points where N_2 is released back into the vacuum, the rate at which CPD returns to its original value increases mid-way on both Figure 49 and Figure 50. This is simply due to the flow rate of N_2 being manually increased.
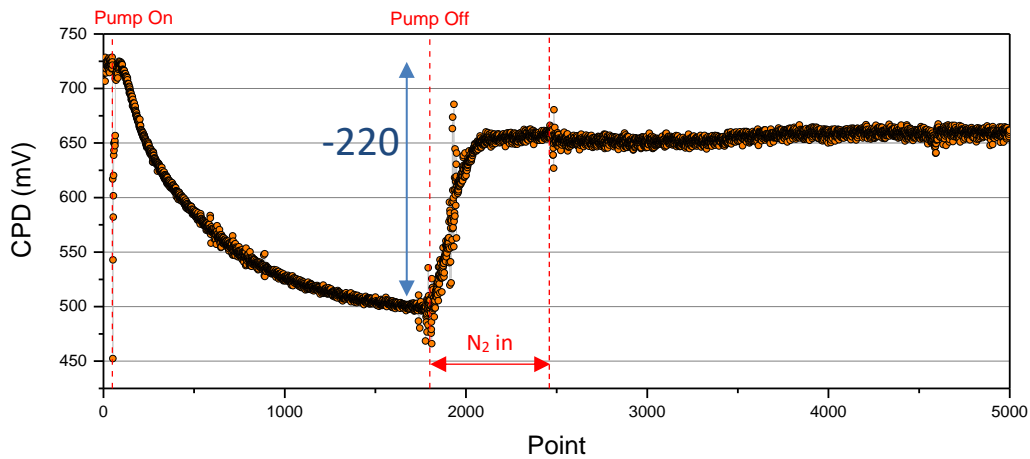
Sample: MABI

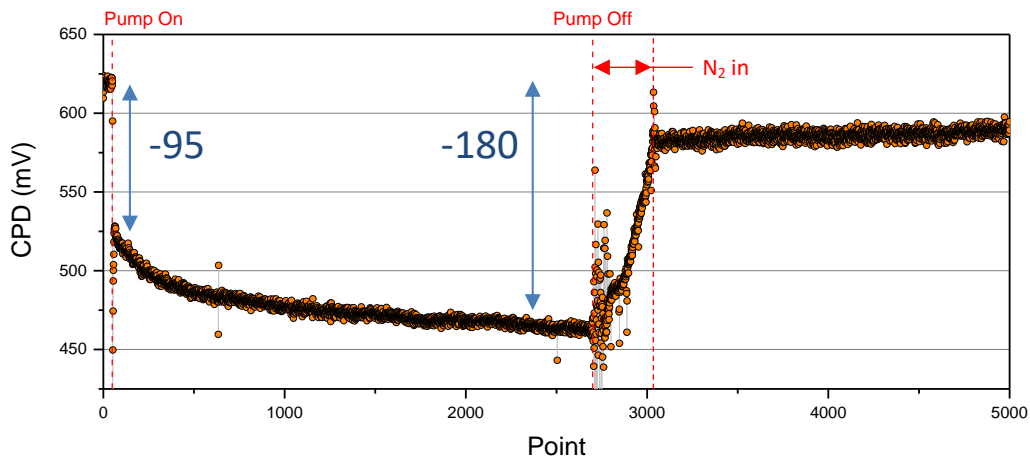*Figure 51 - MABI dark vacuum cycle from ambient air.*

Figure 52 - MABI dark vacuum cycle from atmospheric pressure nitrogen.

The MABI sample also shows a drop in CPD, however, in contrast to MAPI, the profile is different depending on the atmosphere. For the measurement from ambient conditions (Figure 51), the fall in CPD is gradual. Whereas, when pumping from N_2 (Figure 52), there is a plummet of similar nature to MAPI. The offset between beginning and end of Figure 51 shows more evidence that oxygen is affecting the dark work function in a similar way to MAPI.

5.3 Effect of pumping on light responses

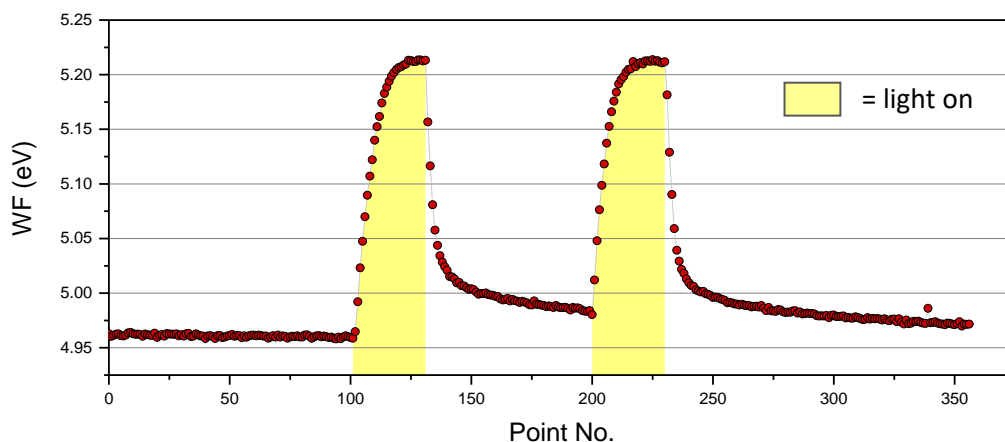*Ambient pressure light responses*

Sample: MAPI

Figure 53 - Work function light responses of MAPI in ambient air. Two pulses showing +250meV increase in work function.

The ambient MAPI responses in Figure 53 are in good agreement with previously reported data [95]. The work function increases by approximately +250meV meaning the fermi level is lowered by 0.25eV.
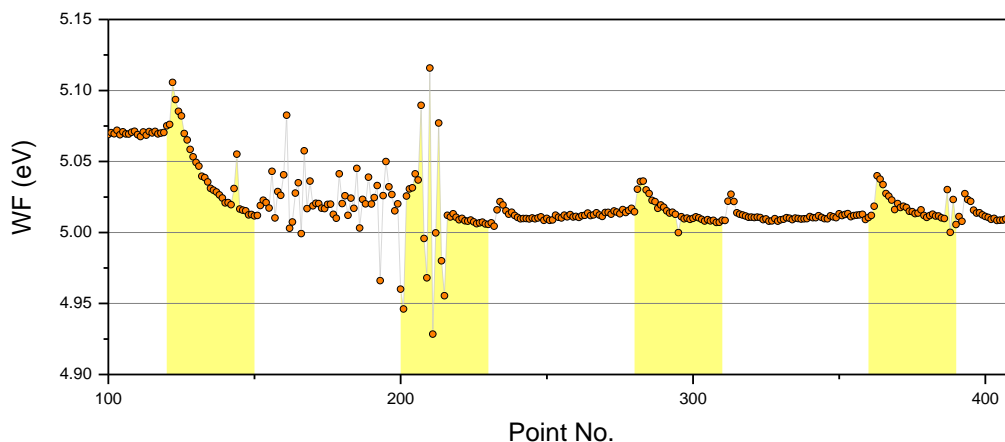
Sample: MABI

Figure 54 - Work function light responses of MABI in ambient air. The response is small and inconsistent.

The ambient light responses for MABI are not so reliable. The response is inconsistent. The measurement shows a -60mV drop, followed by +15mV spikes for the following light pulses. This makes studying the change in response after vacuuming more complicated. The region on Figure 54 from Point 150 to Point 220 is an example greater levels of noise that were common when using the UHV Kelvin probe system compared to the KP020 or APS04 systems. Frequent changes in noise were expected because the UHV Kelvin probe did not have a Faraday enclosure for radiation shielding. Movements of the arm or head during measurements could be enough to change radiation incident on the sample whilst in dark the condition. Additionally, the noisy signal could be linked to charges not recombining and remaining in trapping states since it occurs straight after illumination.

Low pressure light responses

The first attempts at measuring light pulses under vacuum were completed at pressures of 9.3×10^{-3}mBar for MAPI and 1.2×10^{-2}mBar for MABI. These were the pressures that the work function reached equilibrium in. The light pulses at these pressures yielded a small response for both MAPI and MABI (Figure 55 and Figure 56). The direction of the response is opposite to the ambient responses measured for each perovskite. This is demonstrated in Table 19, showing that there is a change due to the pressure dropping. In the case of MAPI, a second pulse was measured and it does not resemble the initial pulse.
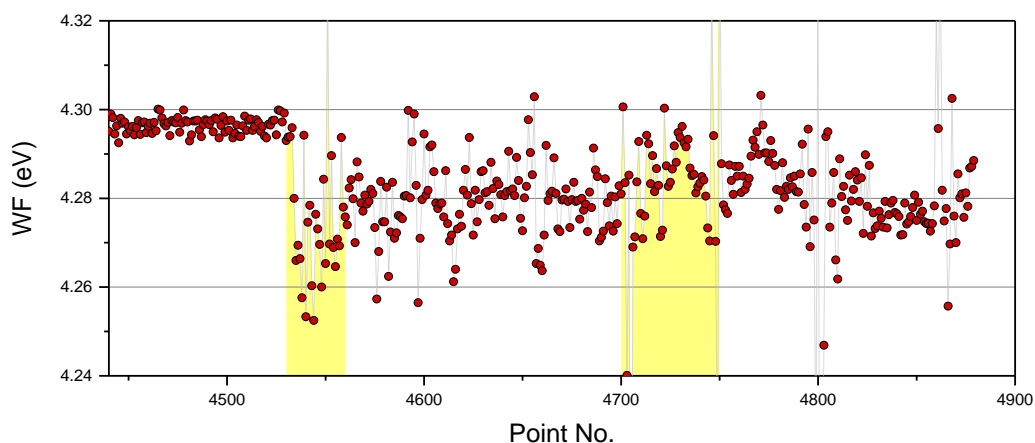

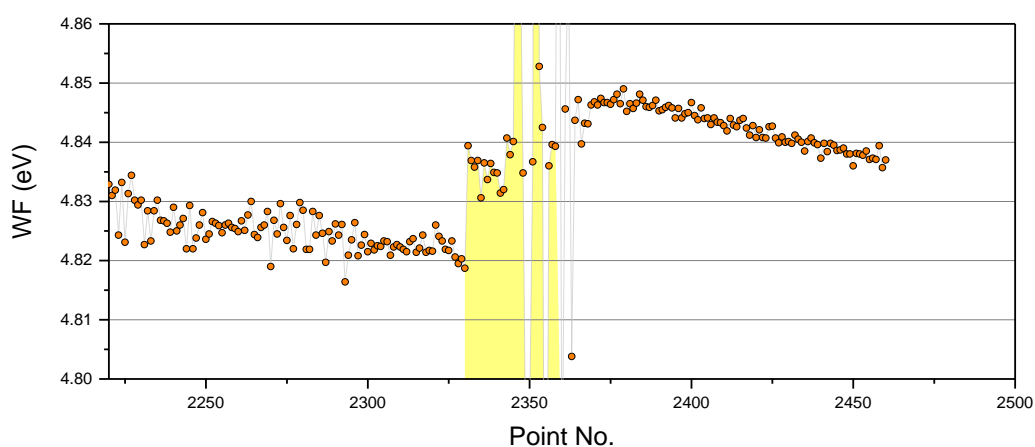*Figure 55 - Low pressure light response of MAPI. Pressure was approximately 9.3x10-3mBar.*

Figure 56 - Low pressure light response of MABI. Pressure was approximately 1.2x10-2 mBar.

Table 19 - Light response of MAPI and MABI before and after vacuum pumping. The direction for both perovskite's responses reversed after the pressure decreases.

	Light response (meV)	
Pressure	**MAPI**	**MABI**
Before pumping – 1.013 Bar	+250	-60
After pumping - 9.3x10^{-3}mBar, 1.2x10^{-2}mBar respectively	-40	+20

On following samples, the pressures were lowered further to 6.7x10^{-3}mBar for MAPI and 7.3x10^{-3}mBar for MABI. It is considered that achieving a better-quality vacuum has led to clearer and better-defined work function responses in both perovskites.

Consecutive light pulses have an effect on the direction of the response for MAPI as shown by the gradual transition from a positive response to a negative response in Figure 57 Detail B. Soon after, repeatable light responses are measured with pulses of equal time steps (Figure 57 Detail C). These MAPI responses inherit faster relaxation in comparison to the previous pulses and retain a high degree of stability with the peaks of the responses.
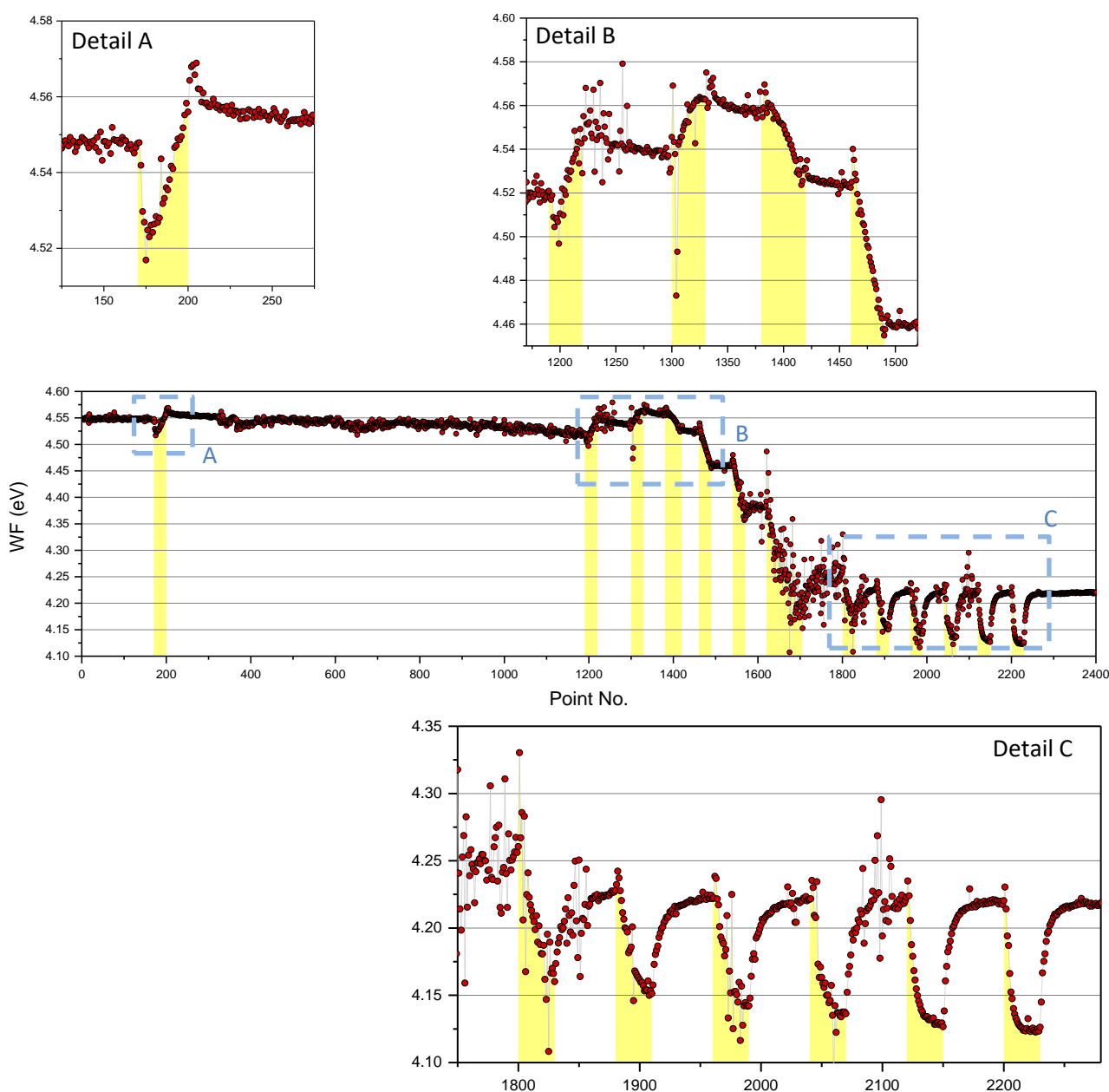

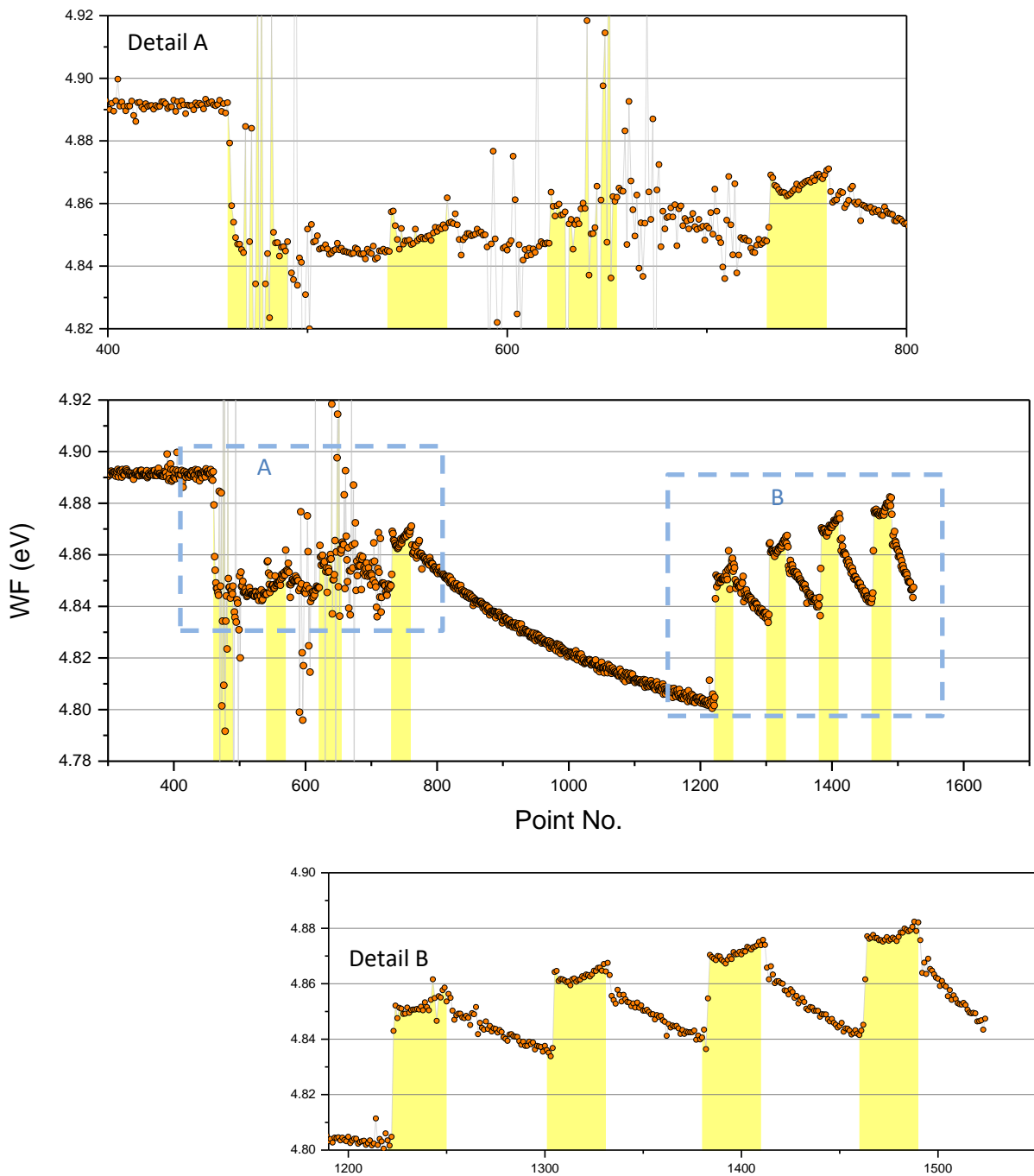*Figure 57 - Low pressure light pulses of MAPI with magnified details. Pressure was approximately 6.7x10-3 mBar.*

Figure 58 - Low pressure light responses of MABI with magnified details. Pressure was approximately 7.3x10-3 mBar.

The first succession of MABI pulses (Figure 58 Detail A) looks very similar to the ambient pulse in Figure 54, suggesting the vacuum condition does not have a significant effect on work function light response. Note how after Detail A, the dark work function does not return back to its original value. A second succession of light pulses is shown in Figure 58 Detail B. The responses are suddenly much sharper and greater in magnitude and have reduced noise – the reason for this is unknown. The relaxation gets faster each pulse. Perhaps the most significant find from Figure 58 Detail B is that distinct responses have been repeatedly measured with MABI – this shows there is some improvement in photovoltaic performance of MABI under vacuum conditions compared with ambient conditions.

To summarise, these measurements of light response for MAPI and MABI in a vacuum have shown that the work function change under illumination is certainly effected by the pressure. For the case of MAPI it should be highlighted that the light responses under vacuum show a poorer photovoltaic performance than the light pulses in ambient conditions as they are much smaller in magnitude and less consistent (Figure 57). It may be that this is directly caused by the extraction of oxygen from the surface in vacuum conditions as we suspected, however this has not been proved. It must also be said that the effect of lowering pressure to achieve vacuum conditions results in much poorer signal-to-noise ratio for both perovskites, as evident from Figure 55 to Figure 58. In general, the direction of light response is inconsistent in vacuum conditions for both perovskites, but both eventually showed a stabilisation of the response during pulses of light. The MABI light response under vacuum shows some promise for improved photovoltaic performance compared with ambient conditions (Figure 58 Detail B). However, it should be noted that this data was a preliminary investigation into the effect of vacuum conditions on dark work function and light response, and there were no repeat measurements.

Chapter 6. Conclusion

6.1 Summary

In undertaking this research, a better understanding of the differences between MAPI and MABI in terms of their energy levels has been gained. From review of literature we expected that Kelvin probe measurements would show that MABI has a smaller work function light response compared to MAPI, which is what we have reported. It is often reported that MABI has much better stability characteristics, which were captured by some work function ageing measurements. However, we do show that MAPI retained its good photovoltaic performance in terms of surface photovoltage over an age of 5 months. Using different Kelvin probe measurement techniques we produced labelled band diagrams for FTO-MAPI and FTO-MABI samples with a model of band bending and shifting of the fermi level across the thickness of the sample under white light illumination. The measurements of work function under white light and spectroscopic illumination deliver the general message that MABI generates a small and unreliable surface photovoltage. This in the context of a full cell means that MABI will not contribute to open circuit voltage as effectively as MAPI does. Surface photovoltage spectroscopy (SPS) showed that the MABI experiences a second photovoltaic effect that is not absorption of band gap photons. There remains ambiguity over what causes this effect.

6.2 Key findings

The white light response of MAPI is much better than that of MABI (Section 4.8)

The MABI samples tested did not respond to white light as well as the MAPI samples. The MAPI showed a consistent white light response of 250meV and the MABI showed inconsistent light responses of less than 50meV. Unknown optoelectronic effects complicate the response for MABI, and multiple light pulses showed that the MABI response reaches better consistency after around 6 pulses. MAPI also shows better performance through its faster decay.

SPS testing on MABI showed that illumination over a spectrum of 1000nm to 400nm causes the fermi level to fall then rise as the wavelength decreased. (Section 4.6)

The SPS measurements were very repeatable showing a minimum fermi level at around 700nm and a maximum at around 500nm. The 700nm effect is correlated with bandgap absorption, and we speculate that the 500nm effect is initiated by a second absorption from higher energy density states that is causing ionic charge diffusion to/from the FTO-MABI interface. A solar cell made with MABI could perform better if one of these effects was diminished.

Under illumination of 500nm at low intensity, MABI responds with a work function response of 120meV, a response that is larger and faster than MAPI. (Section 4.8)

MABI is known to have poorer photovoltaic performance than MAPI and the work function responses measured in white light are tiny in comparison. However, it is suspected that this is due to positive and negative effects on the fermi level cancelling each other out in white light. We reported a large response to 500nm light with MABI which is a significant result for demonstrating that MABI has potential to be used in tandem cells or other applications of light sensitive materials that involve low intensity green-blue light.

The MAPI sampled showed very good stability in surface photovoltage generated from white light illumination after 5 months of exposure to ambient air. (Section 4.10)

MAPI is regarded as an absorber with stability issues. Therefore, it was expected that the surface photovoltage generated under illumination would decrease with ageing. Instead we have shown that the response magnitude is almost unchanged after 5 months of shelf-life in ambient conditions. It is

expected that this is because the samples were protected from light degradation by black shielding containers. An equally good retention of surface photovoltage was also shown in the MABI after 5 months exposure, but this was less surprising. This is useful data for showing both perovskites do not degrade due to atmospheric gases.

MAPI and MABI both have strong CPD responses to vacuum pumping. (Section 5.2 and 5.3)

It is likely that a decrease in pressure draws oxygen out from the porous surface of the perovskite. Oxygen present around the surface may be slightly doping the material, which would explain a change in CPD as it leaves the surface. The light responses at lower pressures were completely different to ambient pressure. In the case of MABI, the response was better at low pressure, so one could test whether MABI devices have better efficiency under vacuum.

6.3 Future work

This work has covered a large range of photo-induced differences between MAPI and MABI. A considerable amount of further work and follow-up testing can come from the ideas explored throughout this thesis. These future investigations are described below:

Gradient measurements of perovskite samples of different thickness to check for gradient pulses increasing with thickness:

The Kelvin probe light pulse measurements revealed that the gradient variable from the Kelvin probe is sensitive to illumination. A simple validation test could be carried out with perovskite samples of increasing thickness. An increase in the gradient response to light for thicker samples would confirm that the gradient is detecting charge carriers moving across the layer thickness.

85°C heat exposure experiment:

The preliminary testing showed that MABI retained a dark work function value after exposure to heat better than MAPI. A repeat of the experiment needs to be carried out to show reliability in the results and should include more controlled storage of the samples. The effect of heat on UV-visible absorption can be explored in greater detail.

Layer-by-layer Kelvin probe measurements of a full cell with MABI:

This is an investigation that requires robust and repeatable manufacture of each layer of a FTO/ETL/perovskite/HTL structure, where batches are manufactured adding a layer each time. The differences in work function responses would show which layer contributes most to V_{oc} and which combination of transport layers works best. Similar investigations have been reported for architectures with MAPI but not with MABI [75][120].

Effect of a vacuum on the work function of MAPI and MABI:

This investigation was attempted at a preliminary level and showed some interesting results. A change in dark work function due to pressure is displayed in Section 5.2, but explanations were only

speculative. The results show that the work function response may be improved under vacuum for MABI which is certainly worth explored further. The MAPI light response is much smaller and inconsistent under low pressure. As previous reports have stated that MAPI degradation is more rapid in oxygen conditions [109][108][107], the light response could be tested in nitrogen at atmospheric pressure.

Perovskite film synthesis optimisation for largest light response e.g. different annealing times, spin-coating settings:

Much optimisation of manufacturing procedures has been documented for PCE results. Literature review in Section 1.3 highlights improvements to the manufacturing process that can be tested for MAPI and MABI. No process optimisation alongside work function light response was found in literature. A larger light response means a larger V_{oc} in a full cell architecture. Therefore, one could carry out a Taguchi Design of Experiments for optimisation of work function by changing variables in the manufacturing steps used.

Humidity sensitivity testing:

The humidity levels in the Faraday enclosure can be mildly controlled by using cups of water and desiccant within the enclosure. By changing number of cups in the enclosure and amount of desiccant the humidity can be independently changed to see if there is a strong relationship between work function light response and humidity.

Further investigation into the variable work function of FTO:

FTO is reported to have a wide range of work function values that is likely to depend on the supplier. However, in this work it was measured that FTO work function changed due to plasma cleaning treatment and illumination. These two relationships should be investigated further, because understanding the work function dynamics of FTO will help to understand the work functions of the layers above. The thorough investigation into work function of FTO reported by Helander et al could be useful for reference [102].

Appendix A

FTO measurements
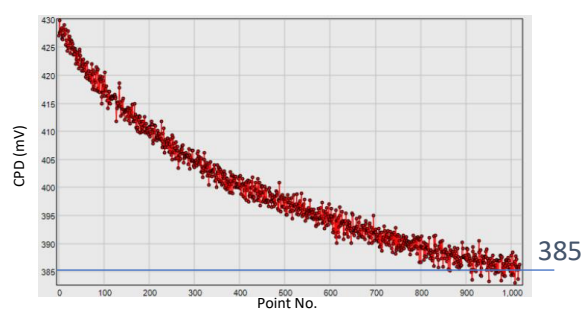
Work function of FTO

The FTO measurement was very important to understand the band diagrams (Figure 32). The FTO work function was measured in a second visit to KP Technology (Figure 59 bottom graphs). These FTO substrates were cleaned with the same steps reported in the experimental methodology (Section 2.1) without the O_2 plasma cleaning.

To resolve the issue of measurements being completed at a different time to the perovskite dark work functions used on the full band diagram (Figure 32), a reference work function for each perovskite was measured to show any systematic offset that might be present (Figure 59 top graphs).

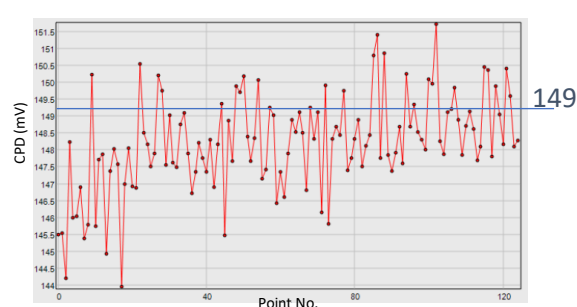MAPI
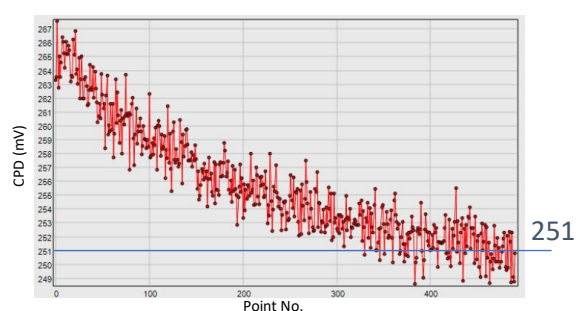
MABI

FTO Sample A
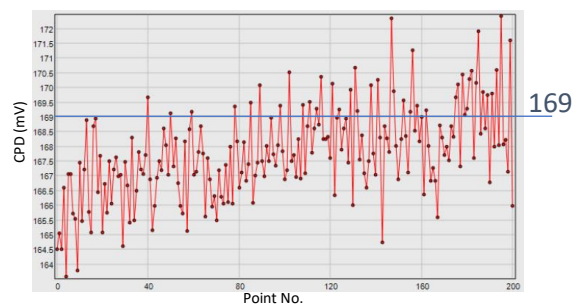
FTO Sample B

Figure 59 – CPD measurements for dark work functions of FTO and both perovskites for reference.

FTO average CPD = (169+149)/2 = 159 mV

Tip work function during measurements in Figure 59 = 4.702 eV

(Calibrated with -52mV CPD from Ag of work function 4.65 eV)

FTO work function = 4.861 eV

Reference MAPI work function = 4.702+0.251 = 4.953 eV

Reference MABI work function = 4.702+0.385 = 5.087 eV

These reference values are approximately 100mV above the values measured for MAPI and MABI dark work function scans in Section 4.4 (Figure 32).

Therefore, **corrected** FTO work function = **4.761 eV**

APS measurement of FTO

The APS measurement of FTO was not straight forward. The photoemission threshold (PE) measured for semiconductors is usually used as an estimate for HOMO (or valence band maxima for inorganic semiconductors). However, in the case of FTO, strong n-type doping results in many electrons existing in the conduction band. The photoemission threshold is where the cubic root plot intersects the baseline, and, in the case of FTO, it is reached at the energy of conduction band electrons for FTO (Figure 60).
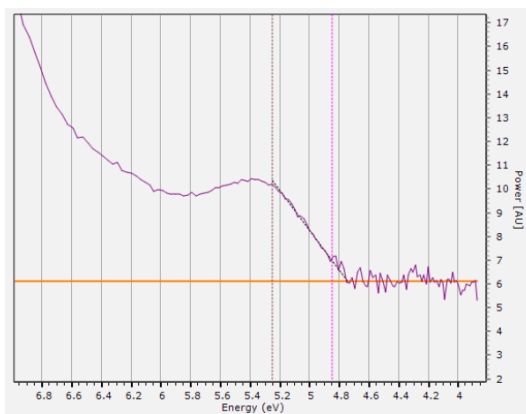
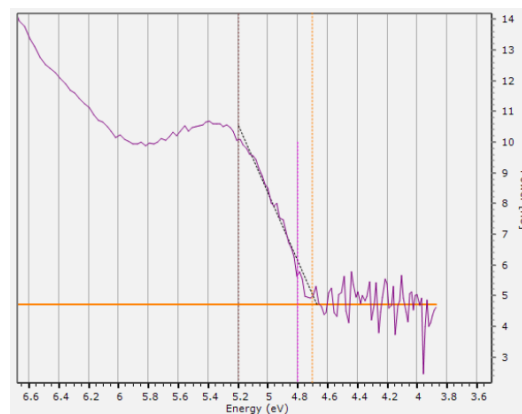FTO Sample A   FTO Sample B

Figure 60 – FTO APS cubic root plots with -70V bias.

Average PE   = 4.710 eV

Work function of FTO (previous page)   = 4.761 eV

The raw data in Figure 61 shows that the photoemission might be rising and falling with the conduction band and valence band energies as shown by the shaded regions. This is only speculation but would be well worth further investigation. On the band diagram in Figure 32, the FTO is presented with the fermi level inside the conduction band. This makes sense because FTO is a degenerate n-type semiconductor and is so rich in electrons that it could be characterised as a semimetal (other literature shows the fermi level could be located inside the conduction band [102]).
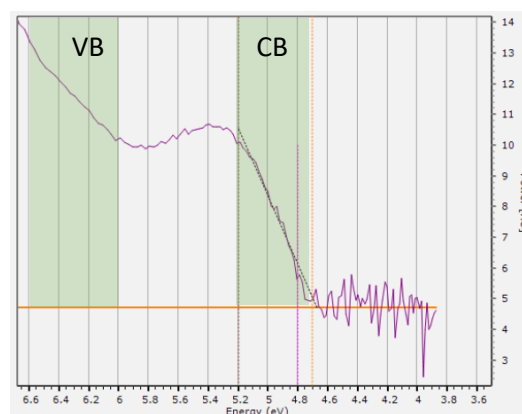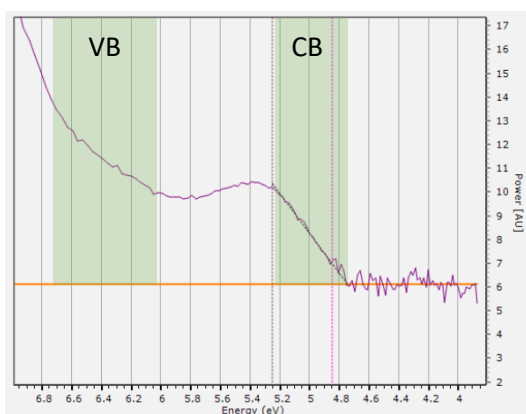

Figure 61 – APS Plots with possible energy band regions highlighted.

As well as acquiring the work function measurement for FTO, two other relationships were noticed:

-         a decrease in work function under illumination

-         an increase in work function due to O_2 plasma treatment

FTO is an n-doped semiconductor, is more of a semimetal because it has a reservoir of free electrons like a metal would. It is not an intrinsic semiconductor, so a response upon illumination was not expected.
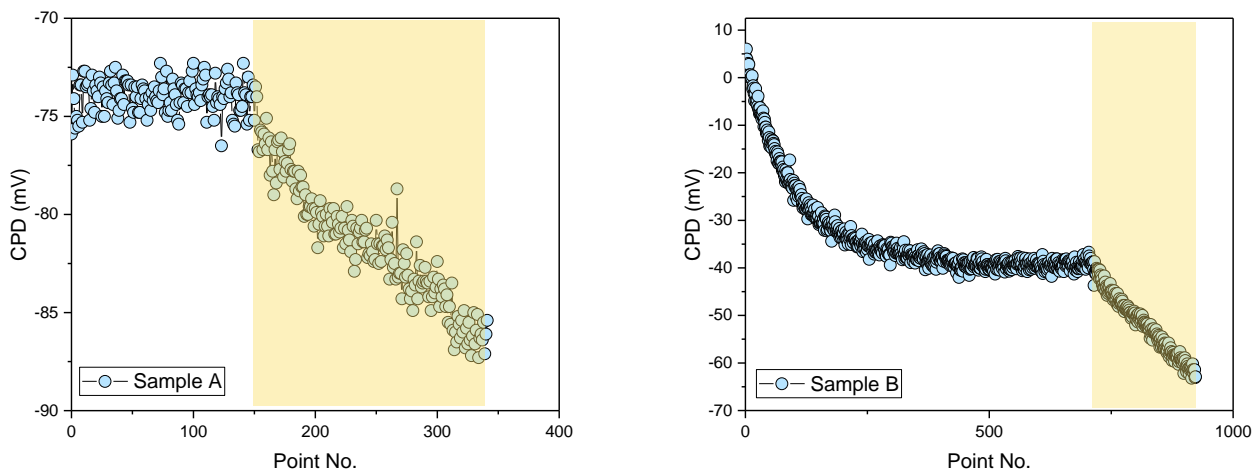

Figure 62 – CPD plots showing FTO has a response to illumination.

Figure 62 backs up that FTO is a far more complex material than expected. The light responses are similar for the two samples tested. The effect is unlikely to be temperature related because the change in gradient happens instantly and radiative heating from the light would be relatively weak. Further investigation is required into FTO for its semiconductor characteristics that have proved to be more complex than expected. The heating power of the light source is a suggested measurement for future, in order to test whether temperature of a glass substrate increases significantly under illumination.

FTO affected by O_2 plasma cleaning

FTO substrates are O_2 plasma cleaned just the perovskite precursor is spin-coated on top. For this reason, the work function of FTO was measured for substrates that had just been plasma cleaned. The work function was much higher than previously - around **800mV** CPD and decreasing at a constant rate. These measurements were not saved because it was believed they were erroneous. However, after reading in literature that FTO has been shown to have an increase in work function of around 100mV with plasma treatment [102], it is likely the result was a true effect of plasma treatment. It has been shown that it is not associated with reduction of carbon contamination [102].

Characterisation measurements

X-Ray Diffraction measurements

X-Ray Diffraction was used to identify the composition of the manufactured samples (Figure 63). The manufacturing procedure for MAPI was well practised within the research group so there was strong confidence that it would produce ABX_3 crystals, but the MABI procedure was less used so the XRD provided a means of gaining confidence that the samples were ABX_3 or $A_3B_2X_9$ as commonly seen in literature [41][105]. Each plot represents a different location on the same sample.

MAPI XRD results:
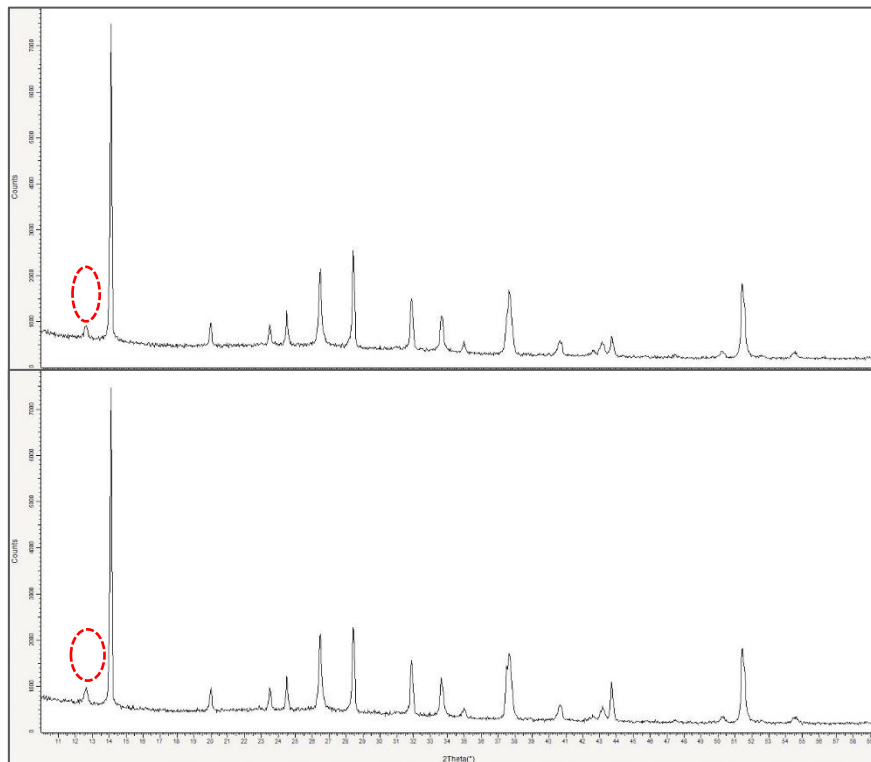
○ = peak at 12.5 possibly showing unreacted PbI_2 and BiI_3

Figure 63

MABI XRD results:

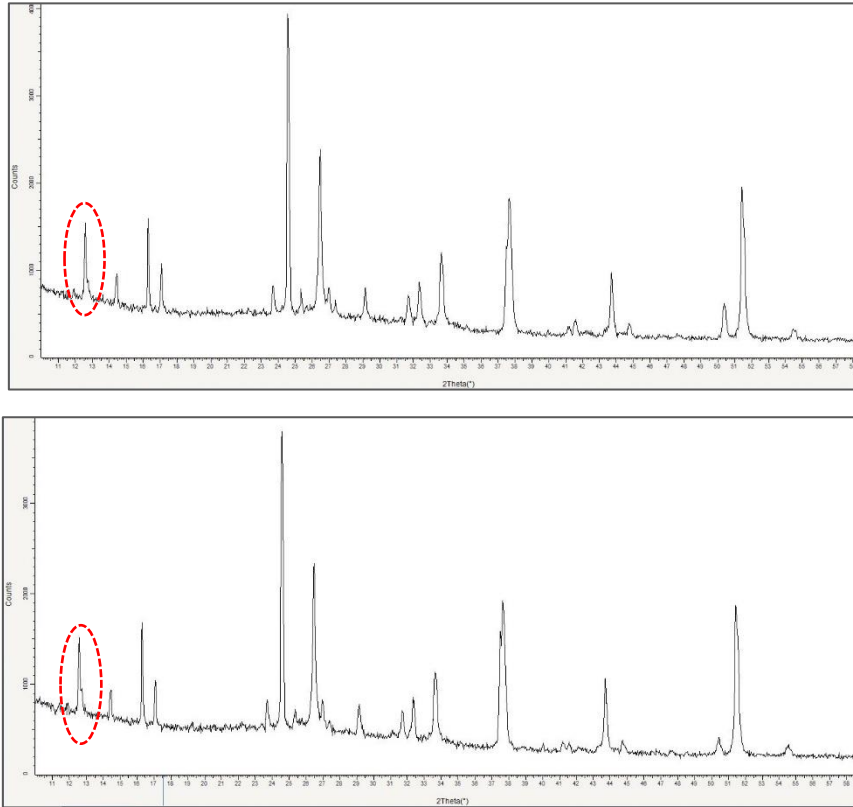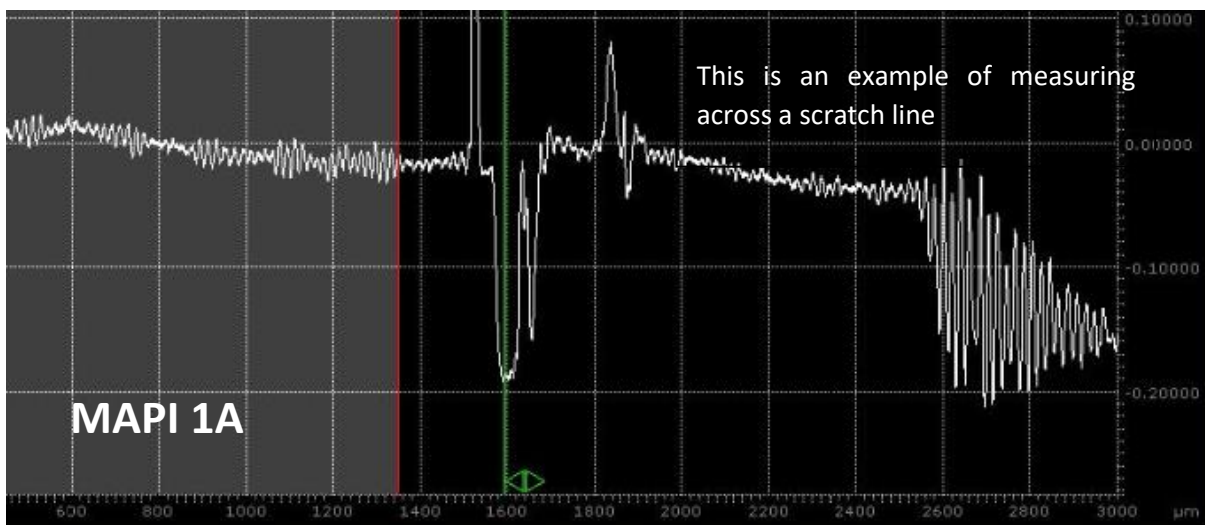*Figure 64 – XRD data*

Perovskite thickness measurements

Table 20 – Thickness values of perovskite layer measured using a Dektak profilometer.

		Thickness (nm)	
Perovskite	Sample	A	B
MAPI	1	185	732
	2	504	260
	3	160	160
	4	200	210
	5	170	170
MABI	1	831	1133
	2	812	
	3	1270	680
	4	580	820
	5	740	820

Table 21 – Average thickness values of measurements from Table 20.

	Average thickness (nm)	Standard Deviation (nm)
MAPI	275	±181
MABI	850	±203

This is an example of measuring across a scratch line

MAPI 1A

MAPI 1B

This is an example of measuring across the boundary of a scraped region
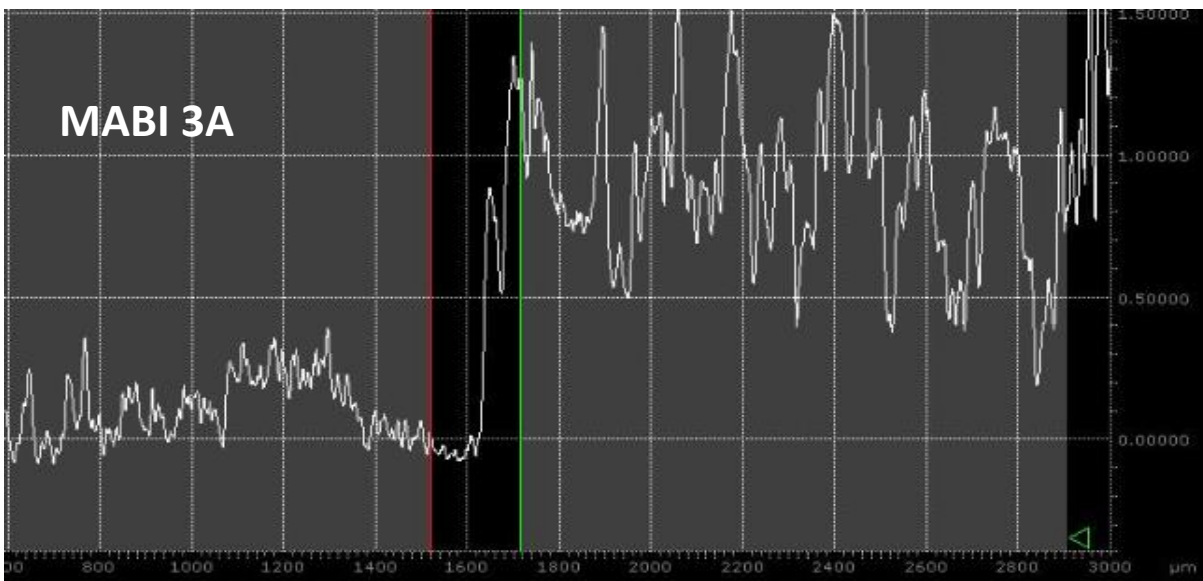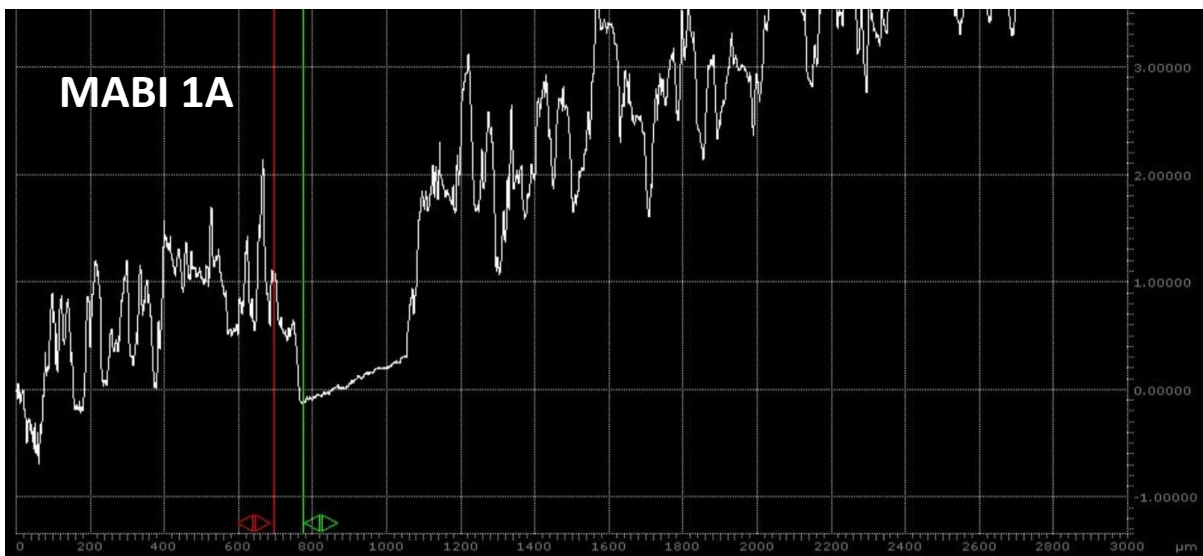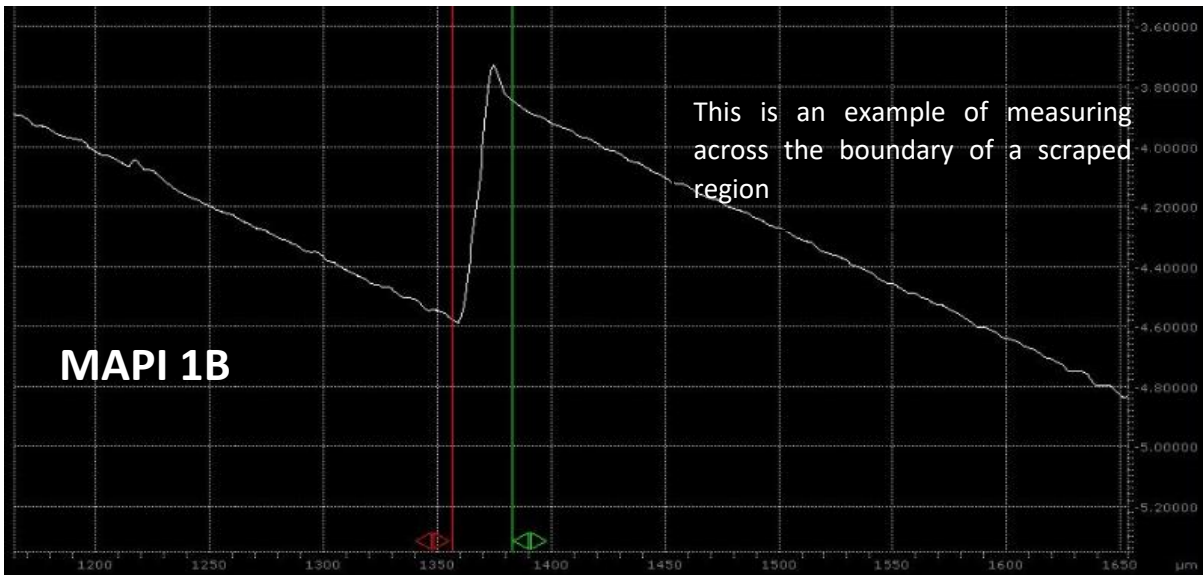
MABI 1A

MABI 3A

Figure 65 – Example plots of the profilometer signal for measurements made.

The MABI films are substantially thicker than the MAPI films. The spin coating settings were the same for the synthesis of both perovskites. Therefore, the reason for the difference in thickness is likely to be due to the anti-solvent dripping step that is only part of the MAPI procedure. Data for both materials have a similarly large standard deviation of around ±200nm, so the averages should be regarded as rough. This results in percentage errors or ±65% and ±24% for MAPI and MABI respectively. The anti-solvent dripping is completed by hand, so human error is considered in the ±65% error on the thickness of MAPI samples.

Surface roughness is visibly larger for MABI, shown by the example plots where the peaks and troughs are larger for MABI (Figure 65). MAPI 1B screen capture shows the data has a flatness gradient before the material etching has been reached. This is an indication of non-perpendicular angle between the surface plane and the profilometer tip.

A summary of the perovskite thicknesses from literature is shown in Table 22. From the examples in the table, a reasonable perovskite film thickness would be between 100-1000nm going off the variation shown from slightly different methodologies.

Table 22 – Thicknesses of MAPI and MAB found in literature compared with this work.

Absorber	Thickness (nm)	Reference
MAPI	150	[75]
	340	[78]
	650	[80]
	250	This work
MABI	584	[90]
	250	[48]
	80-150	[91]
	850	This work

Ambient Pressure Photoemission Spectroscopy

Here are plots from the ambient pressure photoemission spectroscopy reported in section 4.5. Figure 66 includes the plots from the repeat measurements so that the repeatability can be seen.
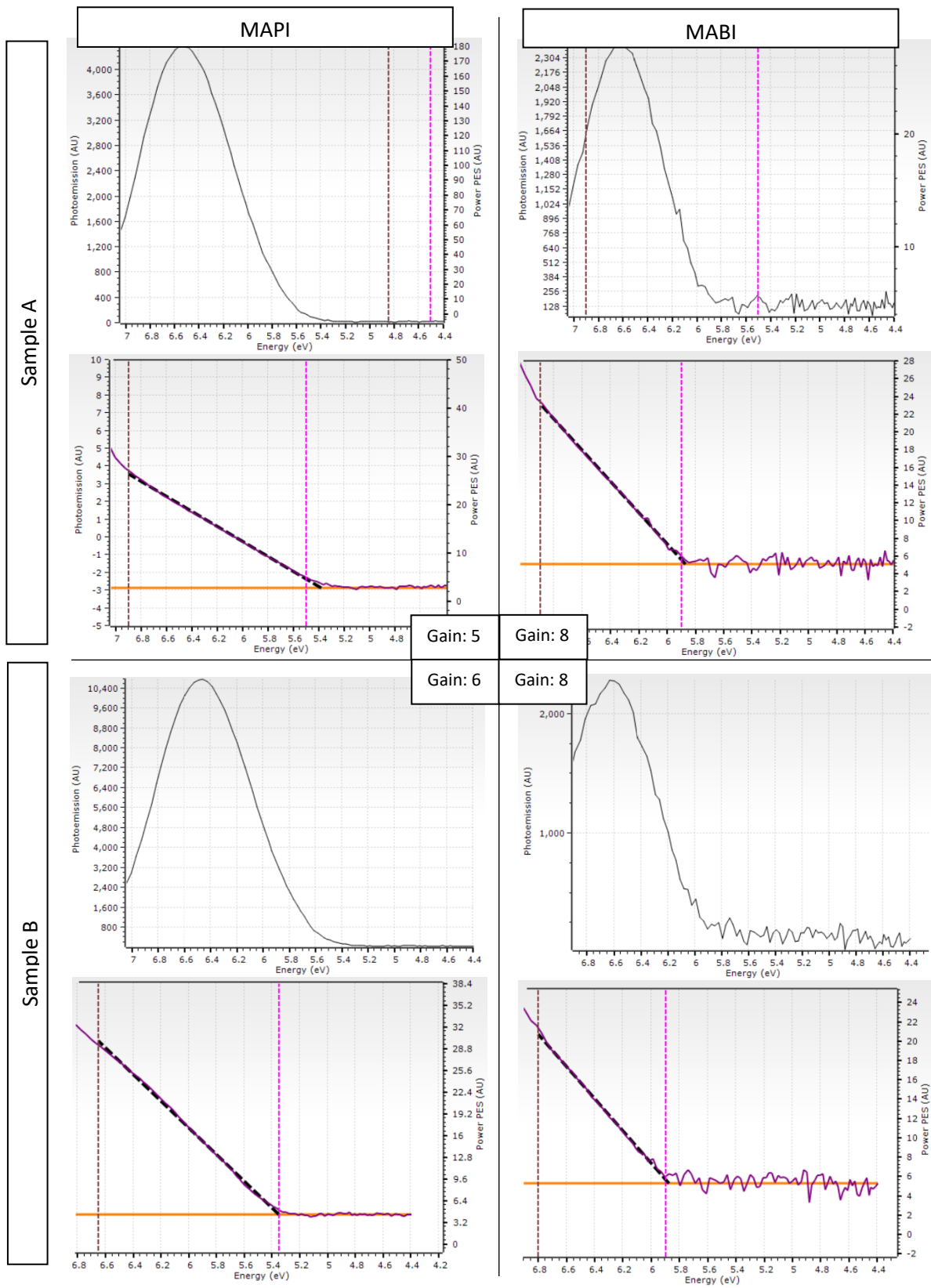

Figure 66 – APS data for all samples reported in Section 4.5
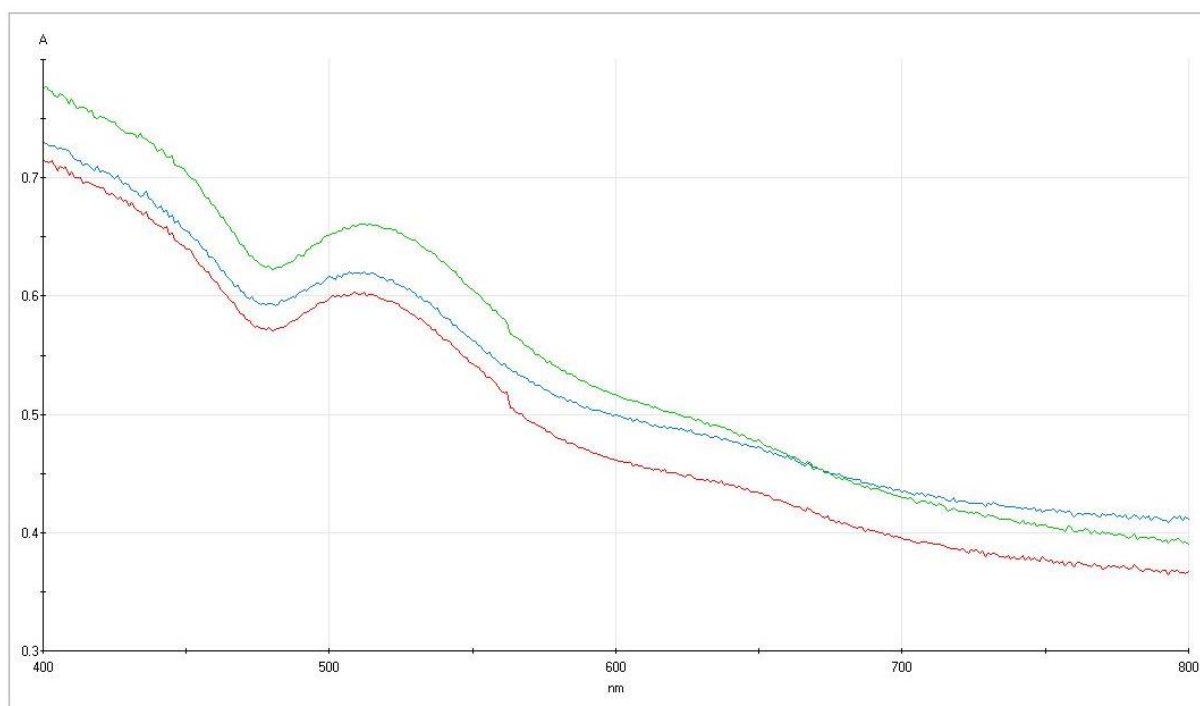
UV-visible Spectroscopy
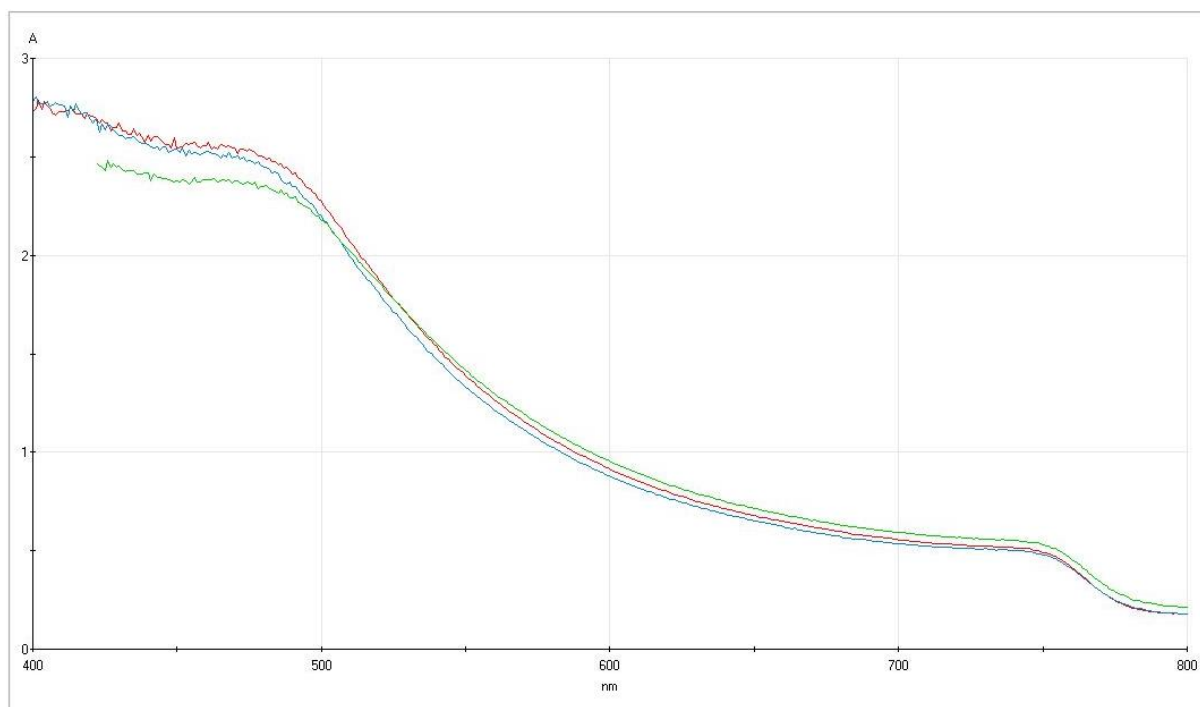
Figure 67 – UV-visible absorption data for MAPI (top) and MABI (bottom).

Extra analysis

Further work on SPV measurements

Figure 68 shows the SPV plots on a logarithmic intensity axis. It highlights the linear regions of the function more clearly. It is also worth noting that the plot shape does not change dramatically compared to the linear axis plots in Section 4.7.

Figure 68 – SPV plots of MAPI and MABI from Section 4.7 on logarithmic axis.

Next, are the monochromatic SPV measurements for 500nm and 700nm light shown on a logarithmic scale (Figure 69). Here, linear regions are much more pronounced than on the linear axis.
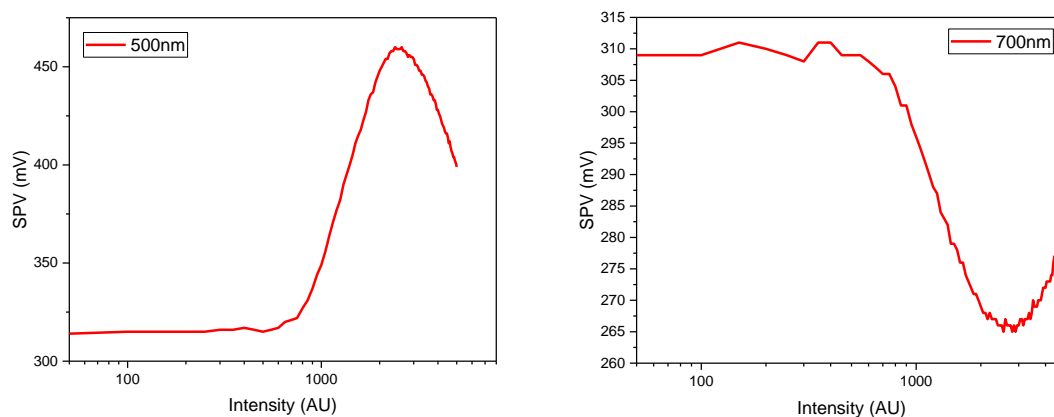
Figure 69 – Monochromatic SPV plots for MABI from Section 4.7 on a logarithmic scale.

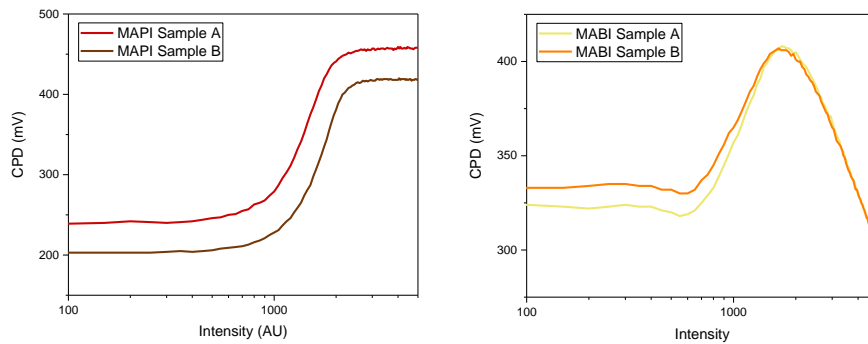The same monochromatic wavelengths were measured at different speeds and the results showed large contrast at high intensities especially for 500nm light (Figure 70). A plausible explanation is a slow effect acting against the change in CPD which dominates the response after enough time under illumination. The fast responses are less affected by this because the measurement is quicker. The CPD for 500nm light at maximum intensity end up below the dark value which is strange.

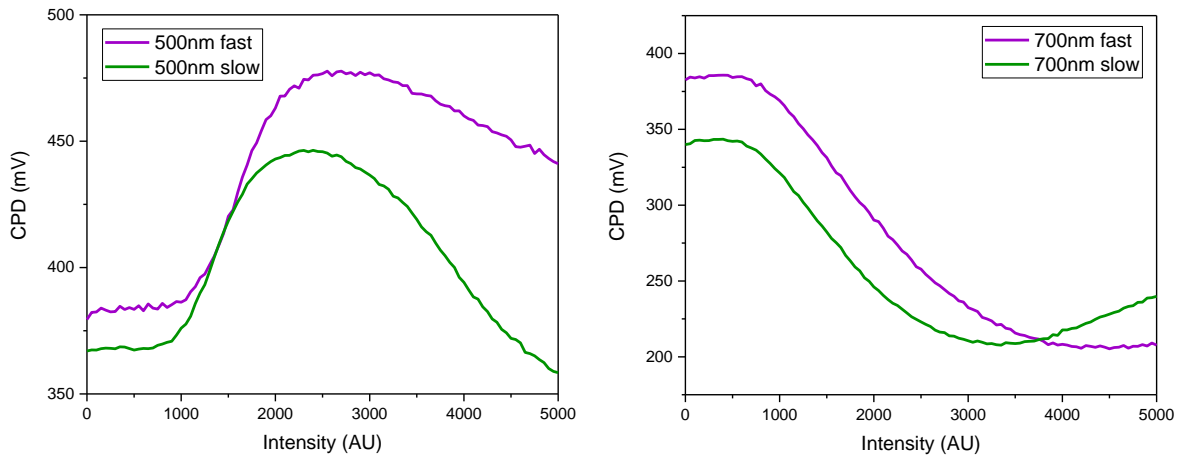*Figure 70 – Monochromatic SPV plots for MABI from Section 4.7 with changing the measurement speed.*

Analysis of decay of work function to dark equilibrium

Figure 71 and Figure 72 display differences between the two material's decays using a logarithmic time axis. Results are analysed on a logarithmic scale of time to highlight separate functions. MAPI has a relatively fast decay represented by one straight line (Figure 71). After the decay, there is another function which we suggest is environmental change. For MABI, there are two decay processes going on because there are two decay functions. It appears that the decay back to dark equilibrium is extremely slow and is initially disguised in a faster decay effect with opposite gradient (Figure 72).

This plot data is taken from the light pulse cycles in Section 4.9. The X axis has been transposed to begin after the final pulse to capture the decay back to dark equilibrium.
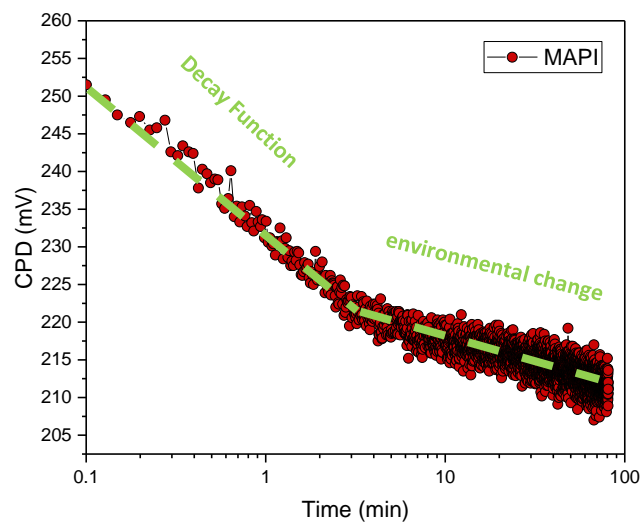

Figure 71 – MAPI dark decay after 100 light pulses. This data is taken from Section 4.9. Two similar functions are visible.
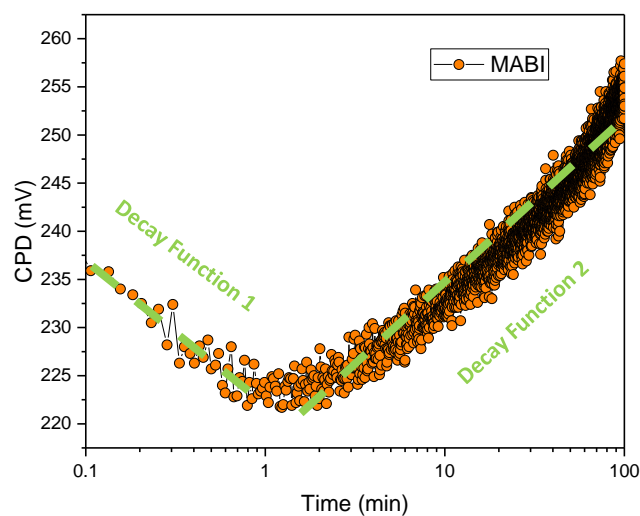
Figure 72 – MABI dark decay after 100 light pulses. This data is taken from Section 4.9. Two dissimilar functions are visible.

Gradient sensitivity to charge generation

The gradient variable logged on the Kelvin probe software, is used to lower the probe to the correct distance above the sample. It is understood that when a material is close enough to the Kelvin probe tip, the gradient signal can change depending on the gap between. The units of gradient are arbitrary. By measuring the gradient during light pulses, it is clear that gradient can detect generation of charge (Figure 73 and Figure 74).
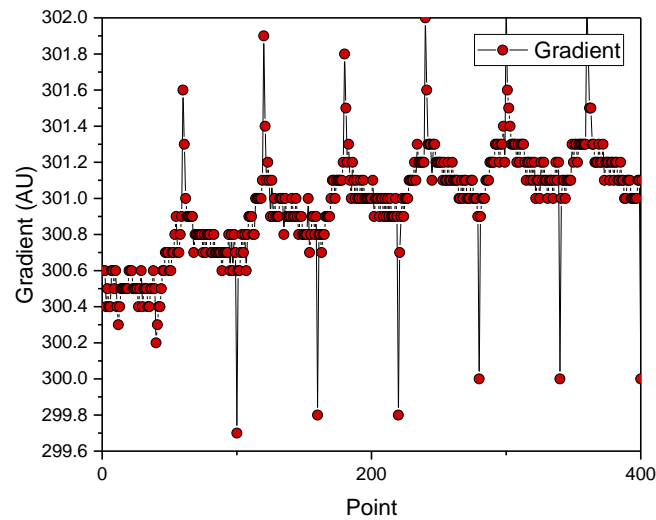
Figure 73 – MAPI gradient values during light pulses showing increases in gradient under illumination.
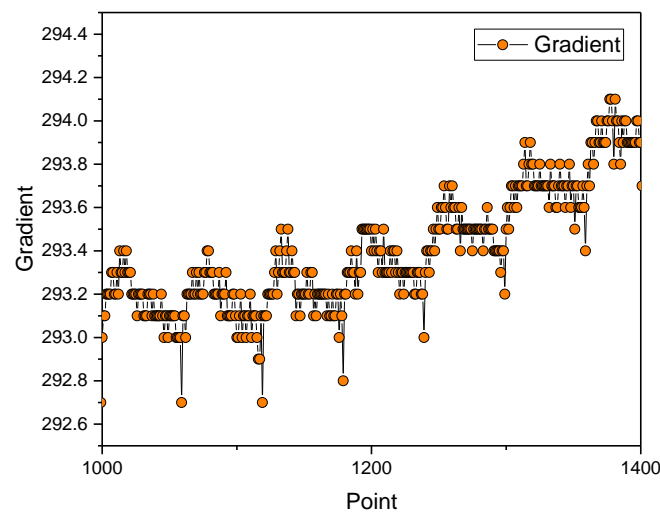
Figure 74 – MABI gradient values during light pulses showing increases in gradient under illumination.

It is likely that the gradient in dark is mainly sensitive to the electrons in the FTO layer a few hundred nm below the perovskite. Under illumination the charges are generated and detected closer to the tip by as much as the thickness of the perovskite. Therefore, a thicker layer of the same perovskite should result in a larger change of gradient.

Appendix B

Preliminary testing on 85°C heat exposure effects

Reported is some preliminary testing completed to gather initial results on how the photo-induced characteristics of MAPI and MABI change with heat exposure. More specifically, the dark work function, UV-visible absorbance and photoluminescence are monitored in-between heating of samples at 85°C for 20 minutes. The UV-visible absorbance was measured to observe where the absorption peak is. This peak would then be used to gauge what wavelength to run the photoluminescence measurement at.

The data shows a relationship between heating and absorbance, where grain structure could possibly be cycling between polycrystal structure and larger grain structures due to thermal degradation followed by fusing of grain boundaries. This cycling is a model proposed to explain the strange UV-visible data gathered for MAPI. The UV-visible data was expected to show a drop in absorbance. It was predicted the MAPI would show a larger decrease in absorbance; suggesting it is more vulnerable to high temperature degradation. Instead the MAPI absorbance drops after 20mins heat then returns to its initial value after 40mins heat. The MABI absorbance decreases each time and totalled a larger decrease than the MAPI – not what was expected.

Day 1

1. 3xMAPI samples, and 3xMABI samples are manufactured using spin coating method.
2. The three samples for each MAPI and MABI are labelled as follows:

   Sample 1 - baseline sample for WF measurements after 0 minutes of heat

   Sample 2 - for UV-visible/PL measurements after 0, 20, and 40 minutes of heat

   Sample 3 - for WF measurements after 20, and 40 minutes of heat

(the following steps were carried out for both perovskites)

Day 2

3. 0mins of heat WF measurements are completed for Sample 1
4. 0mins UV/PL measurements are completed for Sample 2
5. Sample 2 and 3 are placed on hotplate at $85°C$ for 20 mins
6. Sample 2 and 3 are left to cool back to room temperature on an aluminium plate. Films are covered by a dark cover.
7. 20mins of heat WF measurements are completed for Sample 3
8. 20mins of heat UV/PL measurements are completed for Sample 2

Day 3

9. Sample 2 and 3 are placed on hot plate at $85°C$ for 20 mins
10. Sample 2 and 3 are left to cool back to room temperature on an aluminium plate. Films are covered by a dark cover.

Day 4

11. Completed WF measurements for Sample 2 and 3 after 40 minutes of heat
12. Completed UV/PL measurements for Sample 2 and 3 after 40 minutes of heat
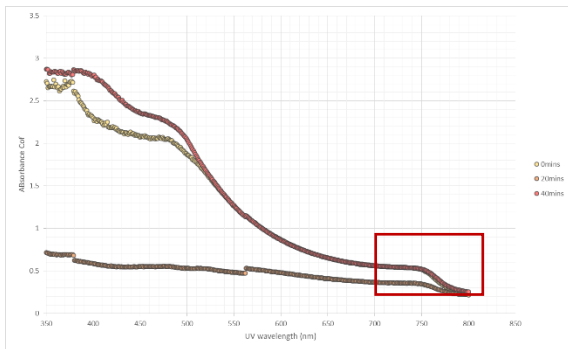
MAPI Data

Peak: 750nm

Absorbance Coefficient:
0mins	0.51
20mins	0.35
40mins	0.52
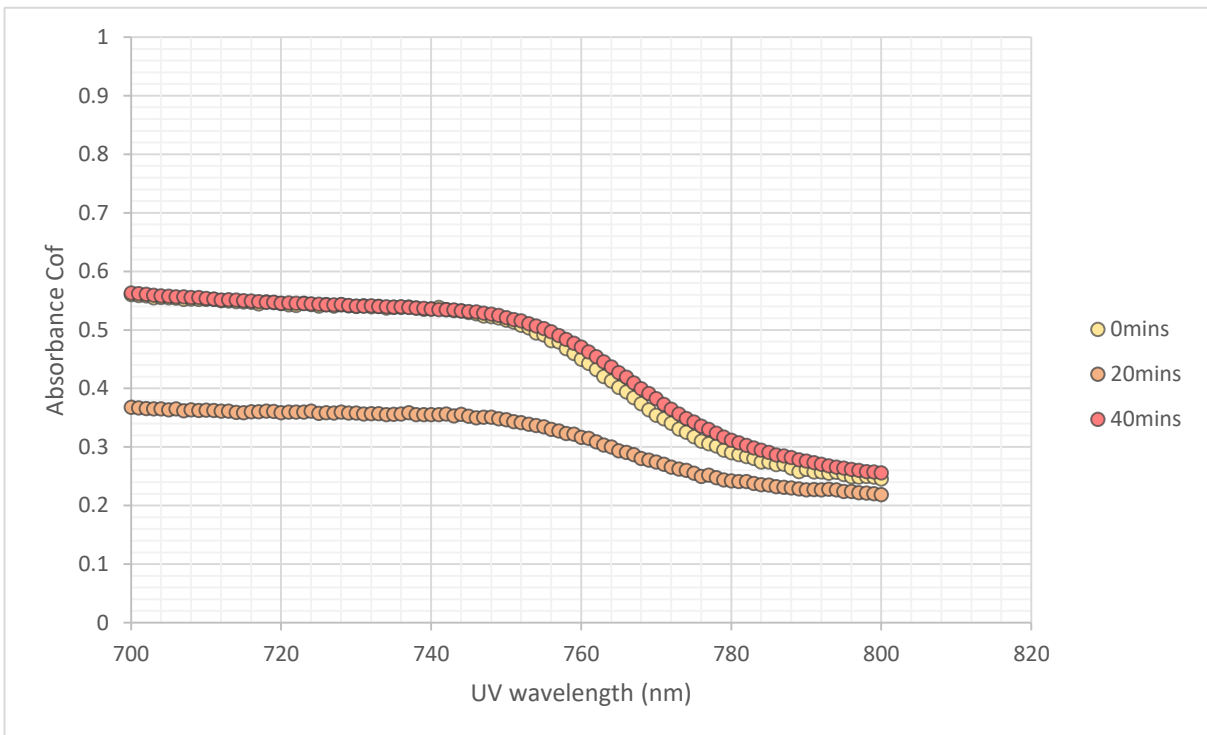
Figure 75 – UV visible data for MAPI with different amounts of heat exposure.
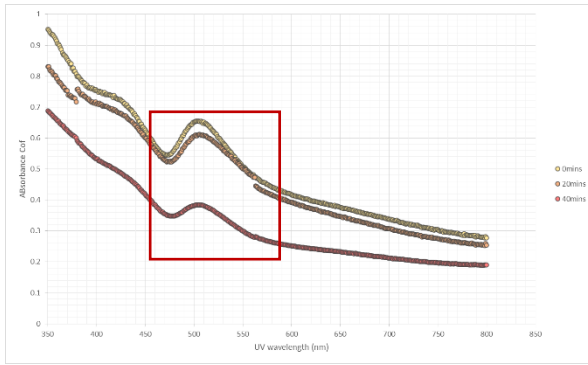
MABI Data

Exciton peak: 504nm

Absorbance Cof:
0mins	0.65
20mins	0.61
40mins	0.38
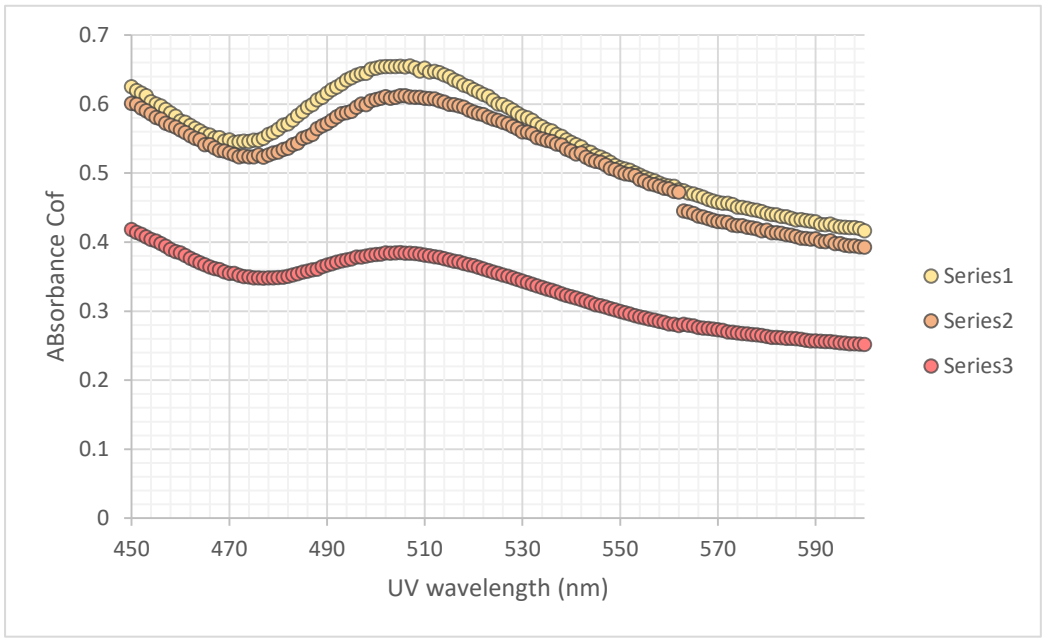
Figure 76 – UV visible data from MABI with different amounts of heat exposure.

The overall range in absorbance coefficient for both samples is ≈0.2. Both perovskites have an initial offset which is visible at 800nm. (Figure 75 and Figure 76)

Decrease in the absorption coefficient after heating is likely to be due to crystals breaking down; creating smaller grains. Strangely, the MAPI absorbance recovered back to its initial coefficient between 20-40mins of heating. This could be due to the grains degrading initially after the first period of heating. Then the boundaries trap light and moisture over night that fuse the gains back together when heated a second time – returning the grains to their original size.

The photoluminescence (PL) highlights the intensities of wavelengths of light emitted from a sample upon illumination of light of wavelength equal to the exciton peak (derived from UV-visible spectroscopy). Figure 77, Figure 78 and Figure 79 show MAPI and MABI PL graphs alongside one another.
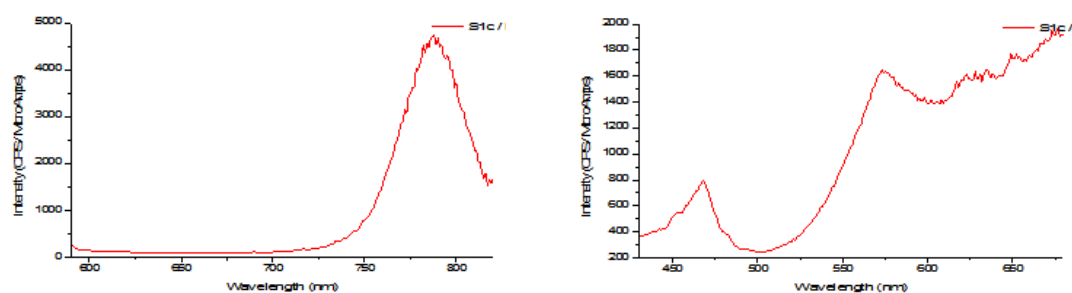
Figure 77 – 0 mins heat, Photoluminescence for MAPI (left) and MABI (right).
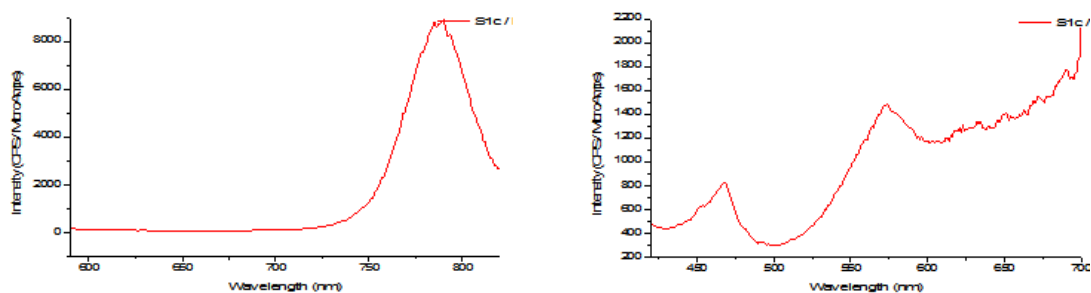
Figure 78 - 20mins heat, Photoluminescence for MAPI (left) and MABI (right).
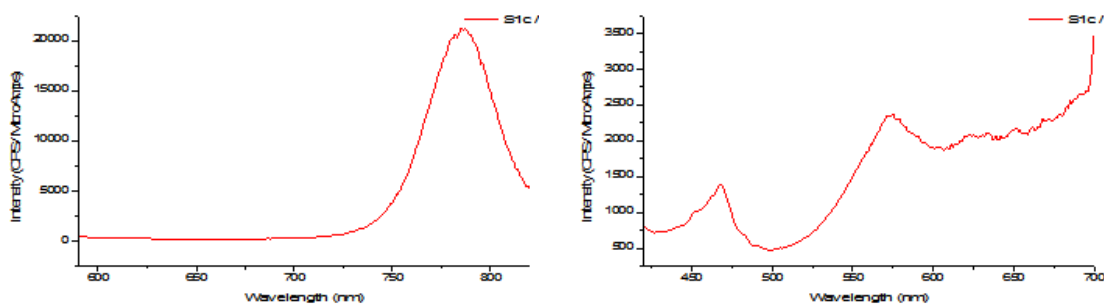
Figure 79 - 40mins heat, Photoluminescence for MAPI (left) and MABI (right).

Table 23 - Summary from Photoluminescence data.

Heating time at 85°C (mins)	Intensity (CPS/microAmps)	
	MAPI	MABI
0	4750	1650
20	8900	1500
40	22500	2350
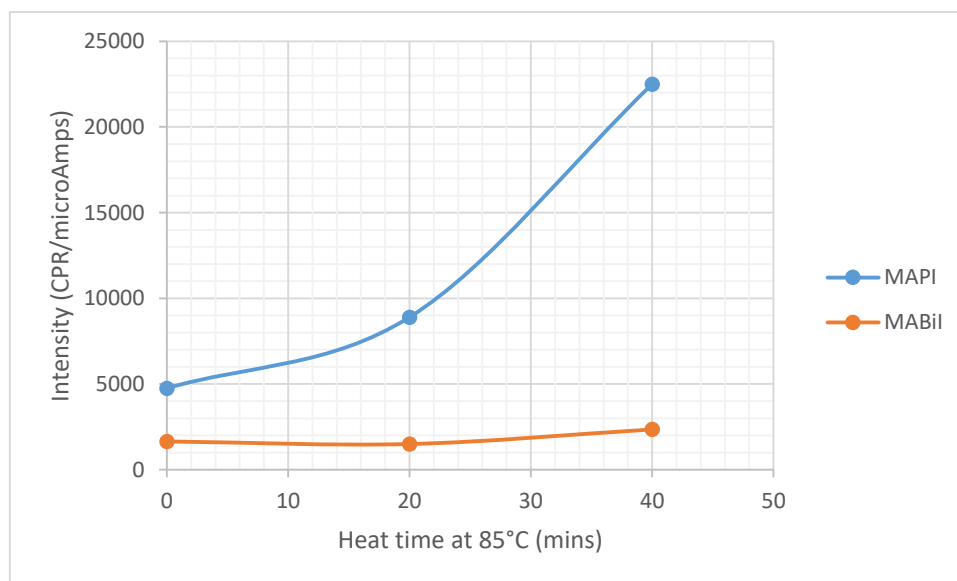
Figure 80 - Photoluminescence intensity changing with heat exposure for both perovskites.

Photoluminescence is a measure of the intensity on photons exerted from a material following illumination. The data gathered shows clearly that the change in PL for MAPI is far greater than that of MABI (Figure 80). This suggests MABI is more thermally stable. The MAPI PL increases by a factor of larger than x5 after 40 mins at 85°C. This suggests some of the following possibilities:

- the surface becomes purer from contaminants evaporating during heating
- more atoms are emitting photons
- more electrons are excited

It is worth noting that the PL has an iterative effect on samples that are tested multiple times. This should be quantified before repeating PL measurements.
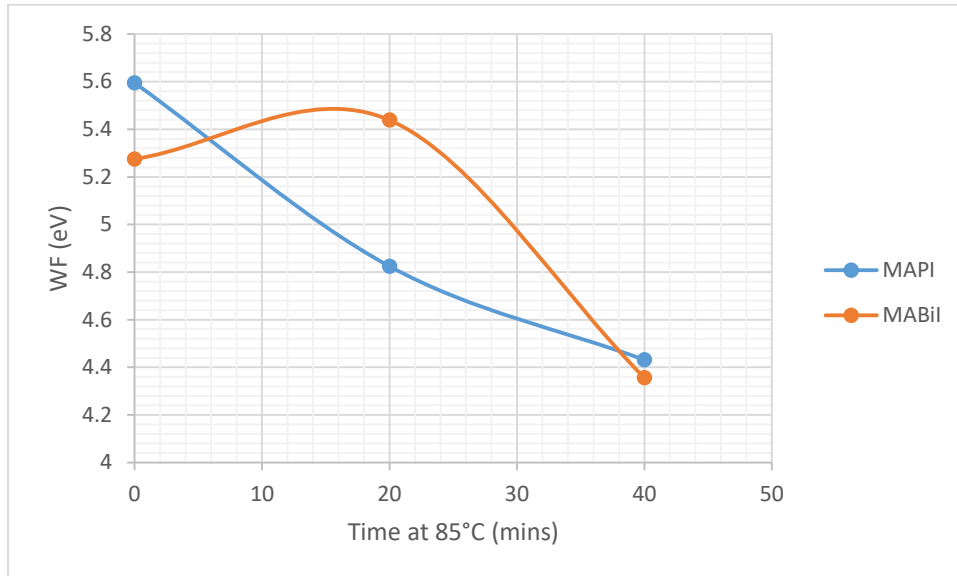
Figure 81 - Work function changes with increasing heat exposure for both perovskites.

The data shows the work function is more stable for MABI than MAPI between 0≤ time <20 (Figure 81). From dark work function ageing in Chapter 3, the work function ageing proved to be less than 0.2eV in 7 days (Figure 29). Therefore, the trend is not heavily influenced by work function ageing over the time period of the testing.

The overall decrease in WF of both perovskites suggests the material fermi level is shifting towards the n-type region of bandgap. In the region after 20mins of heating, the work function for both samples drops similarly. However, the data point at 40mins suggests the gradients are very different. A drop in work function means, less energy is required to remove an electron from the surface of the sample. Maybe electrons are gaining kinetic energy from the heating and moving closer to the material surface.

To understand the trend further, more data needs to be gathered.

Appendix C

Other

Energy level data from literature

Table 24 – Relevant energy level data found in literature.

Sample	HOMO level (eV)	Fermi level (eV)	Band gap (eV)	Ref
FTO		4.4		[121]
FTO		4.4-4.7		[122]
FTO		5.0		[102]
FTO/MAPI	5.31	5.1	1.3	[75]
FTO/MAPI	5.47	5.1	1.57	[95]
FTO/MAPI	5.91	4.22	1.7	[103]
$MA_3Bi_2I_9$			2.9	[91]
MABI			2.04	[88]
$MABi_3I_{10}$		5.11	1.78	[106]
$MA_3Bi_2I_9$		5.52	2.25	[105]
$FTO/TiO_2/MA_3Bi_2I_9$			2.24	[89]
$FTO/TiO_2/MA_3Bi_2I_9$			2.2	[90]

If the reference in Table 24 includes both a measured and calculated value, it is the measure value that is used in Table 24.

Summary of differences

Table of differences between MAPI and MABI:

Table 25 - Differences between MAPI and MABI found in literature.

Characteristic	MAPbI3	MABI3
Dimensionality	3D	2D
Band gap type	direct	indirect
Exciton Binding energy (meV)	30-40	400
Crystal structure (phase)	Tetragonal/Cubic	Hexagonal

Table 26 - Differences between MAPI and MABI from measurements reported in this work.

Characteristic	MAPI	MABI
Response (mV)	+250	variable
Response variance with time	negligible	visible
Decay (recovery)	rapid	slow
Dark WF	4.855	4.944
Band Gap	1.58	1.81
Metallic Cation Atomic size	smaller	larger
Thickness (nm)	400	350

Error sources with the Kelvin probe

The most common sources of error in the Kelvin probe signal were problems with the grounding connection to the sample. This was gradually improved during the investigation as shown in Figure 82. It was found that conductive tape made a particularly poor connection and introduced large resistance. Table 27 lists solutions to some other technical issues encountered.

Worst solution   Best solution
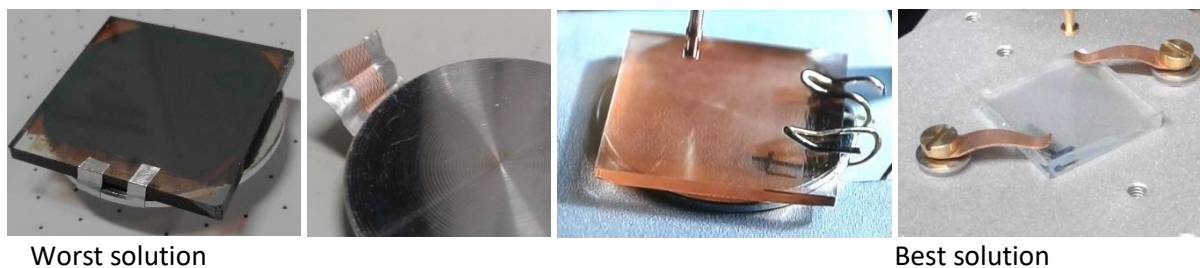
Figure 82 - Evolving methods for grounding the sample to the Kelvin probe system.

Table 27 - Troubleshooting table for common sources of error for operating the Kelvin probe.

Problem	Solution
Poor grounding connection with sample	Do not use conductive tape, use some form of conductive clip
Poor scratching of perovskite layer when trying to reveal conductive FTO for grounding	Use a clean razor blade and scratch with uniform lines
Oxide layer on Aluminium sample mount	This can be penetrated with the locking screw
Contact with the probe affecting tip WF	Lightly dab the underside of the gold tip using a cleanroom cloth and ethanol. Do not apply pressure to the tip just make gentle contact the cloth.
Dust collected on the sample surface	Always blow away dust off the sample surface once mounted with a manual squeezing air duster before every measurement
Moisture/skin oils collected on the sample surface	Do not handle samples or equipment inside the enclosure without gloves. Storing samples in a dry atmosphere can reduce moisture on the surface.
Antistatic strap	This strap may become faulty over time where the connection becomes loose. The signal will be sensitive to static charge from your hand if the strap is broken. If broken, a new strap should be ordered.
Static charge built up on an item in the enclosure	Test if this is the problem by keeping the item outside the enclosure. Then the signal should be normal.

Bibliography

1.   Change NGC. The effects of climate change [Internet]. [cited 2019 Aug 7]. Available from: https://climate.nasa.gov/effects/

2.   Roger Harrabin. Climate change: UK goverment to commit to 2050 target [Internet]. 2019 [cited 2019 Sep 22]. Available from: https://www.bbc.co.uk/news/science-environment-48596775

3.   Change NGC. The causes of climate change. Available from: https://climate.nasa.gov/causes/

4.   Climate Change Committee of the United Kingdom. The UK National Energy and Climate Plan (NECP). Natl Arch [Internet]. 2019;(January):139. Available from: https://assets.publishing.service.gov.uk/government/uploads/system/uploads/attachment_data/file/774235/national_energy_and_climate_plan.pdf

5.   Stephan S, WWF. The Energy Report 100% Renewable Energy By 2050. 2011.

6.   REN21. Renewbles in Cities - 2019 Global Status Report [Internet]. 2019. 336 p. Available from: https://wedocs.unep.org/bitstream/handle/20.500.11822/28496/REN2019.pdf?sequence=1&isAllowed=y%0Ahttp://www.ren21.net/cities/wp-content/uploads/2019/05/REC-GSR-Low-Res.pdf

7.   SPECIFIC. Active Classroom 2018 Cast Study 1 [Internet]. 2018. Available from: https://www.specific.eu.com/wp-content/uploads/2019/12/Active_Classroom_2018_Case_Study-1.pdf

8.   National Geographic. Solar-power. Available from: https://www.nationalgeographic.com/environment/global-warming/solar-power/

9.   IRENA. Renewable Power Generation Costs in 2018 [Internet]. 2019 [cited 2019 Sep 25]. Available from: https://www.irena.org/publications/2019/May/Renewable-power-generation-costs-in-2018

10.   Kibria MT, Ahammed A, Sony SM, Hossain F. A Review : Comparative studies on different generation solar cells technology. Int Conf Environ Asp Bangladesh. 2014;(March):51–3.

11.   Vourvoulias A. How efficienct are solar panels [Internet]. 2020 [cited 2020 Jul 24]. Available from: https://www.greenmatch.co.uk/blog/2014/11/how-efficient-are-solar-panels

12.   Match G. Types of Solar Panels [Internet]. [cited 2020 Jun 17]. Available from: https://www.greenmatch.co.uk/blog/2015/09/types-of-solar-panels

13.   Murthy VS. Third Generation Solar Cells: An Overview [Internet]. [cited 2020 Jun 22]. Available from: http://www.growthconsulting.frost.com/web/images.nsf/0/5C8C038AEE4690D96525744E001A9C9B/$File/TI.htm

14.   Editors of Encylcopaedia Britannica. Photoelectric Effect [Internet]. [cited 2019 Sep 24]. Available from: https://www.britannica.com/science/photoelectric-effect

15.   U.S. Department of Energy. The History of Solar [Internet]. [cited 2019 Sep 24]. Available from: https://www1.eere.energy.gov/solar/pdfs/solar_timeline.pdf

16.   Petrova-Koch V, Hezel R, Goetzberger A, editors. High-Efficient Low-Cost Photovoltaics: Recent Developments. Springer; 2008. 3-5 p.

17.   Solar Flight. Sunseeker 1 - Across America. Available from: https://www.solar-

flight.com/sunseeker-i/

18. Histroy of Solar Power [Internet]. [cited 2019 Sep 26]. Available from: https://www.renewableenergyhub.co.uk/main/solar-panels/the-history-of-solar-power/

19. Akihiro Kojima, Teshima K, Shirai Y, Miyasaka T. Organometal Halide Perovskites as Visible-Light Sensitizers for Photovoltaic Cells. J Am Chem Soc. 2009;131(October):6050–1.

20. Kim HS, Lee CR, Im JH, Lee KB, Moehl T, Marchioro A, et al. Lead iodide perovskite sensitized all-solid-state submicron thin film mesoscopic solar cell with efficiency exceeding 9%. Sci Rep. 2012;2.

21. The world's Biggests solar power plants [Internet]. 2018 [cited 2019 Sep 26]. Available from: https://www.power-technology.com/features/the-worlds-biggest-solar-power-plants/

22. The Guardian. Portugal runs for four days straight on renewable energy alone. Available from: https://www.theguardian.com/environment/2016/may/18/portugal-runs-for-four-days-straight-on-renewable-energy-alone

23. NREL. Best research-cell efficiency chart [Internet]. [cited 2019 Sep 26]. Available from: https://www.nrel.gov/pv/cell-efficiency.html

24. Vox. The global transition to clean energy, explained in 12 charts. Available from: https://www.vox.com/energy-and-environment/2019/6/18/18681591/renewable-energy-china-solar-pv-jobs

25. Fraunhofer ISE. Photovoltaics Report [Internet]. Available from: https://www.ise.fraunhofer.de/content/dam/ise/de/documents/publications/studies/Photovoltaics-Report.pdf

26. Pandey G. India's "last electrified village" Leisang still fighting darkness [Internet]. 2019 [cited 2019 Sep 25]. Available from: https://www.bbc.co.uk/news/world-asia-india-47721497

27. India's $2.5bn scheme to electrify every household [Internet]. 2017 [cited 2019 Sep 25]. Available from: https://www.bbc.co.uk/news/world-asia-india-41397022

28. Navrotsky A. Energetics and Crystal Chemical Systematics among Ilmenite, Lithium Niobate, and Perovskite Structures. Chem Mater [Internet]. 1998;10(10):2787–93. Available from: http://pubs.acs.org/doi/abs/10.1021/cm9801901

29. Zhang Q, Hao F, Li J, Zhou Y, Wei Y, Lin H. Perovskite solar cells: must lead be replaced–and can it be done? Sci Technol Adv Mater [Internet]. 2018;19(1):425–42. Available from: http://doi.org/10.1080/14686996.2018.1460176

30. Hao F, Stoumpos CC, Cao DH, Chang RPH, Kanatzidis MG. Lead-free solid-state organic-inorganic halide perovskite solar cells. Nat Photonics [Internet]. 2014;8(6):489–94. Available from: http://dx.doi.org/10.1038/nphoton.2014.82

31. Frohna K, Stranks SD. Handbook of Organic Materials for Electronic and Photonic Devices [Internet]. Second Edi. Woodhead Publishing Limited; 2019. 211-256 p. Available from: https://www.sciencedirect.com/topics/engineering/diffusion-length

32. Banerjee D, Kumar K. Perovskite Photovoltaics [Internet]. Thomas S, Thankappan A, editors. 2018. 123-162 p. Available from: https://www.sciencedirect.com/topics/engineering/carrier-diffusion-length

33. Frances K. Meet perovskite [Internet]. 2018 [cited 2019 Sep 27]. Available from: https://ideas.ted.com/meet-perovskite-the-mystery-mineral-that-could-transform-our-solar-

energy-future/

34. Swift Solar. Swift Solar - Technology [Internet]. [cited 2019 Sep 27]. Available from: https://www.swiftsolar.com/

35. Potential of perovskite solar for lower cost energy [Internet]. 2019. Available from: https://www.nextbigfuture.com/2019/02/first-commercial-perovskite-solar-late-in-2019-and-the-road-to-moving-the-energy-needle.html

36. Ali R, Hou GJ, Zhu ZG, Yan QB, Zheng QR, Su G. Predicted Lead-Free Perovskites for Solar Cells. Chem Mater. 2018;30(3):718–28.

37. Liang L, Gao P. Lead-Free Hybrid Perovskite Absorbers for Viable Application: Can We Eat the Cake and Have It too? Adv Sci. 2018;5(2).

38. Xiao Z, Song Z, Yan Y. From Lead Halide Perovskites to Lead-Free Metal Halide Perovskites and Perovskite Derivatives. Adv Mater. 2019;1803792:1–22.

39. Chen LJ, Lee CR, Chuang YJ, Wu ZH, Chen C. Synthesis and Optical Properties of Lead-Free Cesium Tin Halide Perovskite Quantum Rods with High-Performance Solar Cell Application. J Phys Chem Lett. 2016;7(24):5028–35.

40. Adonin SA, Frolova LA, Sokolov MN, Shilov G V., Korchagin D V., Fedin VP, et al. Antimony (V) Complex Halides: Lead-Free Perovskite-Like Materials for Hybrid Solar Cells. Adv Energy Mater. 2018;8(6):1–6.

41. Jain SM, Phuyal D, Davies ML, Li M, Philippe B, De Castro C, et al. An effective approach of vapour assisted morphological tailoring for reducing metal defect sites in lead-free, $(CH_3NH_3)_3Bi_2I_9$bismuth-based perovskite solar cells for improved performance and long-term stability. Nano Energy [Internet]. 2018;49:614–24. Available from: https://doi.org/10.1016/j.nanoen.2018.05.003

42. Noel NK, Stranks SD, Abate A, Wehrenfennig C, Guarnera S, Haghighirad AA, et al. Lead-free organic-inorganic tin halide perovskites for photovoltaic applications. Energy Environ Sci. 2014;7(9):3061–8.

43. Bansode U, Naphade R, Game O, Agarkar S, Ogale S. Hybrid perovskite films by a new variant of pulsed excimer laser deposition: A roomerature dry process. J Phys Chem C. 2015;119(17):9177–85.

44. Hebig J-C, Kühn I, Flohre J, Kirchartz T. Optoelectronic Properties of $(CH_3NH_3)_3Sb_2I_9$ Thin Films for Photovoltaic Applications. ACS Energy Lett [Internet]. 2016;1(1):309–14. Available from: http://pubs.acs.org/doi/abs/10.1021/acsenergylett.6b00170

45. Harikesh PC, Mulmudi HK, Ghosh B, Goh TW, Teng YT, Thirumal K, et al. Rb as an Alternative Cation for Templating Inorganic Lead-Free Perovskites for Solution Processed Photovoltaics. Chem Mater. 2016;28(20):7496–504.

46. Boopathi KM, Karuppuswamy P, Singh A, Hanmandlu C, Lin L, Abbas SA, et al. Solution-processable antimony-based light-absorbing materials beyond lead halide perovskites. J Mater Chem A. 2017;5(39):20843–50.

47. Nie R, Mehta A, Park BW, Kwon HW, Im J, Seok S Il. Mixed Sulfur and Iodide-Based Lead-Free Perovskite Solar Cells. J Am Chem Soc. 2018;140(3):872–5.

48. Park BW, Philippe B, Zhang X, Rensmo H, Boschloo G, Johansson EMJ. Bismuth Based Hybrid Perovskites A3Bi2I9 (A: Methylammonium or Cesium) for Solar Cell Application. Adv Mater. 2015;27(43):6806–13.

49.	Kim Y, Yang Z, Jain A, Voznyy O, Kim GH, Liu M, et al. Pure Cubic-Phase Hybrid Iodobismuthates AgBi2I7for Thin-Film Photovoltaics. Angew Chemie - Int Ed. 2016;55(33):9586–90.

50.	Zhu H, Pan M, Johansson MB, Johansson EMJ. High Photon-to-Current Conversion in Solar Cells Based on Light-Absorbing Silver Bismuth Iodide. ChemSusChem. 2017;10(12):2592–6.

51.	Greul E, Petrus ML, Binek A, Docampo P, Bein T. Highly stable, phase pure Cs2AgBiBr6 double perovskite thin films for optoelectronic applications. J Mater Chem A. 2017;5(37):19972–81.

52.	Leonland. Chemical elements by market price [Internet]. [cited 2020 Jun 23]. Available from: http://www.leonland.de/elements_by_price/en/list

53.	Song T Bin, Yokoyama T, Aramaki S, Kanatzidis MG. Performance Enhancement of Lead-Free Tin-Based Perovskite Solar Cells with Reducing Atmosphere-Assisted Dispersible Additive. ACS Energy Lett. 2017;2(4):897–903.

54.	Lee SJ, Shin SS, Kim YC, Kim D, Ahn TK, Noh JH, et al. Fabrication of Efficient Formamidinium Tin Iodide Perovskite Solar Cells through SnF2-Pyrazine Complex. J Am Chem Soc. 2016;138(12):3974–7.

55.	Noel NK, Stranks SD, Abate A, Wehrenfennig C, Guarnera S, Haghighirad AA, et al. Lead-free organic-inorganic tin halide perovskites for photovoltaic applications. Energy Environ Sci [Internet]. 2014;7(9):3061–8. Available from: http://dx.doi.org/10.1039/C4EE01076K

56.	Yokoyama T, Song T Bin, Cao DH, Stoumpos CC, Aramaki S, Kanatzidis MG. The Origin of Lower Hole Carrier Concentration in Methylammonium Tin Halide Films Grown by a Vapor-Assisted Solution Process. ACS Energy Lett. 2017;2(1):22–8.

57.	Jokar E, Chien CH, Tsai CM, Fathi A, Diau EWG. Robust Tin-Based Perovskite Solar Cells with Hybrid Organic Cations to Attain Efficiency Approaching 10%. Adv Mater. 2019;31(2):1–7.

58.	Cells LPS. Lead-Free Perovskite Solar Cells. 2017;904–5.

59.	Baranwal AK, Masutani H, Sugita H, Kanda H, Kanaya S, Shibayama N, et al. Lead-free perovskite solar cells using Sb and Bi-based A3B2X9 and A3BX6 crystals with normal and inverse cell structures. Nano Converg [Internet]. 2017;4(1):26. Available from: http://nanoconvergencejournal.springeropen.com/articles/10.1186/s40580-017-0120-3

60.	Jiang F, Yang D, Jiang Y, Liu T, Zhao X, Ming Y, et al. Chlorine-Incorporation-Induced Formation of the Layered Phase for Antimony-Based Lead-Free Perovskite Solar Cells. J Am Chem Soc. 2018;140(3):1019–27.

61.	Hussain AA, Rana AK, Ranjan M. Air-stable lead-free hybrid perovskite employing self-powered photodetection with an electron/hole-conductor-free device geometry. Nanoscale. 2019;11(3):1217–27.

62.	Ke W, Kanatzidis MG. Prospects for low-toxicity lead-free perovskite solar cells. Nat Commun [Internet]. 2019;10(1):1–4. Available from: http://dx.doi.org/10.1038/s41467-019-08918-3

63.	Greul E, Petrus ML, Binek A, Docampo P, Bein T. Highly stable, phase pure Cs $_2$ AgBiBr $_6$ double perovskite thin films for optoelectronic applications. J Mater Chem A [Internet]. 2017; Available from: http://xlink.rsc.org/?DOI=C7TA06816F

64.	Tao SH, Bolger PM. Hazard assessment of germanium supplements. Regul Toxicol Pharmacol. 1997;25(3):211–9.

65.	Krishnamoorthy T, Ding H, Yan C, Leong WL, Baikie T, Zhang Z, et al. Lead-free germanium iodide perovskite materials for photovoltaic applications. J Mater Chem A. 2015;3(47):23829–

32.

66. Johansson MB, Zhu H, Johansson EMJ. Extended Photo-Conversion Spectrum in Low-Toxic Bismuth Halide Perovskite Solar Cells. J Phys Chem Lett. 2016;7(17):3467–71.

67. Iefanova A, Adhikari N, Dubey A, Khatiwada D, Qiao Q. Lead free CH3NH3SnI3 perovskite thin-film with p-type semiconducting nature and metal-like conductivity. AIP Adv. 2016;6(8).

68. Wu C, Zhang Q, Liu Y, Luo W, Guo X, Huang Z, et al. The Dawn of Lead-Free Perovskite Solar Cell: Highly Stable Double Perovskite Cs 2 AgBiBr 6 Film. Adv Sci. 2018;5(3):2–9.

69. Pantaler M, Cho KT, Queloz VIE, García Benito I, Fettkenhauer C, Anusca I, et al. Hysteresis-Free Lead-Free Double-Perovskite Solar Cells by Interface Engineering. ACS Energy Lett. 2018;3(8):1781–6.

70. Liao W, Zhao D, Yu Y, Shrestha N, Ghimire K, Grice CR, et al. Fabrication of Efficient Low-Bandgap Perovskite Solar Cells by Combining Formamidinium Tin Iodide with Methylammonium Lead Iodide. J Am Chem Soc. 2016;138(38):12360–3.

71. Hu Y, Qiu T, Bai F, Miao X, Zhang S. Enhancing moisture-tolerance and photovoltaic performances of FAPbI3 by bismuth incorporation. J Mater Chem A. 2017;5(48):25258–65.

72. Hu Y, Qiu T, Bai F, Ruan W, Zhang S. Highly Efficient and Stable Solar Cells with 2D MA3Bi2I9/3D MAPbI3 Heterostructured Perovskites. Adv Energy Mater. 2018;8(19):1–9.

73. Ran C, Wu Z, Xi J, Yuan F, Dong H, Lei T, et al. Construction of Compact Methylammonium Bismuth Iodide Film Promoting Lead-Free Inverted Planar Heterojunction Organohalide Solar Cells with Open-Circuit Voltage over 0.8 V. J Phys Chem Lett. 2017;8(2):394–400.

74. Zhang L, Wang K, Zou B. Bismuth Halide Perovskite-Like Materials: Current Opportunities and Challenges. ChemSusChem. 2019;12(8):1612–30.

75. Harwell JR, Baikie TK, Baikie ID, Payne JL, Ni C, Irvine JTS, et al. Probing the energy levels of perovskite solar cells: Via Kelvin probe and UV ambient pressure photoemission spectroscopy. Phys Chem Chem Phys. 2016;18(29):19738–45.

76. Singh T, Kulkarni A, Ikegami M, Miyasaka T. Effect of Electron Transporting Layer on Bismuth-Based Lead-Free Perovskite (CH3NH3)3 Bi2I9 for Photovoltaic Applications. ACS Appl Mater Interfaces. 2016;8(23):14542–7.

77. Im JH, Kim HS, Park NG. Morphology-photovoltaic property correlation in perovskite solar cells: One-step versus two-step deposition of CH3NH3PbI 3. APL Mater [Internet]. 2014;2(8). Available from: http://dx.doi.org/10.1063/1.4891275

78. Yin M, Xie F, Chen H, Yang X, Ye F, Bi E, et al. Annealing-free perovskite films by instant crystallization for efficient solar cells. J Mater Chem A. 2016;4(22):8548–53.

79. Smith B. HOPV16 - Lab-scale perovskite solar cell workshop. :3–7.

80. Ahn N, Son DY, Jang IH, Kang SM, Choi M, Park NG. Highly Reproducible Perovskite Solar Cells with Average Efficiency of 18.3% and Best Efficiency of 19.7% Fabricated via Lewis Base Adduct of Lead(II) Iodide. J Am Chem Soc. 2015;137(27):8696–9.

81. Fang X, Wu Y, Lu Y, Sun Y, Zhang S, Zhang J, et al. Annealing-free perovskite films based on solvent engineering for efficient solar cells. J Mater Chem C. 2017;5(4):842–7.

82. Xiao M, Huang F, Huang W, Dkhissi Y, Zhu Y, Etheridge J, et al. A fast deposition-crystallization procedure for highly efficient lead iodide perovskite thin-film solar cells. Angew Chemie - Int

Ed. 2014;53(37):9898–903.

83. Prochowicz D, Tavakoli MM, Solanki A, Goh TW, Pandey K, Sum TC, et al. Understanding the effect of chlorobenzene and isopropanol anti-solvent treatments on the recombination and interfacial charge accumulation in efficient planar perovskite solar cells. J Mater Chem A. 2018;6(29):14307–14.

84. Jeon NJ, Noh JH, Kim YC, Yang WS, Ryu S, Seok S Il. Solvent engineering for high-performance inorganic-organic hybrid perovskite solar cells. Nat Mater. 2014;13(9):897–903.

85. Fan P, Gu D, Liang GX, Luo JT, Chen JL, Zheng ZH, et al. High-performance perovskite CH3NH3PbI3thin films for solar cells prepared by single-source physical vapour deposition. Sci Rep. 2016;6(July):1–9.

86. Jiang J, Tao H jun, Chen S, Tan B, Zhou N, Zhu L, et al. Efficiency enhancement of perovskite solar cells by fabricating as-prepared film before sequential spin-coating procedure. Appl Surf Sci [Internet]. 2016 May;371(7):289–95. Available from: http://dx.doi.org/10.1016/j.apsusc.2016.02.206

87. Zhang W, Saliba M, Moore DT, Pathak SK, Hörantner MT, Stergiopoulos T, et al. Ultrasmooth organic-inorganic perovskite thin-film formation and crystallization for efficient planar heterojunction solar cells. Nat Commun. 2015;6.

88. Hoye RLZ, Brandt RE, Osherov A, Stevanovic V, Stranks SD, Wilson MWB, et al. Methylammonium Bismuth Iodide as a Lead-Free, Stable Hybrid Organic-Inorganic Solar Absorber. Chem - A Eur J. 2016;22(8):2605–10.

89. Mohammad T, Kumar V, Dutta V. Electric field assisted spray coated lead free bismuth iodide perovskite thin film for solar cell application. Sol Energy [Internet]. 2019;182(December 2018):72–9. Available from: https://doi.org/10.1016/j.solener.2019.02.034

90. Ahmad K, Ansari SN, Natarajan K, Mobin SM. A (CH 3 NH 3) 3 Bi 2 I 9 Perovskite Based on a Two-Step Deposition Method: Lead-Free, Highly Stable, and with Enhanced Photovoltaic Performance. ChemElectroChem. 2018;6(4):1192–8.

91. Öz S, Hebig JC, Jung E, Singh T, Lepcha A, Olthof S, et al. Zero-dimensional (CH3NH3)3Bi2I9 perovskite for optoelectronic applications. Sol Energy Mater Sol Cells. 2016;158:195–201.

92. McDonald C, Ni C, Švrček V, Lozac'H M, Connor PA, Maguire P, et al. Zero-dimensional methylammonium iodo bismuthate solar cells and synergistic interactions with silicon nanocrystals. Nanoscale. 2017;9(47):18759–71.

93. Bredas J-L. Mind the gap! Mater Horiz [Internet]. 2014;1:17–9. Available from: https://pubs.rsc.org/en/content/articlepdf/2014/mh/c3mh00098b

94. Dechun Z. Chemical and photophysical properties of materials for OLEDs [Internet]. Organic Light-Emitting Diodes (OLEDs): Materials, Devices and Applications. Woodhead Publishing Limited; 2013. 114-142 p. Available from: http://dx.doi.org/10.1533/9780857098948.1.114

95. Amalathas AP, Conrad B. Probing photoinduced degradation of CH3NH3PbI3 perovskite films by Kelvin Probe and Photoluminescence techniques. 2018;(November).

96. Brown DR, Brumbach M, Ihlefeld J, Smith S. Improving Kelvin probe work function measurement reliability. 2011;

97. Smith GXR, Crook R, Wadhawan JD. Measuring the work function of TiO2nanotubes using illuminated electrostatic force microscopy. J Phys Conf Ser. 2013;471(1).

98.   Kronik L, Shapira Y. Surface photovoltage phenomena : theory , experiment , and applications.

99.   Sze SM. Physics of Semiconductor Devices. Second Edi. John Wiley &Sons; 1981. 18-19 p.

100.   Schroder DK. Surface voltage and surface photovoltage- history theory and applications. 2001;12.

101.   Harrick plasma. Plasma-cleaning [Internet]. [cited 2020 Jun 29]. Available from: https://harrickplasma.com/plasma-cleaning/

102.   Helander MG, Greiner MT, Wang ZB, Tang WM, Lu ZH. Work function of fluorine doped tin oxide. J Vac Sci Technol A Vacuum, Surfaces, Film. 2011;29(1):011019.

103.   Miller EM, Zhao Y, Mercado CC, Saha SK, Luther JM, Zhu K, et al. Substrate-controlled band positions in CH3NH3PbI3perovskite films. Phys Chem Chem Phys. 2014;16(40):22122–30.

104.   Baikie ID, Grain A, Sutherland J, Law J. Near ambient pressure photoemission spectroscopy of metal and semiconductor surfaces. Phys Status Solidi Curr Top Solid State Phys [Internet]. 2015;12(3):259–62. Available from: http://dx.doi.org/10.1016/j.apsusc.2014.08.159

105.   Lyu M, Yun JH, Cai M, Jiao Y, Bernhardt P V., Zhang M, et al. Organic–inorganic bismuth (III)-based material: A lead-free, air-stable and solution-processable light-absorber beyond organolead perovskites. Nano Res. 2016;9(3):692–702.

106.   Shin J, Kim M, Jung S, Kim CS, Park J, Song A, et al. Enhanced efficiency in lead-free bismuth iodide with post treatment based on a hole-conductor-free perovskite solar cell. Nano Res. 2018;11(12):6283–93.

107.   Aristidou N, Eames C, Sanchez-Molina I, Bu X, Kosco J, Saiful Islam M, et al. Fast oxygen diffusion and iodide defects mediate oxygen-induced degradation of perovskite solar cells. Nat Commun [Internet]. 2017;8(May):1–10. Available from: http://dx.doi.org/10.1038/ncomms15218

108.   Bryant D, Aristidou N, Pont S, Sanchez-Molina I, Chotchunangatchaval T, Wheeler S, et al. Light and oxygen induced degradation limits the operational stability of methylammonium lead triiodide perovskite solar cells. Energy Environ Sci. 2016;9(5):1655–60.

109.   Aristidou N, Eames C, Islam MS, Haque SA. Insights into the increased degradation rate of CH $_3$ NH $_3$ PbI $_3$ solar cells in combined water and O $_2$ environments. J Mater Chem A [Internet]. 2017;5(48):25469–75. Available from: http://xlink.rsc.org/?DOI=C7TA06841G

110.   Baikie T, Fang Y, Kadro JM, Schreyer M, Wei F, Mhaisalkar SG, et al. Synthesis and crystal chemistry of the hybrid perovskite (CH $_3$ NH $_3$)PbI $_3$ for solid-state sensitised solar cell applications. J Mater Chem A. 2013;1(18):5628–41.

111.   Eperon GE, Stranks SD, Menelaou C, Johnston MB, Herz LM, Snaith HJ. Formamidinium lead trihalide: A broadly tunable perovskite for efficient planar heterojunction solar cells. Energy Environ Sci. 2014;7(3):982–8.

112.   Wang H, Tian J, Jiang K, Zhang Y, Fan H, Huang J, et al. Fabrication of methylammonium bismuth iodide through interdiffusion of solution-processed BiI 3 /CH 3 NH 3 I stacking layers. RSC Adv [Internet]. 2017;7(69):43826–30. Available from: http://dx.doi.org/10.1039/C7RA07123J

113.   Podraza NJ, Qiu W, Hinojosa BB, Xu H, Motyka MA, Phillpot SR, et al. Band gap and structure of single crystal BiI3: Resolving discrepancies in literature. J Appl Phys. 2013;114(3).

114.   Lehner AJ, Fabini DH, Evans HA, Hébert CA, Smock SR, Hu J, et al. Crystal and Electronic Structures of Complex Bismuth Iodides A3Bi2I9 (A = K, Rb, Cs) Related to Perovskite: Aiding the Rational Design of Photovoltaics. Chem Mater. 2015;27(20):7137–48.

115. Alsari M, Pearson AJ, Wang JTW, Wang Z, Montisci A, Greenham NC, et al. Degradation Kinetics of Inverted Perovskite Solar Cells. Sci Rep [Internet]. 2018;8(1):6–11. Available from: http://dx.doi.org/10.1038/s41598-018-24436-6

116. Ganose AM, Savory CN, Scanlon DO. Beyond methylammonium lead iodide: prospects for the emergent field of ns2 containing solar absorbers. Chem Commun. 2017;53(1):20–44.

117. He J, Ng C-F, Young Wong K, Liu W, Chen T. Photostability and Moisture Stability of CH3NH3PbI3-based Solar Cells by Ethyl Cellulose. 2016; Available from: https://onlinelibrary.wiley.com/doi/full/10.1002/cplu.201600415#accessDenialLayout

118. Zhang YY, Chen S, Xu P, Xiang H, Gong XG, Walsh A, et al. Intrinsic Instability of the Hybrid Halide Perovskite Semiconductor CH3NH3PbI3∗. Chinese Phys Lett. 2018;35(3).

119. Sachtler WMH, Dorgelo GJH, Holscher AA. The Work Function of Gold. Surf Sci. 1966;5:221–9.

120. Lee BN, Kirmayer S, Edri E, Hodes G, Cahen D. Surface photovoltage spectroscopy study of organo-lead perovskite solar cells. J Phys Chem Lett. 2014;5(14):2408–13.

121. Andersson A, Johansson N, Bröms P, Yu N, Lupo D, Salaneck WR. Fluorine Tin Oxide as an Alternative to Indium Tin Oxide in Polymer LEDs. Adv Mater. 2005;10(11):859–63.

122. Ossila. FTO Coated Glass (Unpatterned) [Internet]. [cited 2019 Jun 6]. Available from: https://www.ossila.com/products/fto-glass-unpatterned

123. Saule Technologies [Internet]. [cited 2019 Oct 9]. Available from: https://sauletech.com/

124. Baikie I. Theory Behind The Kelvin Probe [Internet]. [cited 2019 Oct 3]. Available from: http://www.kelvinprobe.info/technique-theory.htm